

Influence of capillary bridges on weathered tailings material

STEF CARELSEN

November 2013

SUPERVISORS:

Dr. Ir. H.R.G.K. Hack, CEng

Prof. Dr. R.M. van der Meer



Influence of capillary bridges on weathered tailings material

STEF CARELSEN

Enschede, The Netherlands, November 2013

Thesis submitted to the Faculty of Geo-Information Science and Earth Observation of the University of Twente in partial fulfilment of the requirements for the degree of Master of Science in Geo-information Science and Earth Observation.

Specialization: Applied Earth Sciences

SUPERVISORS:

Dr. H.R.G.K. Hack, CEng

Prof. Dr. R.M. van der Meer (Physics of Fluids, University of Twente)

THESIS ASSESSMENT BOARD:

Prof. Dr. V.G. Jetten (chair)

Dr. Ir. S. Slob (External Examiner, Witteveen+Bos)

Ing. W. Verwaal (External Examiner, Delft University of Technology)

DISCLAIMER

This document describes work undertaken as part of a programme of study at the Faculty of Geo-Information Science and Earth Observation of the University of Twente. All views and opinions expressed therein remain the sole responsibility of the author, and do not necessarily represent those of the Faculty.

Не ваља паран број

- Кафана хајдук вељко, Бор, Србија (2011)

Abstract

Weathering of tailings materials (mine waste) can affect the grain size and angularity of the grains. As a consequence, the angle of repose of such granular material and void volume (porosity) decreases, which potentially results in the failure of a slope of such material (e.g., tailings dam). The decrease of the porosity may affect the permeability and increases the (volumetric) water content (W) of the material. The water content of a material influences the amount of capillary bridges that are formed in a unsaturated granular material. Most research has been done on the effects of these capillary bridges on the static shear strength. In this thesis, the influence of the residual (dynamic) shear stress was studied with a newly built shear box test. The resulting Mohr Coulomb failure envelope suggests that for water content below the maximum value of the residual shear strength ($W = 0.1$), capillary bridges add to rigidity of the bulk material rather than adhesion in the shear band. This is reflected in an increasing angle of internal friction, while the cohesion is negligibly low. A peak in the cohesion at $W = 0.1$ suggests that capillary bridges are formed and pinched off continuously in the shear band, resulting in a maximum residual shear strength. Finally, for $W > 0.1$ both the angle of internal friction and cohesion are found to decrease significantly.

Preface

This Thesis is the final result of a master project done at the Earth Systems Analysis (ESA) department of ITC, Faculty of Geo-Information Science and Earth Observation of the University of Twente. The experiments presented in this Thesis were carried out under the aegis of the Physics of Fluid (PoF) research chair belonging to the faculty of Science and Technology at the University of Twente. The faculty ITC is situated in the center of the city of Enschede (Overijssel, East-Netherlands) and was recently incorporated into the University of Twente. The campus of the University of Twente is located on the outskirts of Enschede and counts about 3300 scientist and 9000 students.

The ESA department investigates geo-information to improve the understanding of earth's surface and subsurface processes in both space and time. The three mainstreams are the sustainable use of earth resources (Earth Resources Exploration), the influence of geological and geotechnical processes on the construction or performance of civil structures (Engineering Geology), and the mitigation of natural and man-induced disasters (Natural Hazards and Disaster Risk Management).

The focus of the research done at the PoF chair is the fundamental understanding the phenomena in the physics of fluids, bubbles and jets by the use of (a combination of) experimental, theoretical and numerical techniques. The research ranges from the fundamental understanding of turbulence, e.g. Taylor-Couette flow and Rayleigh-Bénard convection, and granular flows, such as the impact of a sphere on fluidised sand, to the medical application of cavitating bubbles during a root canal treatment.

This work is in line with a previous internship on remediation of mine tailings conducted in Bor (East-Serbia) from February to August 2011 with Dutch engineering company Witteveen+Bos.

Stef Carelsen started in 2004 with his study Applied physics at the University of Twente and received his Bachelor of Science degree in April 2010. The Bachelor project was done in the research chair of Inorganic Material Science in the spring of 2008 and was titled: “*Heat transfer between plasma and substrate surface during Pulsed Laser Deposition*”. He started to study Applied Earth Sciences in January 2010 alongside his M.Sc. in Applied Physics, which he achieved on 22nd February 2013 with Thesis-title: *Pushing oobleck to the limit: Force response of an intruder in a dense cornstarch suspension.*¹

Acknowledgements

I am glad to thank Robert Hack for the geotechnical endeavour of the last four years. What started as a casual meeting on the first of December 2009 to do a short course in Earth Sciences, now ends in a full Master of Science degree. Robert, this wouldn't have happened in the first place if it wasn't for you. You have given me new knowledge and guided me past bureaucratic impediments and in all weather to enjoy a coffee. I cannot thank you enough for this.

I take great pleasure in thanking Devaraj van der Meer and Detlef Lohse of the Physics of Fluids (PoF) chair. Devaraj van der Meer was my daily supervisor and played an important role in the experiments and analysis thereof. Devaraj, thanks you for all your help with this research and Thesis. I wish you good luck with your professorship and your chair "Physics of Granular Matter and Interstitial Fluids" all the best results, publications, prizes, and PhD-grants.

All the research at PoF would not be possible if it weren't for the secretary and technicians: Joanita Leferink, Gert-Wim Bruggert, Bas Benschop, and Martin Bos. Thank you all for helping me with designing and building the experimental setup of which this Thesis is the result. Also, I want to acknowledge Wim Verwaal of the Technical University of Delft for his useful insights during the sketching phase of this setup.

I acknowledge the inhabitants of Student Room A and its sublime Patron: E.E.N. Maurice, E.N. Luuk, N. Maarten, Bart, Marise, Bram S., Wolter, Matthijs, Erik, Rodrigo, Thomas, and Martin: Thanks for the great times, preposterous imitations, and good discussions.

This second study would not have been possible if it weren't for Marloes Letteboer and Jeroen Verschuur who handled most administrative hurdles for which I am grateful.

Now that I hopefully thanked everybody from the TNW-faculty, I want to thank Victor Jetten and the other staff members of the Earth Systems Analysis department from ITC. I am in particular grateful to Harald van der Werff for showing great perseverance with probably the most complicated student ITC has stumbled upon. Boudewijn de Smeth, I thank you for your help on the chemical weathering part. As a physicist *pur sang*, chemistry is something I try to avoid, so your corrections were much appreciated.

For old times sake, I would like to thank for the good times I had with the AES-2011-students: Pooyan, Viet, Rana, Keshav, Ronni, Haydar, etc.

This research wasn't restricted to Enschede. I thank Witteveen+Bos' Siefko Slob for exchanging views on the properties of tailings and Marten van der Wijk for giving me the opportunity to investigate tailings material in Bor, Serbia and providing me the results from their geotechnical investigations. Besides Marten and Siefko I also had fruitful discussions and a good time with Dirk de Kramer, Peter den Bossche, Ingrid Rijk, Harry Pachen, Thomas von Schwartzberg, and Jelena Zugić.

During my times in Bor, I met many friendly and helpful Serbs of whom I want to thank:

Regionalni Rezvoj Bora: Aleksandar Budjelan and Duško Spasojević.

Technički Fakultet u Boru: Saša Stojadinović and Radoje Pantović.

Institut za Rudarstvo i Metalurgiju Bor: Zoran Stevanović and Vladan Marinković.

Rudarsko-Topioničarski Basen Bor: Slaviša Nikolić.

Harizma: Zoran Vesković and Olivier Mitrović.

I am grateful to the home supporters: To my parents Frans and Anneke, brothers Bart and Floris, in-laws Suzan and Sarai, and nephews Carsten, Lars and Olivier: Thank you for all the support and faith in every way during these f/n-ine years! And in particular my girlfriend, Mireille, thank you for all your support and necessary distractions from my work. I know that I can be a bit of a workaholic, and you always made sure that I took my rest at the right moments!

I take this opportunity thank the (formers) residents of Huize MacGyver, where I lived for the past 8¹/₂ years. I also found great joy in my student days with the convivial Heeren van Bracque. I thank them for all the fine weekends, excellent beer brewing activities, and Wednesday nights spent in the pub.

Lastly, I thank Aleksander Budjelan for kindly providing the Serbian sayings I often stumbled across during my internship in Bor. As written after the title page of this Thesis: “Ne valja paran broj” literally means “Do not be an even number”. This saying is often used in Serbian taverns (kafana’s) to push someone in drinking a third schnapps. The second slivovitz was already imposed with a “Došao si na dve noge” (“You came on two legs”)¹. As a consequence, you likely end up in an advancing state of inebriation causing next drinks to be a stone’s throw. In this case, it refers to the second Master of Science that is now concluded with this thesis. Although this part is done, citizens-life and more work lie ahead.

Stef Carelsen
Enschede, The Netherlands
Friday 29th November, 2013

Table of Contents

| | |
|---|-------------|
| Abstract | i |
| Preface | iii |
| Acknowledgements | v |
| Table of Contents | vii |
| List of Figures | ix |
| List of Tables | xi |
| Glossary | xiii |
| 1 Introduction | 1 |
| 1.1 Overburden waste | 2 |
| 1.2 Tailings | 3 |
| 1.3 Tailings dam failures | 4 |
| 1.4 Scientific framework | 5 |
| 1.5 Scope | 6 |
| 2 Decay: Weathering and erosion | 7 |
| 2.1 Weathering | 8 |
| 2.1.1 Physical weathering | 8 |
| 2.1.2 Chemical weathering | 11 |
| 2.1.3 Biotic weathering | 13 |
| 2.2 Erosion | 14 |
| 2.3 Factors controlling decay | 15 |
| 2.3.1 Weathering intensity | 15 |
| 2.3.2 Weathering intensity rate | 17 |
| 2.3.3 Summary | 20 |
| 3 Decay of tailings dams | 21 |
| 3.1 Tailings dams | 22 |
| 3.1.1 Construction | 22 |
| 3.1.2 Material characteristics | 24 |
| 3.1.3 Weathering | 25 |
| 3.1.4 Erosion | 26 |
| 3.2 Slope stability | 27 |
| 3.3 RTB copper mine, Bor, Serbia | 28 |
| 3.3.1 Project components | 28 |
| 3.3.2 Tailings Disposal Facilities (TDFs) | 29 |
| 3.3.3 Tailings dams | 29 |
| 4 Liquid content and the shear strength of wet granular matter | 37 |
| 4.1 Wet granular matter | 37 |
| 4.1.1 Solid phase | 38 |

| | | |
|----------|--|-----------|
| 4.1.2 | Liquid phase | 38 |
| 4.2 | Capillary bridges | 39 |
| 4.2.1 | Energies | 40 |
| 4.2.2 | Regimes of wetness | 41 |
| 4.3 | Shear strength | 43 |
| 4.3.1 | Shear strength of an unsaturated soil | 43 |
| 4.3.2 | Static friction | 43 |
| 4.3.3 | Dynamic friction | 43 |
| 5 | Experiment | 45 |
| 5.1 | Shear box | 45 |
| 5.1.1 | Supporting plate | 47 |
| 5.1.2 | Gap width | 47 |
| 5.2 | Actuation | 48 |
| 5.2.1 | Precision | 48 |
| 5.2.2 | Rail friction | 48 |
| 5.3 | Measurement | 49 |
| 5.3.1 | Noise reduction | 49 |
| 5.3.2 | Calibration | 50 |
| 5.3.3 | Data acquisition | 51 |
| 5.4 | Sample | 51 |
| 5.4.1 | Packing fraction | 53 |
| 5.4.2 | Liquid content | 53 |
| 6 | Analysis & Results | 55 |
| 6.1 | Analysis | 55 |
| 6.1.1 | Noise filtering | 55 |
| 6.1.2 | Timing | 56 |
| 6.1.3 | Baseline | 56 |
| 6.1.4 | Average determination | 57 |
| 6.1.5 | Calculation of shear stresses | 58 |
| 6.2 | Results | 60 |
| 6.2.1 | σ_p - and σ_{p+g} -experiments | 60 |
| 6.2.2 | Grain-to-grain shear stress (σ_g) | 62 |
| 6.2.3 | Mohr-Coulomb | 63 |
| 7 | Conclusion & Recommendations | 67 |
| 7.1 | Discussion & Conclusion | 67 |
| 7.2 | Recommendations | 69 |
| 7.2.1 | Improvements | 69 |
| 7.2.2 | Future work | 69 |
| | List of References | 71 |
| | A Southeast “Ostrelj” overburden waste dump | 81 |
| | B Experimental setup phases | 85 |
| | C Matlab script | 89 |

List of Figures

| | | |
|------|---|----|
| 1.1 | Total world refined copper consumption from 1970 to 2004. | 1 |
| 1.2 | Origin of mine wastes: (B) Overburden waste and (C) tailings. | 2 |
| 1.3 | World mine production of copper and copper-tailings accumulation since 1900. | 3 |
| 1.4 | Failures of conventional and tailings dams from 1909 to 1999. | 4 |
| 1.5 | Causes of registered tailings dams failures from 1917 to 1989. | 5 |
| | | |
| 2.1 | Frost and thermal weathering in the field. | 10 |
| 2.2 | Honeycomb weathering of limestone. | 10 |
| 2.3 | Exfoliation jointing. | 11 |
| 2.4 | Types of water erosion. | 14 |
| 2.5 | Gully erosion due to water running off the slope of an overburden waste rock dump. | 15 |
| 2.6 | Diagrammatic illustrative views of stages of granite weathering. | 17 |
| 2.7 | Basic map of the World distinguishing four climates. | 18 |
| 2.8 | Difference in weathering grades on both sides of a sandstone tombstone. | 19 |
| 2.9 | Factors that control decay. | 20 |
| | | |
| 3.1 | Failure of the Los Freiles tailings dam. | 21 |
| 3.2 | Construction scheme of a water retaining tailings dam. | 22 |
| 3.3 | Construction schemes of phased tailings dams. | 23 |
| 3.4 | Drawing of the principle behind a cyclone, which used to separate the courser and fine fraction of tailings. | 24 |
| 3.5 | Formation of a hardpan layer of cemented tailings. | 26 |
| 3.6 | Typical angles of repose of several granular materials. | 27 |
| 3.7 | Map of Serbia. | 29 |
| 3.8 | Satellite view of Bor indicating the mine waste structures. | 30 |
| 3.9 | Particle size distribution of tailings material in Krivelj TDF 2, Bor, Serbia. | 31 |
| 3.10 | Seepage of Acid Mine Drainage at the base of tailings dam 1 (TDF1, Bor, Serbia). | 32 |
| 3.11 | Decay on top of tailings dam 3 (TDF2, Bor, Serbia) | 33 |
| 3.12 | Topography of the project area (Bor, Serbia). | 34 |
| 3.13 | 3D GIS representation of Krivelj TDF 2. | 35 |
| 3.14 | Krivelj Tailings Disposal Facility (TDF). | 36 |
| | | |
| 4.1 | Volumes of the phases in a granular matter. | 37 |
| 4.2 | Effects of liquid content on the cohesion of granular material. | 39 |
| 4.3 | Geometrical constants of a capillary bridge. | 39 |
| 4.4 | Energies in granular materials as a function of the particles radii. | 40 |
| 4.5 | Wetting regimes encountered while increasing the liquid content of granular matter. | 41 |
| 4.6 | The number of capillary bridges, number of cluster, and the normalised volume of the largest cluster as a function of the water content W in a wet granular pile. | 42 |
| 4.7 | Yield strength versus water content of a sample of grains. | 44 |

| | | |
|-----|---|----|
| 5.1 | Digital drawing and photograph of the setup. | 46 |
| 5.2 | Close-up of the upper-container while it is loaded | 46 |
| 5.3 | Measurement of the shear force of the (empty) setup for several velocities. . . | 48 |
| 5.4 | Load cell used in the experiments. | 49 |
| 5.5 | Electronic circuit of the load cell. | 50 |
| 5.6 | Calibration of the load cell. | 51 |
| 5.7 | Scanning Electron Microscope (SEM) imagery of the 1 mm glass beads used in the experiments. | 52 |
| 6.1 | Example of a measured and its filtered signal. | 56 |
| 6.2 | Detailed view of the first four shear measurements. | 57 |
| 6.3 | Detailed view of the first pulling motion, displaying the four average intervals. 58 | |
| 6.4 | Schematic topview of the upper container | 59 |
| 6.5 | Shear stress σ_s versus normal pressure σ_n for $W = 0$, $W = 0.1$, and $W = 0.2$. 61 | |
| 6.6 | σ_g calculated for $W = 0$, $W = 0.1$, and $W = 0.2$ | 62 |
| 6.7 | Mohr-Coulomb criteria ϕ and c as a function of the water content W | 64 |
| 7.1 | Schematic representation of energy from capillary forces in the system versus the water content. | 68 |
| A.1 | Weathering profile at the NE of Ostrelj overburden waste dump (1). | 83 |
| A.2 | Weathering profile at the NE of Ostrelj overburden waste dump (2). | 84 |
| A.3 | Weathering profile at the SE of Ostrelj overburden waste dump. | 84 |
| B.1 | Preliminary sketch of the setup. | 85 |
| B.2 | Conceptual first digital drawing of the setup. | 86 |
| B.3 | Digitally drawn cross section and photograph of the spring-tipped rod. | 88 |

List of Tables

| | | |
|-----|--|----|
| 2.1 | Typical pressure values arising from several processes that cause weathering. | 9 |
| 2.2 | Weathering description and classification by BS5930 1999. | 16 |
| 2.3 | Relative stability of several minerals. | 17 |
| 3.1 | Examples of Acid Mine Drainage (AMD) producing weathering reactions in sulfidic mine wastes. | 25 |
| 4.1 | Maximum packing fraction, ϕ , for several crystalline and amorphous configuration of spheres. | 38 |
| 4.2 | Types of energy in (wet) granular matter and their relation to the particles radius, r | 40 |
| 5.1 | Liquid content of the samples used. | 53 |
| 6.1 | The coefficient of friction (μ), angle of internal friction (ϕ) and cohesion (c) of the experimental and calculated data. | 65 |
| A.1 | Physical and mechanical properties of rocks at Bor's mining field. | 82 |
| B.1 | Geometrical parameters of the setup. | 86 |

Glossary

- Angle of internal friction (ϕ)** Parameter from the Mohr-Coulomb theory, which is equal to the arctangent of the coefficient of friction μ . Not be mistaken with the packing fraction.
- Angle of repose** Steepest angle possible of a slope of a heap of granular material without the material cascading down (figure 3.6).
- Capillary bridge** of a liquid that creates an attractive force in between particles due to the surface tension of the liquid.
- Coefficient of friction (μ)** (see shear strength)
- **Dynamic** ... The ratio between dynamic shear strength and normal pressure σ_n .
 - **Static** ... The ratio between static shear strength and normal pressure σ_n .
- Cohesion (c)** Parameter from the Mohr-Coulomb theory.
- Coordination number** Number of capillary bridges per grain/sphere.
- Decay** The combined action of weathering, erosion, and redistribution of stress (chapter 2).
- Degree of saturation (S)** The fraction of the voids volume that is occupied by water (section 4.1.2).
- Discontinuity** Mechanical or chemical interface in a rock or ground mass, e.g, bedding plane, joints, cracks, fractures, etc.².
- Erosion** Removal and transport of (weathered) material, e.g., by water, gravity, or wind (section 2.2).
- Ground mass** Assembly of intact ground zones with boundaries formed by discontinuities².
- Intact ground** Material comprising of any solid material in the ground consisting of rock, soil or artificial material, without planar features with reduced strength characteristics².
- Intact rock** Aggregate of minerals or of minerals that are bounded together (cemented or interlocked), i.e., with tensile strength, and without discontinuities.
- Intact soil** Mineral or rock particles without cementation or tight interlocking, and without planar features with reduced strength characteristics, i.e. without discontinuities².
- Laplace pressure (P_L)** Pressure difference between the inside and outside of a capillary bridge.
- Liquid content (W)** The ratio of the volume of liquids to the volume of the whole sample, i.e., the packing fraction of the liquid phase.
- Mine waste** All waste that remains after the extraction of the rock material, comprising of overburden and tailings material.

Mohr-Coulomb failure criterion Theoretical linear model describing the shear strength σ_s of a material as function of the normal pressure σ_n : $\sigma_s = \sigma_n' \tan(\phi) + c$, where ϕ is the angle of internal friction and c the cohesion.

Normal pressure (σ_n) Force per unit area applied perpendicular to a surface.

Overburden waste Material that used to be situated on top or around an orebody and was excavated during the construction of an open-pit mine.

Overburden waste dump Site at which overburden waste is dumped.

Packing fraction (ϕ) The fraction of the total volume that is occupied by the solid phase (section 4.1.1). Not be mistaken with angle of internal friction.

Permeability Hydraulic conductivity of a porous medium (e.g., ground), i.e., opposite to the resistance of a medium towards a fluid flow³.

Porosity The fraction of the total volume that is occupied by either air or water (section 4.1.2).

Random dense packing fraction ϕ_{rdp} Typical packing fraction of granular materials after being poured and shaken *in-situ* in a container. Experimentally determined to be 0.62 by Herminghaus⁴.

Rock Aggregate of minerals or of minerals that are bounded together (cemented or interlocked), i.e., with tensile strength

Rock mass Assembly of blocks of intact rock with boundaries formed by discontinuities.

Shear strength

- **Dynamic/Residual** ... The shear stress σ_s required to continuously shear a granular material under a certain normal pressure σ_n .
- **Static** ... The maximum shear stress σ_s which a granular material can sustain under a certain normal pressure σ_n .

Shear stress (σ_s) Tangential force per unit area acting on a contact, i.e., a stress that attempts the internal structure of a material to slide against itself.

Soil Mineral or rock particles without cementation or tight interlocking².

Soil mass Assembly of intact soil zones with boundaries formed by discontinuities².

Surface tension (γ) Line-force that arises from molecular attraction, causing the surface of a liquid to contract.

Tailings Residual waste after ore processing (chapter 1).

Tailings dam Dam made from tailings material.

Tailings Disposal Facility (TDF) Impoundment in which tailings material is stored, including the retaining (tailings) dams.

Water bridge Capillary bridge from water.

Water content The fraction of the total volume that is occupied by water (section 4.1.2).

Weathering Alteration of a material due to physical, chemical, or biological influences (section 2.1).

Introduction

The past 50 years are characterised by a global trend of economic development and industrialisation. This caused an increase in the demand of commodities in developed as well as developing countries. Particularly, the demand increased for metals that serve as a base for construction, power generation, machines, etc. For example, figure 1.1 displays the ever increasing amount of copper that is consumed per country since 1970. It is noteworthy that emerging economies like China and, to a lesser extent, South Korea and India, are the driving countries behind the increased copper consumption. Further trends indicate that metal consumption in general will rise even further, as the world population, per capita metal consumption, and per capita GDP are expected to increase in the coming years⁵.

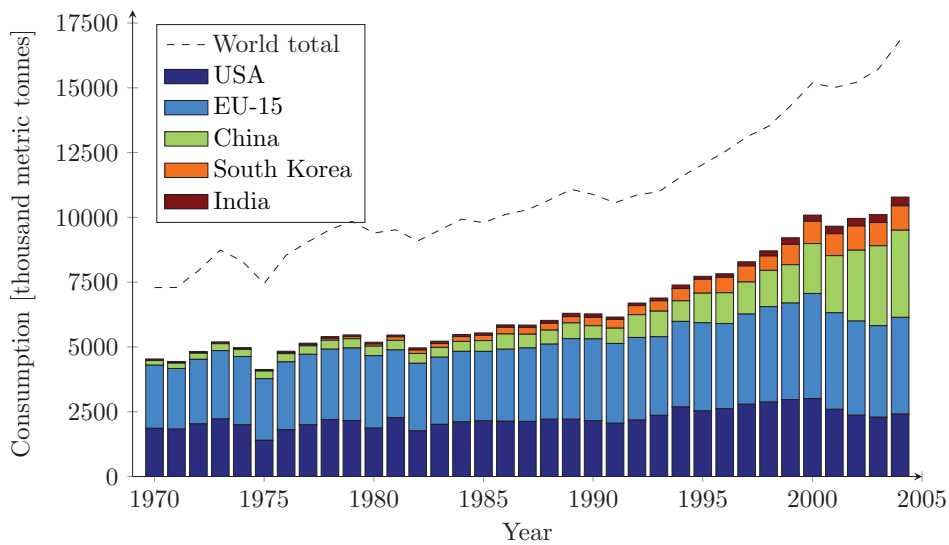


FIGURE 1.1: Total world refined copper consumption from 1970 to 2004 and that of the World's largest (USA and 15 countries of the European Union) and three emerging, Asian economies (China, South Korea, and India). [World consumption after International Copper Study Group (2012)⁶; Consumption per country after USGS (2008)⁷]

Due to this increased consumption of copper, the mine production increases as is shown in figure 1.3. The global mine production of copper has raised steadily over the last years to a grand total of 16.1 million (metric) tonnes of copper ore mined in 2011⁸.

Given copper as an example, mining of any ore mineral in general generates high amounts of waste^{9;10}. In this thesis two types of mine waste are distinguished: *Overburden waste* and *tailings* (figure 1.2), which are both described briefly below.

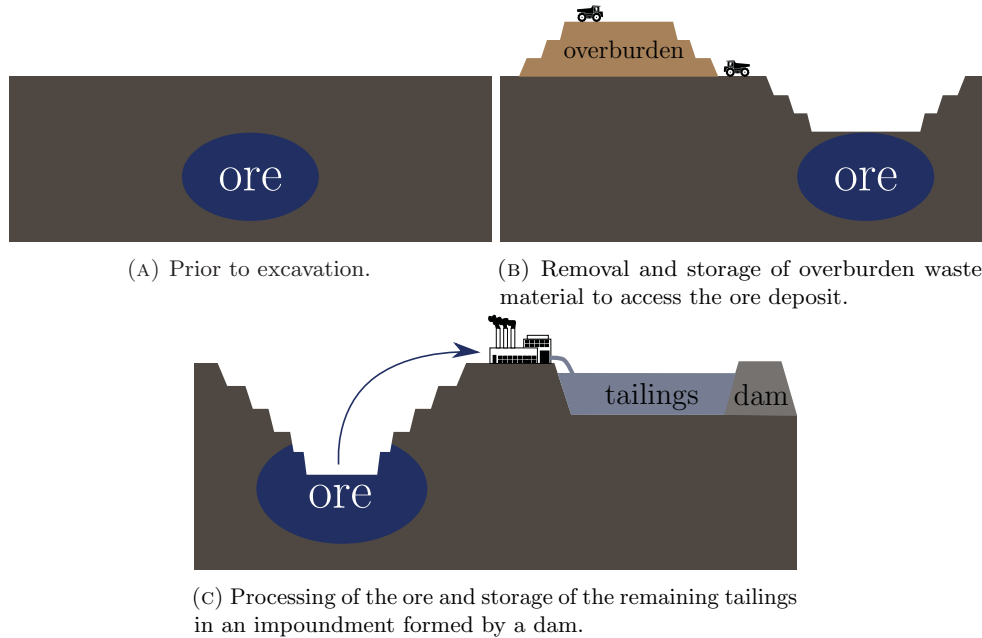


FIGURE 1.2: Origin of mine wastes: (B) Overburden waste and (C) tailings.

1.1 Overburden waste

Overburden waste consists of the material that used to be on top or around the ore deposit. The excavated overburden material is mostly dumped in heaps close to the mine by truck [figure 1.2(b)]. The amount of overburden waste is significant for open-pit mining, causing the heaps to be large and clearly visible. Overburden waste dumps are often characterised by high steep slopes consisting of abundant materials prone to weathering and erosion. Oxidation of overburden material may cause production of Acid Mine Drainage (AMD)⁹⁻¹¹, which is an environmental threat and catalyst for further weathering¹²⁻¹⁴.

Eventually, the weathering process will alter the geotechnical parameters of the material, which can lead to failures if it has not been taken into account in the design of the dump. The design and control are often below standard as there is little economic value and money spend on waste dumps is a direct reduction of the profits of a mine. Possible problems with dumps normally occur after years, often past the financial interest span of the stake holder at the time of mining. Failures can have disastrous consequences. For example, in 1966 a school and 20 houses in Aberfan (Wales, UK) were engulfed by a coal mine's waste slide, killing 144 people, of which 116 school children^{15;16}. An example of a weathering overburden waste dump in Bor (Serbia) is presented in appendix A.

1.2 Tailings

Tailings comprises of the residual ore-material, after it has been crushed and processed to extract the economic minerals. Although most of the ore minerals are taken out, the fine-grained tailings may still contain considerable quantities of ore minerals and may contain chemicals used for the extraction process. The tailings are further likely to contain other minerals that are geologically associated with the ore minerals and thus present in the ore body, but without a sufficient economic value to extract⁹ (chapter 3).

Low-grade ores result in large amounts of tailings. Copper is often mined from rocks with copper-grades less than 1%, i.e., mining cut-off grades are less than 1%, meaning that for some or all of the extracted rock 99% or more is non-metal rock that is dumped as tailings after extracting the copper. Assuming an average grade of 1%, a total of about 57 billion m³ have accumulated since 1900 for copper alone (figure 1.3).

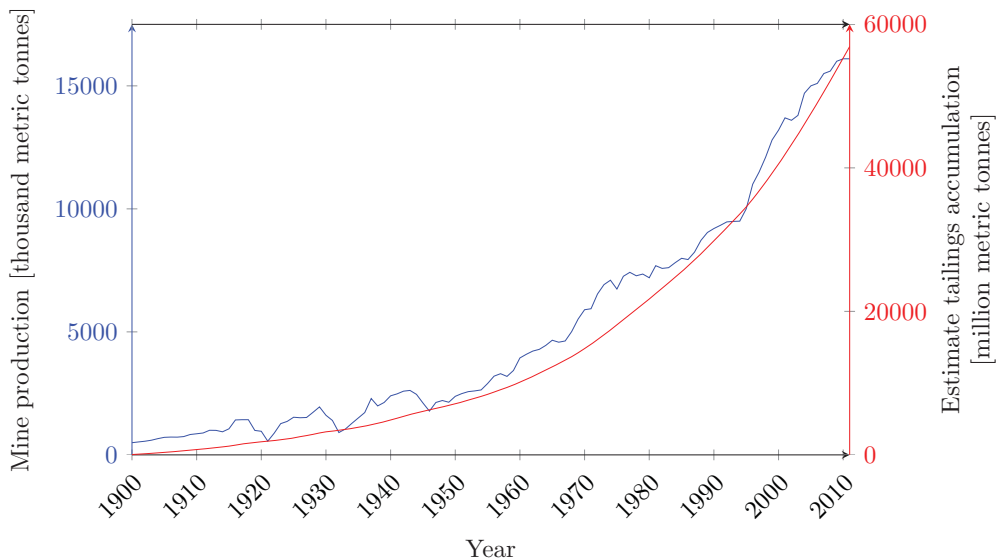


FIGURE 1.3: World mine production of copper (blue) and copper-tailings accumulation (red) since 1900. The tailings accumulation is estimated under the assumption that the cut-off grade of copper ore is 1%. [Data after USGS (2012)⁸]

In a worldwide perspective there are very large quantities of tailings. For copper, it is expected that the total land-based resources exceed 3 billion (metric) tonnes¹⁷. This means that its processing will result in an approximate 300 billion tonnes of tailings only from copper extraction.

These tailings are mixed with large quantities of water and deposited in semi-fluid form in large impoundments which is referred to as *Tailings Disposal Facilities* (TDFs). Martin *et al.* (2002)¹⁸ and Martin & Davies (2002)¹⁹ have tenuously estimated the total amount of active TDFs to be 3500 worldwide. The most common TDFs are valley impoundments, which are made by building dams in a river valley forming a basin in which tailings are pumped. The dams are often constructed from the coarser fraction of the (sand-sized) tailings, as this is the cheapest resource of construction material that is locally available^{9;20} (chapter 3).

1.3 Tailings dam failures

Tailings dam failures have disastrous effects on both the environment as well as human society. For example, the tailings dam failure in Kolontár, Hungary (October 2010) caused a flood that polluted 8 km² of land, killed 10 people, and injured approximately 120 people²¹. Another example is the Aznalcóllar mine spil (April 1998), where an approximate 1.3 million m³ pyritic tailings and 5.5 million m³ tailings water endangered a national park²² (chapter 3). Nowadays, the environmental impact is still apparent in the acidity of the soil and groundwater²³.

Martin & Davies (2002)¹⁹ indicate that the number of tailings dam failures as compared to that of conventional water retaining dams are increasing (see figure 1.4). Szymanski (1999)²⁴ reported that reasons for this increase may be found in the difference in construction, but also the lack of interest and accompanied in-house expertise on dam engineering of mining companies. After all, the maintenance of a TDF is merely a burden to a mining company, which evaporates part of the profit. A correlation between tailings dam failures and mining market cycles was found by Davies & Martin (2009)²⁵.

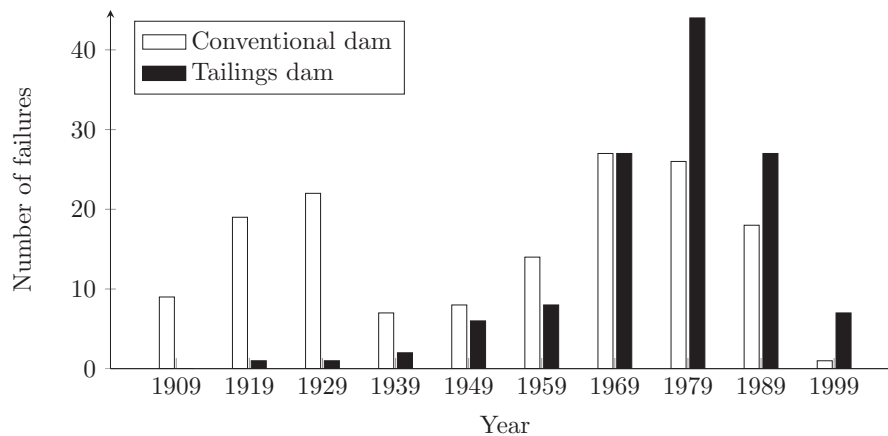


FIGURE 1.4: Failures of conventional and tailings dams from 1909 to 1999. [Data after Martin *et al.* (2002)¹⁸ and Martin & Davies (2002)¹⁹]

Another reason for this increase in failures may be due to the ageing of the tailings dams. Large-scale mining started 100–200 years ago, and nowadays, these dams are probably weathered and start failing.

Figure 1.5 gives the main cause of failures of tailings dams worldwide, as documented by Rico *et al.* (2008)²⁶. The majority of incidents has meteorological causes (25%). Also deficient management is often the issue as that accounts for 10% of the total number of failures. Although for a large part meteorological causes are described in the literature as cause, this may be doubted to be always the true cause.

It is difficult to understand that meteorological conditions cause instability of a slope after many years of existence. For such slopes it is highly likely that similar circumstances have happened before without causing instability. Therefore meteorological conditions are likely more the trigger while the underlying mechanism, i.e., the cause, is something else, such as degradation of material properties due to weathering or changes in slope geometry²⁷.

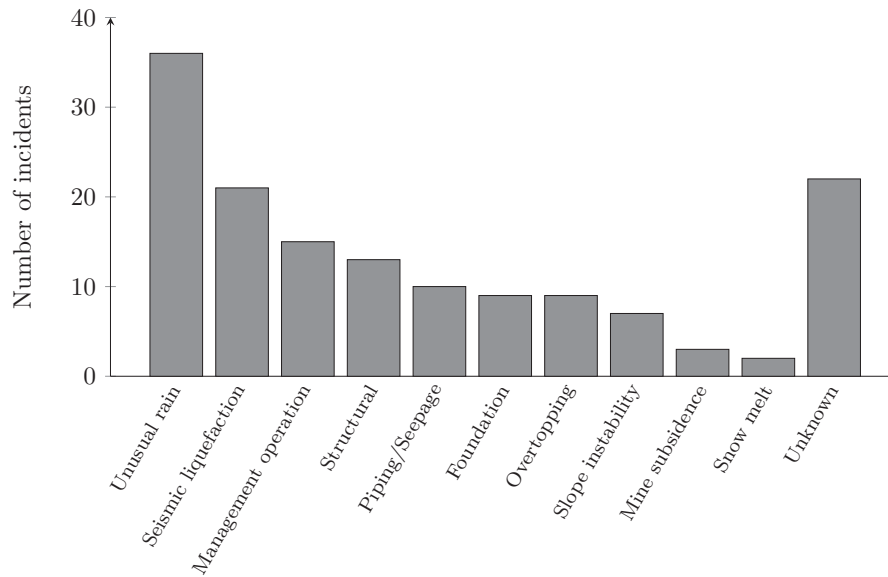


FIGURE 1.5: Causes of registered tailings dams failures from 1917 to 1989. [Data after Rico *et al.* (2008)²⁶]

1.4 Scientific framework

Research done on the weathering of overburden waste rock dumps and tailings ponds, mostly focusses on the geochemical aspect that is inflicting pollution of the environment^{11;23;28}. The extent of weathering of overburden waste dumps and tailings ponds is also investigated, for example, by Electrical Resistivity Imaging (ERI)^{29–31} or by hyperspectral remote sensing³². Again, this research is done to quantify the impact on the environment due to Acid Mine Drainage (AMD) and metal contamination.

Besides the environmental impact, weathering is a one of the principal factors influencing the geotechnical parameters that can cause slope instabilities^{2;27;33}. For example, the degradation of the cementation of soils due to chemical weathering can cause slope instabilities as strength properties are reduced³⁴. On the other hand, cementation due to chemical reaction of tailings material may actually increase the slope stability⁹ (chapter 3).

In general, under the influence of weathering processes, soil grains break down into progressively smaller fragments with a decreasing angularity^{2;35;36} (chapter 4). The first consequence is that the angle of repose of the material will decrease. This influence of weathering has been implemented in numerical models for natural hillsides by Uteri (2004)³⁷ and Uteri & Crosta (2011)^{38;39} and for artificial slope by Huisman (2006)⁴⁰ and Huisman *et al.* (2006 & 2011)^{41;42}, but has not yet been validated for slopes of overburden waste dumps and tailings dams.

Secondly, the degradation of the grain size and the preferential weathering of less stable minerals (chapter 2) results in smaller particle sizes and a broader particle size distribution, respectively. As a result the voids are filled by the smaller grains, resulting in a lower porosity and a lower permeability of the granular material (chapter 4).

As a consequence, the dams response to a large influx of water can change in time due to the weathering of the tailings material^{9;43}. This may well be another reason behind the relatively large number of rainfall induced tailings dam failures (figure 1.5).

1.5 Scope

Weathering agents (i.e., water and air) mainly have access to the unsaturated zone of a tailings dam. Hence, the aforementioned weathering processes which decreased the porosity and permeability of the material, will affect this region the most^{9;10;28;44}.

Firstly, the shear stress on the dam is increased as (part of) the designed unsaturated zone becomes saturated. As a consequence, the risk of liquefaction of the dam is increased. Specifically upstream-type tailings dams, of which the foundation partially rests on the tailings fines, are notorious for their liquefaction potential. Also, the increase of the phreatic level within the dam may result in failures due to overtopping or piping^{9;10;20}.

Secondly, the shear strength of the unsaturated zone is partially governed by capillary bridges that generate cohesion^{4;45}. Although many studies focus on peak shear strength (i.e., static friction) of granular matter as a function of the degree of saturation⁴⁶⁻⁵⁵, little can be found on the influence of capillary bridges on the residual shear strength (i.e., dynamic friction). Research on the dynamic shear strength does not only give a better fundamental understanding of granular flows, but can also have implications for the stability of slopes in such unsaturated material. Specifically in events where the (static) shear strength is overcome (e.g., earthquakes).

Conventional shear apparatuses (e.g., triaxial tests^{2;56} and direct shear tests^{46;47}) generally lack the ability to shear a granular material over a large distance. Circular shear apparatuses that do offer such displacement (e.g., ring shear tests² and concentric cylinders⁵⁷) lack a well defined position of the shear band⁵⁸.

In this study, a dynamic direct shear box was developed (chapter 5). This shear box was used to shear samples of glass beads with various water contents over displacements up to 19 cm (chapter 6).

The structure of this thesis is as follows: Firstly, the general aspects of decay (weathering and erosion) of rock and soil are treated in chapter 2. Chapter 3 presents how tailings dams are constructed, the tailings material characteristics, and what decay processes can be expected. This includes fieldwork observation of tailings from the RTB copper mine in Bor (Serbia) that was visited and studied by the author (section 3.3). Chapter 4 discusses the influence of weathering on the hydrological conditions in the unsaturated zone of a slope in granular material (e.g., a tailings dam), where capillary bridges may govern the shear strength. Chapter 5 discusses the experimental setup that was built by the author to investigate the influence of these capillary bridges on both the peak shear strength (i.e., static friction) and residual shear strength (i.e., dynamic friction). The results are presented in chapter 6. Finally, chapter 7 concludes the thesis and provides recommendation for improvements and future work.

Decay: Weathering and erosion

This chapter discusses the general aspects of weathering (section 2.1), erosion (section 2.2), and the factors that control the intensity and rate of decay (section 2.3). It is written as a brief summary of the subjects, which are requisites for understanding part of this thesis. The decay of tailings is treated in the next chapter (Chapter 3) and that of the material in an overburden waste dump in Appendix A.

Ground- and rock mass decay is part of the cycle in which soil and rock deteriorate^{3;59}. Huisman (2006)⁴⁰ defines decay as the combined action of weathering and erosion, which can be observed at slopes in rock and groundmasses in the form of increasing numbers of discontinuities, gullies, slumps, landslides, etc.

Erosion and weathering are both natural processes that occur since the very existence of our planet, shaping it as it is today. Nowadays human (geotechnical) activities can change the balance of these processes and, hence, alter the speed of decay. Especially when decay is accelerated, the consequences can be catastrophic. Examples are the failures of slopes^{60;61} or the boosted release of weathering products in nature with disastrous effects on the surrounding ecological system. Examples can be found in De Mulder *et al.* (2012)⁶² (e.g., pages 32 & 73), and in figure 3.10 of this thesis, which shows the release of Acid Mini Drainage due to pyrite oxidation in a tailings dam.

To account for the decay of slopes in a geotechnical context, three main processes can be distinguished⁴⁰:

1. Weathering,
2. Erosion, and
3. Redistribution of stress and strain throughout the material due to changes induced by, for instance, excavation or weathering and erosion.

These processes are interrelated, i.e., they may mutually depend on each other. For example, weathering will reduce the geotechnical properties of the material, potentially enhancing erosion. In turn, the removal of this material by erosion alters the stress and strain distribution of the material and exposes new (unweathered) material to the atmosphere, which increases weathering rates.

2.1 Weathering

Weathering is classically regarded as the general process in which rocks are broken down into soil and substances that can be dissolved⁵⁹. However this definition only considers rock as susceptible to weathering. More correct is to include soils. Soil particles, structure, and texture can also change under influence of weathering, e.g., soil grains becoming smaller due to fracture forming, unstable minerals falling apart, and reduction of angularity².

Weathering is defined by Bland & Rolls (1998)⁶³ as “the alteration by chemicals, mechanical, and biological processes of rocks and minerals, at or near the Earth’s surface, in response to environmental conditions”. How near to the surface these processes occur is dependent on the environment at surface, i.e., temperature and humidity, the flow of groundwater through discontinuities and intact rock, the dissolved chemicals in the groundwater, and the preferential weathering of its different lithological units^{62;64}.

The processes underlying weathering can be divided into three categories:

1. *Physical weathering* caused by cyclic processes (e.g., wetting–drying or freeze–thaw cycles) or static processes (e.g., expansion caused by crystallisation of salts).
2. *Chemical weathering* due to reactions with water and/or gas including the air (e.g., dissolution and oxidation).
3. *Biological or biotic weathering* caused by living organisms, like plants, bacteria, algae, lichens, and fungi.

As biological agents weather groundmasses by either physical (e.g., expanding plant roots) or chemical means (e.g., excretion of acids by bacteria), often only physical and chemical weathering are described in the literature^{40;59;65}. In this thesis though, a brief section will be dedicated to biotic weathering processes (section 2.1.3) after physical and chemical weathering is treated in sections 2.1.1 and 2.1.2, respectively.

Although the distinction can be made in the type of weathering, these processes often influence each other. In general, weathering processes tend to enhance one another, resulting in a cascade that ultimately transform ground material into soil that exists of only the most (chemically) stable minerals of the parent rock, e.g., quartz.

For instance, physical weathering results in a progressively smaller segments⁶², effectively increasing the total surface area of the rock or soil. Hence, the total surface exposed to chemical weathering is increased. On the other hand, chemical processes weaken cracks and discontinuities aiding physical processes to tear the rock in smaller pieces. This combined weathering can widen cracks, which give access to water with dissolved minerals and weathering products, e.g., residual soil. Biotic weathering also enhances both physical and chemical weathering processes, which is explained in section 2.1.3.

2.1.1 Physical weathering

Physical, or *mechanical*, weathering is the *disintegration* of a groundmass by stresses that can be either cyclic or static in nature⁴⁰. A static stress environment needs to exceed a certain threshold in order to break down a block of rock or soil grain. Cyclic processes on the other hand do not necessarily have to exceed this threshold. As long as the fatigue limit of the material is reached, disintegration will result⁶⁶. Time may be involved as some rocks are known to break after a stress configuration has been exerted for a certain time span, i.e., creep failure. The magnitude of pressures that can be exerted on a rock during some of these processes are given in table 2.1.

| Physical weathering process | Pressure induced [MPa] |
|-----------------------------|-------------------------|
| Freezing (max. at -20 °C) | 200 ^{63;67} |
| Crystallisation of salt | 7–220 ⁶³ |
| Hydration of salts | 2–20 ⁶³ |
| Clay expansion | 2–2.45 ^{67;68} |

TABLE 2.1: Typical pressure values arising from several processes that cause weathering. Summarised after Bland & Rolls (1998)⁶³, Fookes *et al.* (1988)⁶⁷, and Agus & Schanz (2005)⁶⁸.

Cyclic processes that contribute to physical weathering are:

Freeze and thaw cycles A feature of water is that it expands when it freezes or *solidifies*⁶⁹. Whenever this expansion is confined, e.g., within pores or discontinuities, this may cause large stresses that can disintegrate the ground material (table 2.1). This is called freeze–thaw weathering, but is also referred to as frost weathering/shattering/wedging/cracking/bursting or gelifraction.

Whether a material is susceptible to freeze-thaw weathering depends on the material properties, such as pore size, permeability, discontinuity geometry, and toughness. Also environmental conditions play a major role, e.g., temperature gradient, water availability and salinity⁶³. An example of rock that failed due to frost weathering is shown in figure 2.1(a).

Wetting and drying cycles Wetting and drying causes many ground materials to swell and shrink, which may lead to cracking and flaking. As every mineral has its own swelling capacity, differences between expansion rates of the material’s constituents may lead to high pressures internally. Especially the presence of clay minerals, structural weaknesses, and a low tensile strength, are characteristics of a material that is vulnerable to weathering by wetting and drying cycles. Swelling of clay minerals can build up pressures up to approximately 2.5 MPa⁶⁸ (table 2.1). For example, shale is known to be very susceptible to this type of weathering⁶³. Clay soils are also prone to crack during dry periods, allowing easy access of water during a subsequent wet period⁶⁵.

Insolation weathering Insolation weathering, which is also referred to as thermal fatigue or *thermoclastis*, incorporates the same principle as the other cyclic processes: It causes the ground to expand during heating and contract while cooling down^{63;70}. The vulnerability of ground material to insolation weathering is dependent on its environmental conditions and thermal characteristics, e.g., albedo (surface reflectivity), thermal conductivity, and coefficient of thermal expansion.

The two key environmental variables that play a role in insolation weathering are the *temperature range*, i.e., $T_{\max} - T_{\min}$, and the *rate of temperature change*, i.e., $\partial T(t)/\partial t$ ⁶³. High day-to-day changes and rates due to solar heating and subsequent cooling are mostly measured in extreme environments like deserts and the polar regions⁶³.

Bush fires can easily heat a rock up to 500 °C within 10 minutes, causing a so-called *thermal shock* as the rock cannot cope with the high rate of deformation, i.e., the rock fails⁷¹. From the prehistoric times until the Middle ages thermal shocks were used to mine for minerals (so-called *fire-setting*)⁷².

Figure 2.1(b) shows an example of thermal fatigue, which is distinctly different from cracks due to other cyclic processes. Fractures caused by insolation do not necessarily follow the natural planes of weakness (discontinuities). In other words, fractures are governed by the temperature gradient, but will partially follow present intrinsic weaknesses of the rock, i.e., internal (incipient) discontinuities.



(A) Frost wedging of a granite boulder (Yosemite National Park (CA), USA). [S. Rayfield, Science Source]



(B) Thermal fatigue of a rock (Andes, Argentina). Notice that the fractures do not follow the planes of weakness, i.e., discontinuities. [K. Hall⁷¹]

FIGURE 2.1: Frost and thermal weathering in the field. Note that in contrast to frost wedging, cracks formed by thermal weathering do not necessarily follow the natural planes of weakness.

Examples of weathering due to non-cyclic processes are:

Salt weathering In a similar fashion as freezing water, salts can weather rocks by exerting an expansion stress when they crystallise or hydrate. Dissolved salt enters the ground via pores and discontinuities, where it crystallises *in situ* when the solution becomes oversaturated, i.e., a decrease of the mineral's solubility as water evaporates or temperature decreases. During hydration a mineral assimilates a water molecule and expands as a consequence (section 2.1.2). Salt weathering can cause pressures up to 20 MPa when it hydrates, and 220 MPa as it crystallises (table 2.1).

This type of weathering is often found near coastal cliffs, where saline water is easily deposited in preexisting cracks. Subsequently, it will crystallise causing the rock to show typical honeycomb-like structures⁷³, as shown in figure 2.2.



FIGURE 2.2: Honeycomb weathering of sandstone, due to expanding salt crystals. The exposure is about 7 km from the Mediterranean (Buntsandstone, Mare de Déu de la Roca, Montroig del Camp, Catalunya, Spain). [Hanneke Arnoldus, 2011]

Pressure release Ground material that is at surface today, may have been formed many years ago under high compressive stresses at large depths. During their migration upward, by tectonic uplift and surface erosion, these stresses have reduced, causing a stress-strain redistribution within the material. This results in an expansion in the direction of the stress reduction⁴⁴.

This expansion in the direction of stress reduction is often regarded as the main mechanism behind sheet jointing or *exfoliation* that is often found parallel to the unloading surface⁷⁴, e.g., in figure 2.3. Yet, it needs to be emphasised it is not a generally accepted explanation, as some scientists regard exfoliation as the result of insolation weathering^{59;75}. In the latter, exfoliation occurs due to inequalities between thermal expansion coefficients of the different minerals in the rock (see before).



FIGURE 2.3: Exfoliation jointing found at Little Shuteye pass (CA, USA). [J.D. Rogers, Missouri University of Science and Technology]

Abrasion Abrasion occurs when two rock surfaces or soil grains grind one another. This occurs by shearing of rock masses in fault zones, and on the small scale during erosion, for example, stones transported in a river and by wind-blown sand⁴⁰. It is also a common feature of glacial erosion when blocks of rock in a glacier grind over surrounding rock masses, leading to striation marks⁴⁴.

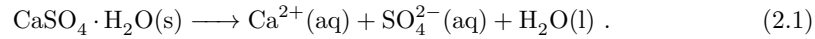
2.1.2 Chemical weathering

Chemical weathering is the *decomposition* of minerals resulting in⁶³:

- Solution of ions and molecules,
- The formation of new minerals, e.g., clay minerals, and
- Release from a rock mass of residual unweathered materials, e.g weathering-resistant minerals such as quartz and gold.

These processes can, and mostly will, occur simultaneously. The most commonly encountered mechanisms of chemical weathering are described below.

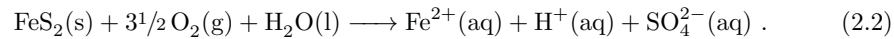
Dissolution Dissolution is a process in which ions are withdrawn from a mineral during contact with water, like kitchen salt (sodium chloride) dissolved in water⁶³. Dissolution mostly affects carbonate and evaporate minerals, e.g., gypsum:



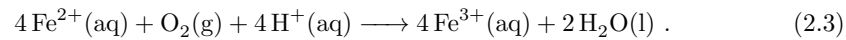
Carbonation occurs when carbon dioxide is in aqueous solution, forming carbonic acid (H_2CO_3). This process occurs whenever water is in contact with the Earth's atmosphere, and can even be enhanced in groundwater due to biological activity.

The solubility of minerals is generally increased with lower pH values. As a consequence, acid rainfall enhances weathering of minerals. A mildly acidic water, e.g., due to carbonation, can form large caves and karst landscapes in limestone bedrocks⁷⁶.

Redox reactions Oxidation (and reduction) are processes that involve the transition of an electron from one element (oxidation) to the other (reduction)⁶³. Redox reactions are favoured by the presence of water. A common example is the weathering of pyrite (FeS_2), which in the presence of oxygen and water decomposes into ferrous iron(II) ions and sulfuric acid:

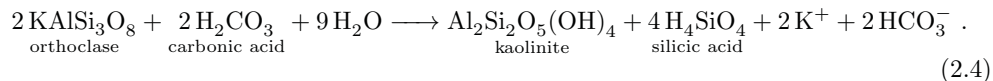


Subsequently the ferrous iron(II) ions can oxidise (possibly aided by bacteria) to ferric iron(III) ions:



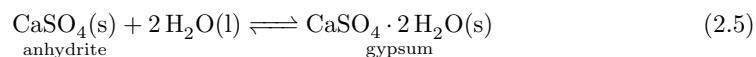
Ferric iron(III) is poorly soluble in water and will precipitate in one of the forms of iron hydroxide $\text{Fe}(\text{OH})_3$, often Goethite, which can alter subsequently in ferric iron(III) oxide (hematite, Fe_2O_3). Goethite/Hematite is often present in iron-rich soils and rock masses, and gives a typical red and brown staining⁷⁷. See, for example, figure 3.10 where Acid Mine Drainage seeping from a (pyrite-rich) tailings dam in East-Serbia.

Hydrolysis During hydrolysis, a water molecule is split in H^+ and OH^- of which either of these ions attaches itself onto a molecule, swapping places with another element or group⁶³. Hence, the molecule and thus the mineral alters. An example is the hydrolysis of orthoclase feldspar under the influence of carbonated water, i.e., carbonic acid:

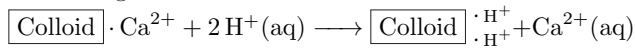


This reaction is also called *kaolinisation* as the clay mineral kaolinite is formed along with silicic acid, bicarbonate ions (HCO_3^-) and potassium ions (K^+)⁵⁹.

(De)hydration Hydration and dehydration are the addition or loss of a water molecule to a mineral molecule, respectively. An important and common example in engineering geology of underground excavations is the hydration of anhydrite into gypsum, resulting in an increase in rock (volume)⁶³:



Cation exchange As the name suggests: Cations (positive ions) in a mineral are swapped with cations that are dissolved in the surrounding liquid because of their smaller hydrated radius and/or higher valency. This often happens on the surface of clay minerals (colloidal particles of diameter $< 2 \mu\text{m}$), which can subsequently alter the clay mineral in both type and characteristics (e.g., plasticity and swelling capacity). Common exchange cations are H^+ , K^+ , Ca^{2+} , Mg^{2+} , and Al^{3+} , which can be present in water that passes through soil or weathering material. A schematic reaction is⁶³:



Chelation Chelation is a chemical phenomenon in which a metal ion is bound to a molecule with multiple ligands (bondings) instead of to normal, single central atom. These chelate complexes are found to be exceptionally stable. As a consequence, the presence of chelating agents (e.g., humic acid) increase the mobility (and thus removal) of metal ions (e.g., Fe^{3+} and Al^{3+}). These metal ions are often products from weathering reactions (e.g., pyrite) and their fast removal enhances further decomposition of minerals. Chelation often occurs in ground where biological (bacterial) activity is present⁶³, e.g., humus.

2.1.3 Biotic weathering

Although all direct causes of weathering are either physical or chemical in nature, it is often enhanced or even inflicted by living organisms. Disregarding their mutual differences, plant roots, lichens, and algae basically share a similar *biophysical* weathering mechanism: They penetrate a material and subsequently expand or contract depending on the moisture content. Hence, they enhance the wetting and drying cycles, as explained in section 2.1.1. In general, it can be stated that the *biophysical* impact is larger for larger organisms, i.e., plants will have a large physical impact than bacteria do⁶³. Humans and animals do not weather rock from day to day and are disregarded in this rule of thumb. Yet, human actions (e.g., mining, slope cutting) and decaying animal matter does contribute to weathering^{11–14}.

Some common occurring *biochemical* weathering processes involve⁶³:

- **Carbonation** of groundwater due to CO_2 excretion by micro-organisms and plant roots.
- Excretion of acids, which enhances the **solubility** of groundwater. Bacteria acidify by the nitrification of ammonia, while lichens, fungi, plant roots, and decay plant and animal matter emit organic acids.
- Organic acids originating from plant roots and/or humus can act as **chelating** agents, increasing the mobility of metal ions (section 2.1.2).
- Some bacteria are known to **oxidise** metals, especially in acid conditions. For example, the *Thiobacillus Ferrooxidans* can achieve much higher oxidation rates of pyrites (FeS_2) than non-biological oxidation, given the right conditions⁷⁸.
- **Sulphate-reducing** bacteria. For example found, during a tunnel boring project in Tehran (Iran). These bacteria were found to produce hydrogen sulfide (H_2S), while they reduce anhydrite (CaSO_4) in the presence of methane (CH_4) (forming H_2S , CaCO_3 , and water). The high amounts of hydrogen sulfide measured during this project were of immediate life danger to the workers in the tunnel⁷⁹.

As shown by the processes described above, many organisms that inhabit soils can have a profound footprint on weathering. Therefore the presence of soil, which is essentially the product of weathering, is in itself a large contributor to its formation⁵⁹.

2.2 Erosion

Erosion is the process in which material is transported from their source by natural agents like gravity, wind, water, snow, or ice⁶². It can be encountered on many scales: From the largest scale where it sculpts Earth's terrain (*glyptogenesis*), to glaciers tearing large blocks from the bedrock, to the wind blowing away the finest particles.

Erosion has a large impact on weathering and its rate, and *vice versa*. Materials that are intrinsically weak or those that have been diminished by (physical) weathering will erode more readily. Also, the removal of weak material exposes the underlying (unweathered) material to weathering agents. Weathering of materials that are being eroded may also occur. Examples hereof are minerals dissolving from matter that is dragged along a stream, or the occurrence of abrasion when the transported materials clash with one another.

Most societies are situated in the non-periglacial zones (figure 2.7). Hence, gravity, wind, and water are the three major erosion processes that are to be taken into account when considering most geotechnical structures or excavations⁸⁰.

Figure 2.4 show three types of water erosion: Sheet, rill, and gully erosion. Sheet wash/erosion is the uniform removal of material as shown in figure 2.4(a), which occurs often in combination with the formation of small channels, called rill erosion [figure 2.4(b)]. Often soil or weak rock is dislodged by the impact of raindrops^{65;81}, after which it is transported along with the water.

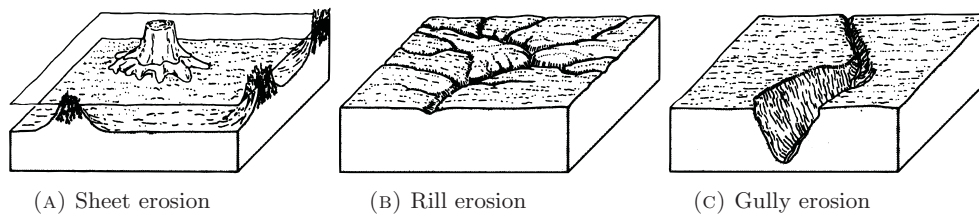


FIGURE 2.4: Types of water erosion. [Modified after Brady (1990)⁶⁵]

Gullies can form when runoff water concentrates in the rills, locally increasing the removal of material. An example of gully erosion on the slope of waste rock dump is shown in figure 2.5. The gullies are formed by water running off the slope, whilst dragging some material along. Also, gravity moves matter that is loosened by rain and wind, forming a scree cover that accumulates at the bottom of the slope. This scree, which is called *talus* or a *colluvial deposit*⁶⁵, is indicated by blue dotted lines in figure 2.5.

In newly made exposures in weak rocks or soils, sheet wash, rill, and gully erosion can be the major factor of decay. For instance in recently made structures like tailings dams, erosion may be dominant over weathering^{40;65}. Yet, in natural slopes that exists for many years and of which the geometry has not changed, weathering most have always altered the geotechnical parameters prior to erosion. It is highly unlikely that such a slope has never been in similar (eroding) conditions, i.e., something most have changed for a grain to get detached.

Figure 3.11(b) shows an example of *wind erosion* forming drop-shaped humps on the crest of a tailings dam in Bor, Serbia. Erosion of mine waste structures is further discussed in chapter 3.



FIGURE 2.5: Gully erosion due to water running off the slope of the Saraka overburden waste rock dump (chapter 3). The talus deposits are situated in between the blue dotted lines. [4th November 2011, Bor, Serbia (44°6'44.3" N; 22°7'32" E)]

2.3 Factors controlling decay

As stated before the combined action of weathering and erosion of a material (i.e., rock or soil) is referred to as its decay. Analogously to a producer and its distributor, respectively weathering and erosion depend on one another. Without the production of erodible material by weathering processes, there is nothing to distribute. On the other hand, when nothing is distributed, the producers warehouse will overflow causing production to slow down. i.e., weathering rates may decelerate when erosion does not remove the weathered material.

Erosion alone may also be intense enough to decay a recently exposed (unweathered) rock or soil layer before significant weathering occurs. In general though, weathering is the producer of erodible material. Hence, a weathering intensity and weathering intensity rate can be introduced to get hold of parameters that control decay.

Weathering intensity is used to indicate a certain degree of decomposition of a material at a specific point in time. The *weathering intensity rate* is the amount of change per unit time^{40;42;63}. Both terms are explained conceptually below in sections 2.3.1 and 2.3.2 below.

2.3.1 Weathering intensity

The intensity of weathering, which essentially is the state of degradation of its geotechnical properties as compared to the 'unweathered material', can be assessed by both qualitative and quantitative means. Qualitative weathering intensities can be determined by measuring:

Mechanical index properties

- Compressive strength,
- Moisture content,
- Porosity, and
- Intensity of discontinuities.

Chemical indices

- Volume change due to dissolution of the material,
- Composition, and
- Amount of weathering-resistant materials, like quartz, as compared to those that are not, e.g., calcite (table 2.3).

Although qualitative measurements are the most comfortable for an engineer to work with, it is often insufficient. Whenever a certain degree or amount of weathering needs to be determined, the unaltered material (e.g., parent rock) needs to be available as a reference. Secondly, the properties of the material do not necessarily give a good description of the weathering intensity of the rock or groundmass as a whole. These techniques can easily lead to misinterpretations for rock masses with deeply penetrating discontinuities and a complex internal hydrology^{40;82;83}.

Since qualitative measurements often deliver unelaborated descriptions of the weathering intensity, verbal descriptive approaches have been developed. Examples of these developed standards are the British Standard (BS 5930:1981)⁸⁴, followed by ISO 14689-1:2003⁶² and BS 5930:1999⁸⁵. BS 5930:1999 is regarded to be more elaborate than its 1981 predecessor, which is the backbone of the ISO standard. As a consequence, ISO 14689-1: 2003 is considered inferior by some^{3;86}. BS 5930:1999 is shown in table 2.2.

TABLE 2.2: Weathering description and classification by BS5930 1999 for rock mass with (A) rocks that are moderately strong to stronger in fresh state; (B) a mixture of strong and weak material; (C) rocks that are moderately weak to weaker in fresh state. [Modified after BS 5930:1999⁸⁵].

| (A) Uniform materials | | |
|---|---|--|
| <i>Grade</i> | <i>Classifier</i> | <i>Description</i> |
| I | Fresh | Unchanged from original state |
| II | Slightly weathered | Slight discolouration; slight weakening |
| III | Moderately weathered | Considerable weakened, penetrative discolouration; large pieces cannot be broken by hand |
| IV | Highly weathered | Large pieces can be broken by hand; does not readily disintegrate (slake) when dry sample immersed in water |
| V | Completely weathered | Considerable weakened; slakes in water; original texture apparent |
| VI | Residual soil | Soil derived by <i>in-situ</i> weathering but having lost retaining original texture and fabric |
| (B) Heterogeneous masses | | |
| <i>Zone</i> | <i>Description</i> | <i>Typical characteristics</i> |
| 1 | 100% grades I-III | Behaves as rock; apply rock mechanics principles to mass assessment and design |
| 2 | >90% grades I-III; <10% grades IV-VI | Weak materials along discontinuities; shear strength stiffness and permeability affected |
| 3 | 50-90% grades I-III; 10-50% grades IV-VI | Rock framework still locked and controls strength and stiffness; matrix controls permeability |
| 4 | 30-50% grades I-III; 50-70% grades IV-VI | Rock framework contributes to strength; matrix or weathering product control stiffness and permeability |
| 5 | <30% grades I-III; 70-100% grades IV-VI | Weak grades will control behaviour. Corestones may be significant for investigation and construction |
| 6 | 100% grades IV-VI | May behave as soil although relict fabric may be still be significant |
| (C) Classification incorporates material and mass features | | |
| <i>Class</i> | <i>Classifier</i> | <i>Description</i> |
| A | Unweathered | Original strength, colour, fracture spacing |
| B | Partially weathered | Slightly reduced strength, slightly closer fracture spacing, weathering penetrating in from fractures, brown oxidation |
| C | Distinctly weathered | Further weakened, much closer fracture spacing, grey reduction |
| D | De-structured | Greatly weakened, mottled, lithorelicts in matrix becoming weakened and disordered, bedding disturbed |
| E | Residual or reworked | Matrix with occasional altered random or apparent lithorelicts, bedding destroyed. Classed as reworked when foreign inclusions are present as a result of transportation |

2.3.2 Weathering intensity rate

To what extent (intensity) and at which rate a material will weather is highly dependent on several parameters, which are divided into three categories: Intrinsic, extrinsic (environmental), and geotechnical factors. These are described below in further detail^{40;63}.

Intrinsic

Intrinsic factors include the properties of the parent material, i.e., its mineralogy and the density of pores and fractures. The mineralogy of the parent material affect the intensity of weathering as some minerals are relatively more stable than others. Table 2.3 shows the relative chemical stabilities for some common minerals. Yet, it needs to be borne in mind that the order is not necessarily the same as that encountered in the field as extrinsic conditions may favour the weathering of some minerals over that of others. For example, figure 2.6 illustrates the weathering of granite containing biotite, feldspar, magnetite, and quartz minerals. In that case quartz is the most chemically stable mineral, hence, its weathering rate will be much lower than that of biotite, feldspar, and magnetite.

The crystal structure determines the parent rock's resistance to cracking and fragmentation. If the rock has many pores and fractures it is easier to be accessed by weathering agents, i.e., water, which increases the rate of chemical processes⁶³.

TABLE 2.3: Relative stability of several minerals after Grotzinger & Jordan (2010)⁵⁹.

| Mineral | Rate of weathering |
|----------------------------------|-------------------------|
| Iron oxides (hematite) | Slowest ↓ Fastest |
| Aluminium hydroxides (gibbsite) | |
| Quartz | |
| Clay minerals | |
| Muscovite mica | |
| Orthoclase feldspar | |
| Biotite mica | |
| Sodium-rich plagioclase feldspar | |
| Amphiboles | |
| Pyroxenes | |
| Calcium rich plagioclase | |
| Olivine | |
| Calcite | |
| Halite (NaCl) | |

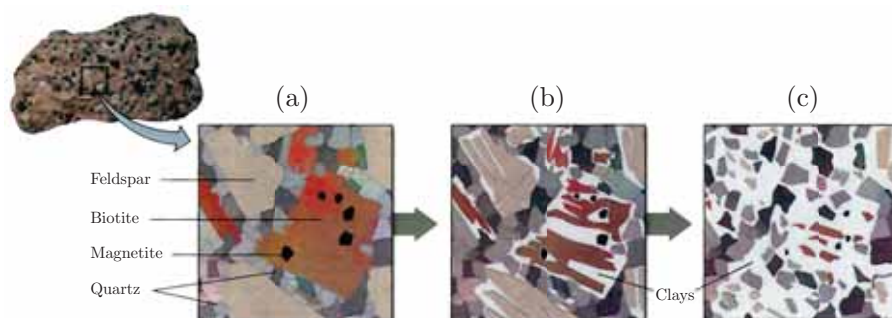


FIGURE 2.6: Diagrammatic illustrative views of stages of granite weathering. (a) Granite is made of several minerals that decay at different rates. (b) Cracks form along the crystal boundaries. Most minerals start to decay into clays, except for quartz which is the most resistant. (c) Weathering continues to weaken and disintegrate the rock. [Modified after J. Grotzinger & T.H. Jordan⁵⁹/Ramón Rivera-Moret, Harvard Mineralogical Museum (scales not indicated)]

Extrinsic (environmental)

Extrinsic factors are influences from outside the material itself⁶³, such as:

- Climate,
- Chemistry of weathering solutions,
- Geomorphology,
- Hydrology. and
- Biotic processes.

As the term ‘weathering’ suggests, climate is an important factor controlling its intensity rate⁶³. Figure 2.7 shows a basic map of the world divided in humid tropical, arid, temperate, and periglacial zones.

Higher temperatures tend to increase chemical weathering rates by, for example, higher solubility of minerals. In general, a 10 °C increase fastens chemical weathering by a factor two. Hence, weathering rates in tropical climates can be about 10 times higher than observed in periglacial zones, given the same conditions^{63;87}. In periglacial zones though, the harsh environments induces frost weathering and high temperature gradients (insolation weathering). In summary, colder climates are found to result in higher physical weathering rates due to frost action, while humid tropical zone have higher chemical weathering rates^{40;80}.

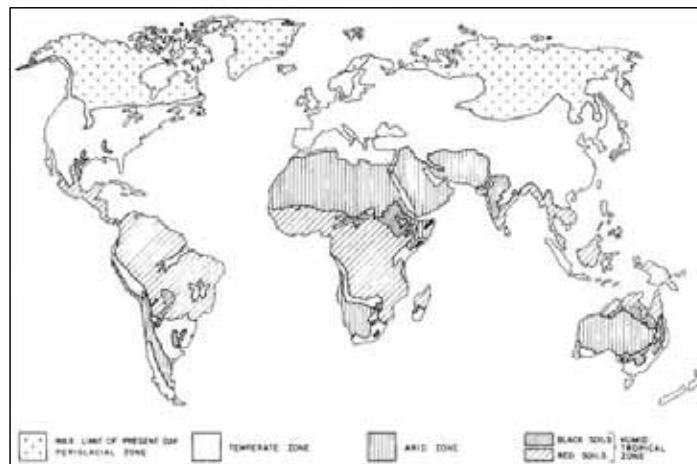


FIGURE 2.7: Basic map of the World distinguishing four climates. [Modified after Saunders & Fookes (1970)⁸⁰]

Beside the temperature, the acidity of a weathering solution has a large influence on its effectiveness. Acidity is often introduced by carbonation of rainwater (pH: 5.5 - 6.2), emission of sulphur dioxide (SO₂) from fossil fuel combustion, and biotic processes (section 2.1.2). It is not out of the ordinary that all these effects combined can result in water of pH 3.5–5.2⁶³. Some Acid Mine Drainage (AMD) has even been reported to have a negative pH value of -3.6^{88;89}.

For example, Tating *et al.* (2013)¹⁴ found that acid drainage from weathering pyrite that percolates to deeper layers below, e.g., by a downward groundwater flow, leads to even more acid groundwater and acid leaching at those deeper levels.

Water is a prerequisite for (chemical) weathering of a soil or rock to occur. As mentioned above, the intrinsic properties like fractures and pores, determine the access to the ground interior. On the other hand, extrinsic factors like hydrology and geomorphology of the site, determine erosion rates and the availability of weathering agents to a soil or rock⁴⁰.

An easily made mistake is to think that weathering can only affect the visual part of a rock or groundmass. Complex hydrogeological situations can cause weathering at places that are not easily revealed during investigation, e.g., discontinuities, fractures, lithologies of preferential weathering, and impermeable layers. As the weathered zones can act either as aquitards, e.g., due to formation of clays, or aquifers, i.e., pathways for groundwater, it is often hard of to determine the groundwater distribution and flow^{64;74}. For instance, Katongo (2005)⁹⁰ found weathering at deep levels (approximately 2–3 km) of a Zambian copper mine, due to water flowing through a fault.

Geotechnical factors

The geotechnical parameters of an engineered slope or structure can also have major influences on the weathering intensities and rates of the material. The following characteristics give rise to different weathering characteristics⁴⁰:

- Slope geometry and orientation,
- Excavation damage,
- Remedial measures, and
- Land use.

As the naturally determined geomorphological and hydrological features of a slope influence its decay, any (engineered) changes will have its effect on the weathering and erosion rates. Slope aspect, geometry, and height are factors that control the amount of solar radiation, wind erosion, and water interaction. In literature tombstones are often used as an example for the influence of aspect on weathering⁷⁷. As shown in figure 2.8, a single tombstone can be only slightly affected on one side, while the other side is severely weathered.



FIGURE 2.8: The (A) slightly weathered and (B) severely weathered side of a sandstone tombstone dated 1883. The difference is due to the prevailing western winds in the region. [Wymondham Abbey (U.K.), Price (1995)⁷⁷]

Any excavation damage inflicted upon a rock, will enhance its weathering by the introduction of cracks and openings for water. Especially in the case of blasting, rock masses are reduced to small fragments that are also prone to mechanical transport (erosion) and thus exposing faster and more new unweathered material. Secondly, the smaller fragments have a larger

Decay of tailings dams

Decay can have disastrous effects on the shear strength of a granular material and, hence, on the stability a slope in such material. The most common examples of these effects is mass wasting, i.e., landslides and dam failures⁵⁹.

An example of an earth flow with catastrophic consequences is the tailings dam failure of Aznalcóllar (southwest Spain), which is shown in figure 3.1. The breach caused an estimated 1.3 million m³ pyritic (acidic) tailings and another 5.5 million m³ tailings water to flow from the Los Freiles mine to a adjacent river, endangering the Doñana National Park downstream²². Although the mechanism causing the dam failure is still under discussion, preliminary reports show that failure of the foundation of the dam is likely the reason. The foundation consists of blue clay and underlying marl^{91;92}. The clay layer was found to have a lower residual friction angle than anticipated during the design of the dam and could possibly have led to a progressive failure once a threshold shear strength was exceeded⁹².



FIGURE 3.1: Failure of the Los Freiles tailings dam, releasing approximately 6.8 million m³ tailings into the surrounding. The accident took place on 25th April 1998 in Aznalcóllar (Andalusia, Spain). [Alonso *et al* (2010)²²]

A Spanish newspaper (El Mundo (May 19, 1998), reference in WISE-uranium²¹) alleged the brittle clay layer to be the residue of the marl layer, of which the limestone (CaCO_3) was dissolved. This weathering process was supposedly enhanced by the acid attack of the Acid Mine Drainage that resulted from the oxidation of pyritic tailings²¹.

The Aznalcóllar case illustrates how weathering can reduce the stability of slopes in granular material. In particular tailings, which is essentially ground ore that is full of newly exposed minerals that may be unstable under the conditions in the dam, can have very high weathering rates.

This chapter discusses tailings dams in general (Section 3.1), i.e., their construction and material characteristics, and gives an example of a copper mine in Bor (Serbia), that was visited and studied by the author (Section 3.3).

3.1 Tailings dams

3.1.1 Construction

A tailings dam can be constructed similarly to an ordinary water retention dam, as shown in figure 3.2. Although this is a safe way to store any type of tailings, a large disadvantage is that the embankment needs to be constructed completely prior to usage and construction is more complicated and expensive than the tailings dams discussed below. I.e., initial capital costs and amounts of construction material needed are high²⁰.

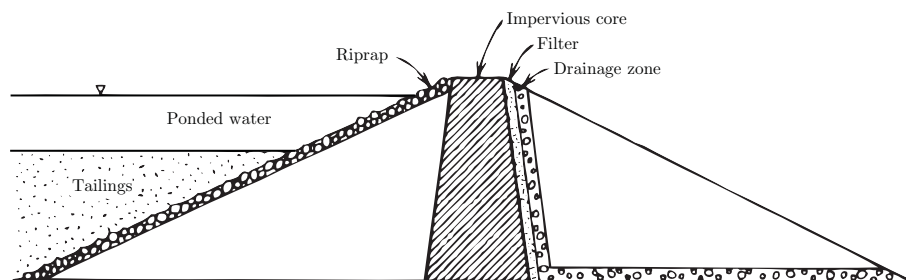


FIGURE 3.2: Construction scheme of a water retaining tailings dam. [Modified after U.S. Environmental Protection Agency (1994)²⁰]

Hence, tailings dams are more often constructed in several stages, of which three different types are distinguished (figure 3.3):

Downstream The subsequent stage is build on top of the downstream side of the dam. The material deposited on the slope needs to be compacted to avoid shear failure²⁰ [figure 3.3(a)].

Upstream The subsequent stage of the dam is build on the crest and beach of the of the previous stage [figure 3.3(c)].

Centerline Centerline is a combination of both, where a subsequent phase is build on top of both the downstream slope and the beach [figure 3.3(b)].

The main advantage is that costs are spread over the full operation time of the TDF. Another major cost reduction of building in stages is that the coarser fraction of the tailings (sand size) can now be used as a source of construction material for the dam itself.

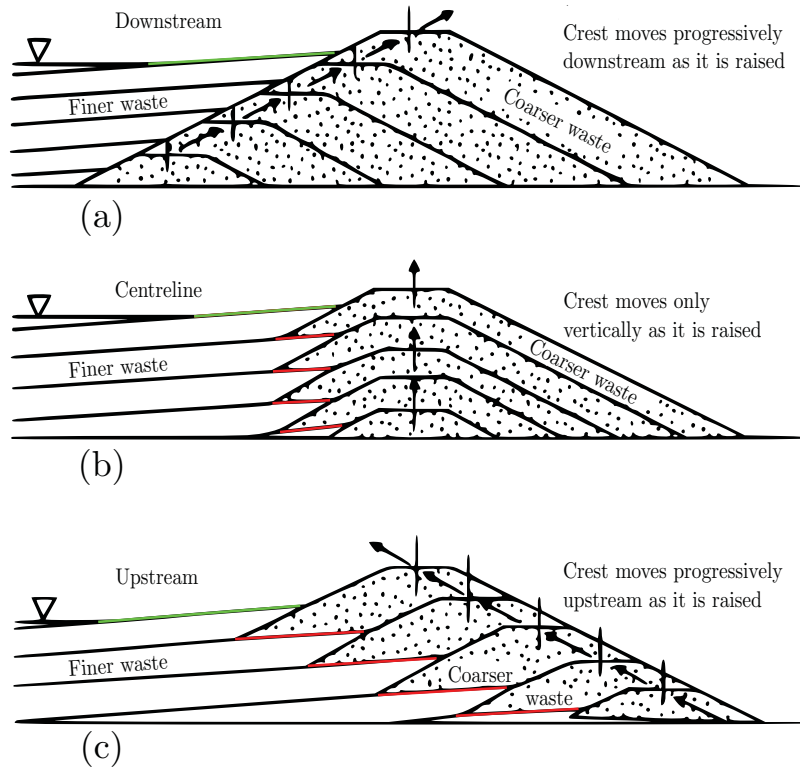


FIGURE 3.3: Construction schemes of phased tailings dams. (a) Downstream type; (b) Centreline type; (c) Upstream type. The current and former beaches are coloured green and red, respectively. [Modified after Blight (2010)¹⁰]

This construction material can be delivered continuously by the use of cyclones, which separates the sand fraction from the smaller silt/clay fraction¹⁰. The layout of a *cyclone* is illustrated in figure 3.4. Its principle is similar to that of a centrifuge: Larger (heavier) particles move to the side, while smaller (lighter) particles move inward. The coarser fraction ends in the lower part of the cyclone and can readily be deposited on the dam, while the finer fraction is captured and directed upward by a second, concentric tube (vortex finder) in the middle. This finer fraction of tailings can subsequently be spigotted from the crest of the dam.

Spigotting is a technique where tailings are discharged through small pipes (spigots) that originate from a tailings main line²⁰. By discharging the tailings by this technique, the finer (lighter) particles end up further away from the dam than the coarser (heavier) ones. This coarser part then forms a *beach* in front of the dam, which can form part of the foundation of a subsequent stage. A coarse beach is essential for upstream and centerline designed embankments to improve drainage and prevent saturation of the embankment.

Oversaturation could lead to excess pore pressures and possible liquefaction of the dam^{10;20}. As guidelines to prevent this from happening, firstly the beach should consist of a minimum of 40 – 60% sand size material. Secondly, raising the dam should not be too fast. Typically 4.5–9 m per year allows the tailings to consolidate and dissipate excess pore pressure. Raising the embankment faster than 15 meters per year is regarded as very hazardous²⁰.

It needs to be emphasised that the upstream-type construction accounts for 78% of 147 reported tailings dams failures of which the construction method was known by Rico *et al.* (2008)²⁶. This is disputable figure as it is also the most used method. Yet, upstream-type

tailings dams are more susceptible to liquefaction as foundations of subsequent phases are build on finer tailings [see figure 3.3(b)]^{18;93-95}. Hence, in most countries that have seismic activity, a downstream construction scheme is preferred or even required.

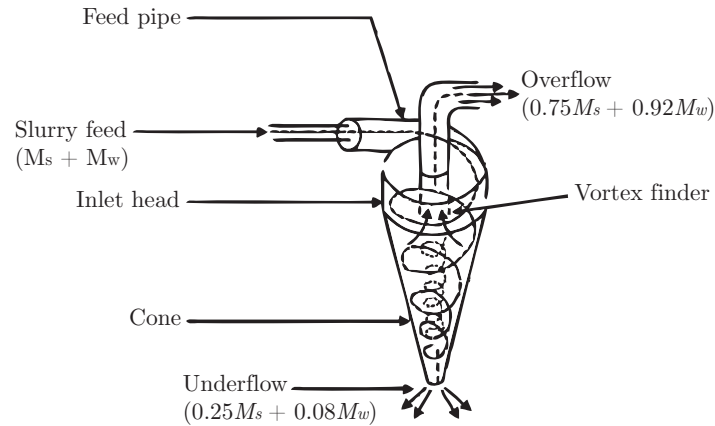


FIGURE 3.4: Drawing of the principle behind a cyclone, which used to separate the courser and fine fraction of tailings. The slurry of tailings from the factory (with solids mass M_s and water mass M_w) are fed into the feed pipe, which leads to the inlet head. The coarser fraction is moved outwards, ending the underflow (typically 25 % of the solids and 8 % of the water). The finer fractions is moved upward via the vortex finder, ending in the overflow. [Modified after Blight (2010)¹⁰]

3.1.2 Material characteristics

Tailings are the residual waste after all commercial valuable minerals are extracted from the ore. After processing tailings consists of⁹:

1. Process chemicals, e.g., flotation reagents, modifiers, flocculants, coagulants, hydrometallurgical reagents, and oxidants,
2. Tailings liquids, i.e., tailings water, and
3. Tailings solids.

Tailings solids consist of material with particle size typically ranging from fine silt- to course sand-sized particles ($2\ \mu\text{m}$ to $2\ \text{mm}$), that do not only consist of the minerals of the original orebody⁹. It is often a mixture of:

- Primary ore and gangue minerals,
- Secondary minerals formed during weathering,
- Chemical precipitates formed during and after mineral processing, and
- Chemical precipitates formed after disposal in the storage facility.

Laboratory research with weathering tailings in a leachate apparatus conducted by Devasahayam (2007)³⁶, indicates that the mean particle size of pyritic tailings (from a coal mine) decrease over time. Devasahayam measured an increasing amount of particles, which is likely caused by the combined effects of physical and chemical weathering.

3.1.3 Weathering

Secondary minerals resulting from post-mining weathering of sulfidic tailings are [after Lottermoser (2010)⁹ (table 2.5, p. 71)]:

1. Sulfates, e.g., jarosite ($\text{KFe}_3(\text{SO}_4)_2(\text{OH})_6$),
2. Oxides, hydroxides, and arsenates, e.g., goethite ($\alpha\text{-FeOOH}$),
3. Carbonates, e.g., calcite (CaCO_3),
4. Silicates, e.g., kaolinite ($\text{Al}_2\text{Si}_2\text{O}_5(\text{OH})_4$), and
5. Native elements, e.g., sulfur (S) or copper (Cu).

Acid Mine Drainage (AMD)

Metallic ore deposits, such as Au, Cu, Fe, Ni, Pb, U, Zn, are often correlated to abundant sulfides, e.g., pyrite (FeS_2) and covellite (CuS). When these sulfidic minerals are processed and disposed as mine waste, they are exposed to the environment. As a consequence, these minerals start to weather (oxidise), which causes the generation of Acid Mine Drainage (AMD). Examples of AMD generating sulfidic minerals are shown in table 3.1. In literature, pyrite is often mentioned as the most common source of AMD (see equation 2.2)^{9–11;28}.

TABLE 3.1: Examples of Acid Mine Drainage (AMD) producing weathering reactions in sulfidic mine wastes. [Lottermoser (2010)⁹]

| Mineral undergoing weathering | Chemical reaction |
|--|---|
| 1. Complete oxidation of Fe-rich sulfides | |
| Pyrite and marcasite | $\text{FeS}_{2(s)} + 15/4\text{O}_{2(g)} + 7/2\text{H}_2\text{O}_{(l)} \rightarrow \text{Fe}(\text{OH})_{3(s)} + 2\text{SO}_4^{2-}{}_{(aq)} + 4\text{H}^+{}_{(aq)}$ |
| Pyrrhotite | $\text{Fe}_{0.9}\text{S}_{(s)} + 2.175\text{O}_{2(g)} + 2.35\text{H}_2\text{O}_{(l)} \rightarrow 0.9\text{Fe}(\text{OH})_{3(s)} + \text{SO}_4^{2-}{}_{(aq)} + 2\text{H}^+{}_{(aq)}$ |
| Chalcopyrite | $\text{CuFeS}_{2(s)} + 15/4\text{O}_{2(g)} + 7/2\text{H}_2\text{O}_{(l)} \rightarrow \text{Fe}(\text{OH})_{3(s)} + 2\text{SO}_4^{2-}{}_{(aq)} + \text{Cu}^{2+}{}_{(aq)} + 4\text{H}^+{}_{(aq)}$ |
| Bornite | $\text{Cu}_3\text{FeS}_4{}_{(s)} + 31/4\text{O}_{2(g)} + 7/2\text{H}_2\text{O}_{(l)} \rightarrow \text{Fe}(\text{OH})_{3(s)} + 4\text{SO}_4^{2-}{}_{(aq)} + 3\text{Cu}^{2+}{}_{(aq)} + 4\text{H}^+{}_{(aq)}$ |
| Arsenopyrite | $\text{FeAsS}_{(s)} + 7/2\text{O}_{2(g)} + 3\text{H}_2\text{O}_{(l)} \rightarrow \text{FeAsO}_4 \cdot 2\text{H}_2\text{O}_{(s)} + \text{SO}_4^{2-}{}_{(aq)} + 2\text{H}^+{}_{(aq)}$ |
| Fe-rich sphalerite | $(\text{Zn,Fe})\text{S}_{(s)} + 3\text{O}_{2(g)} + \text{H}_2\text{O}_{(l)} \rightarrow \text{Fe}(\text{OH})_{3(s)} + \text{SO}_4^{2-}{}_{(aq)} + \text{Zn}^{2+}{}_{(aq)} + 2\text{H}^+{}_{(aq)}$ |
| 2. Precipitation of Fe^{3+} and Al^{3+} hydroxides | |
| Iron hydroxides | $\text{Fe}^{3+}{}_{(aq)} + 3\text{H}_2\text{O}_{(l)} \leftrightarrow \text{Fe}(\text{OH})_{3(s)} + 3\text{H}^+{}_{(aq)}$ |
| Aluminium hydroxides | $\text{Al}^{3+}{}_{(aq)} + 3\text{H}_2\text{O}_{(l)} \leftrightarrow \text{Al}(\text{OH})_{3(s)} + 3\text{H}^+{}_{(aq)}$ |
| 3. Dissolution of secondary minerals (Fe^{2+} , Mn^{2+} , Fe^{3+} , and Al^{3+} sulfate and hydroxysulfate salts) | |
| Halotrichite | $\text{FeAl}_2(\text{SO}_4)_4 \cdot 22\text{H}_2\text{O}_{(s)} + 0.25\text{O}_{2(g)} \rightarrow \text{Fe}(\text{OH})_{3(s)} + 2\text{Al}(\text{OH})_{3(s)} + 13.5\text{H}_2\text{O}_{(l)} + 4\text{SO}_4^{2-}{}_{(aq)} + 8\text{H}^+{}_{(aq)}$ |
| Römerite | $\text{Fe}_3(\text{SO}_4)_4 \cdot 14\text{H}_2\text{O}_{(s)} \leftrightarrow 2\text{Fe}(\text{OH})_{3(s)} + \text{Fe}^{2+}{}_{(aq)} + 8\text{H}_2\text{O}_{(l)} + 4\text{SO}_4^{2-}{}_{(aq)} + 6\text{H}^+{}_{(aq)}$ |
| Coquimbite | $\text{Fe}_2(\text{SO}_4)_3 \cdot 9\text{H}_2\text{O}_{(s)} \rightarrow 2\text{Fe}(\text{OH})_{3(s)} + 3\text{H}_2\text{O}_{(l)} + 3\text{SO}_4^{2-}{}_{(aq)} + 6\text{H}^+{}_{(aq)}$ |
| Melanterite | $\text{FeSO}_4 \cdot 7\text{H}_2\text{O}_{(s)} + 0.25\text{O}_2 \rightarrow \text{Fe}(\text{OH})_{3(s)} + 4.5\text{H}_2\text{O}_{(l)} + \text{SO}_4^{2-}{}_{(aq)} + 2\text{H}^+{}_{(aq)}$ |
| Jurbanite | $\text{Al}(\text{SO}_4)(\text{OH}) \cdot 5\text{H}_2\text{O}_{(s)} \rightarrow \text{Al}(\text{OH})_{3(s)} + 3\text{H}_2\text{O}_{(l)} + \text{SO}_4^{2-}{}_{(aq)} + \text{H}^+{}_{(aq)}$ |
| Jarosite | $\text{KFe}_3(\text{SO}_4)_2(\text{OH})_{6(s)} + 3\text{H}_2\text{O}_{(l)} \rightarrow \text{K}^+{}_{(aq)} + 3\text{Fe}(\text{OH})_{3(s)} + 2\text{SO}_4^{2-}{}_{(aq)} + 3\text{H}^+{}_{(aq)}$ |
| Alunite | $\text{KAl}_3(\text{SO}_4)_2(\text{OH})_{6(s)} + 3\text{H}_2\text{O}_{(l)} \rightarrow \text{K}^+{}_{(aq)} + 3\text{Al}(\text{OH})_{3(s)} + 2\text{SO}_4^{2-}{}_{(aq)} + 3\text{H}^+{}_{(aq)}$ |

Cementation

The previously mentioned formation of secondary minerals by weathering, does not only generate AMD, but can also cause cementation of the tailings. During sulfide oxidation and carbonate dissolution, *coatings* can be formed that enclose the acid producing minerals and, hence, inhibit further weathering⁹⁶.

Also, so-called *hardpan layers* can be formed during precipitation of the secondary minerals⁹. These hardpan layers can form on the surface or at a certain depth of tailings dams and overburden waste dumps (figure 3.5). This layer can be formed at the interface between saturated and unsaturated zone or in the unsaturated zone of a tailings dam⁹⁷.

Coating and hardpans have a significantly lower permeability as compared to the (loose) tailings material⁹⁷. As a result further extension of the oxidation layer can be restricted, causing a natural cover of the acid generating tailings below.

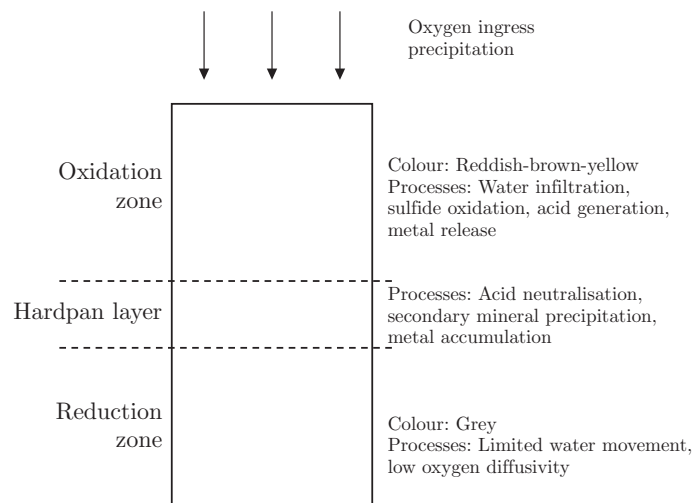


FIGURE 3.5: Formation of a hardpan layer of cemented tailings. Secondary minerals (hydroxides, sulfates, and sulfides) precipitate below the zone of oxidation, e.g., the water table, giving a vertical colour change from reddish-brown-yellow (oxic layer) to grey (anoxic layer). [Modified after Jambor *et al.* (2006)⁹⁸, ref. in Lottermoser (2010)⁹¹]

3.1.4 Erosion

As tailings consist of fine material, it can easily be picked up by wind. Although the dam itself is constructed from the coarser part, much of the finer tailings from the impoundments are blown over the dam and deposited on the leeward side. During the journey over the dam these airborne particles may hit the dam dislodging other particles; effectively sand blasting the dam. This occurs when particles are in *saltation*, which is in between surface creep, i.e., remaining contact with the ground, and full suspension⁹⁹.

Cementation of the tailings material, as explained above, can largely reduce the extent to which erosion can affect the surface of a tailings dam⁹⁷.

3.2 Slope stability

In general terms, failures of a slope made out of granular materials can occur due to³⁵:

- a decrease in shear strength, or
- an increase of the shear stress.

An increased shear stress can be generated by external forces, such as loads on top of the slope, water pressures, and earthquakes. The shear strength of a granular material can be decreased due to³⁵:

- Increased porewater pressures, e.g, due to heavy rainfall.
- Effects of clay minerals, e.g.,
 - Increase of the void fraction, i.e., decrease in bulk density, due to swelling.
 - Realignment of minerals, which decreases the anisotropic shear strength.
- Effects of weathering:
 - Physical weathering: Breaking soil into progressively smaller fragments and a decrease of grain angularity as asperities wear down, i.e., become smaller^{2;35;36}.
 - Chemical and biological weathering: Alteration of the original (often clay) minerals, which may become weaker as a result. However, often chemical weathering may actually strengthen the material, e.g., by cementation (section 3.1.3).

As was described above, tailings material is prone to decay, hence the effects of weathering can have a large impact of the stability of a tailings dam. Physical weathering breaks down the larger soil particles in progressively smaller fragments with a decreasing angularity^{2;35;36}. This may resulting in a decreasing:

1. Angle of repose, and
2. Permeability.

Generally, the *angle of repose* reduces with particle size as shown in figure 3.6⁵⁹. This figure is made under the assumption that the angularity of the grains decreases as well. Although this may often be the case, the angularity of the particles do play an important role in the shear strength of a granular material^{58;100}. As a consequence, the slope of a tailings dam can become too steep because the angle of repose of the slope materials is decreased^{40–42}.



FIGURE 3.6: Typical angles of repose as for granular materials of different size. Note that angularity is not taken into account in this figure. [Modified after Grotzinger & Jordan (2010)⁵⁹]

Secondly, the weathering of some tailings minerals, e.g., pyrite (table 2.3), into smaller fragments, can result in a broader particle size distribution^{36;101}. This increased polydispersity, will increase the packing fraction (ϕ)*, i.e., the bulk density increases as voids in between the larger particles will be filled with smaller ones¹⁰². Also, the physical and chemical attack of asperities will generally decrease the grain-to-grain friction, increasing the packing fraction as a consequence^{4;102}.

* ϕ = ratio of the volume taken by the solids and that of that of the whole sample (section 4.1.1).

Not only affect above weathering processes the shear strength of the dry material, they may also alter the hydrological conditions within a tailings dam. Both the broadening of the particle size distribution and the formation of hardpans result in a lower porosity and, thus, a lower hydraulic conductivity (*permeability*) of the material. This can severely effect the drainage of the dam. With a reduced drainage, excess pore pressures may be difficult to dissipate, which in turn increases the risk of *liquefaction* of the dam^{9;10}.

Another consequence of the decreased porosity is that the same amount of water now further wets the material, i.e., the liquid content increases. The liquid content has a large influence on the cohesion of a granular soil as is illustrated and will be discussed further in chapter 4.

The weathering of tailings in the impoundment may also have major influence on the stability of the dam. Zandarín *et al.* (2009)⁴³ found that the (low) permeability of those tailings cause phreatic levels throughout the tailings disposal facility to fall slowly after rainfall events. Weathering can further decrease this permeability, changing the hydrodynamics of the dam and potentially decrease its stability over time.

In summary, the effects of water are of high importance in the stability of slopes of granular material and these effects can be altered due to weathering, by the means of physical weathering, which breaks down particles in progressively smaller fragments (with lesser angularity) and by chemical weathering which alters the properties of the granular material itself.

3.3 RTB copper mine, Bor, Serbia

Bor region (total area of 3507 km²) is located in the eastern part of Serbia (figure 3.7) and has a population of approximately 123,000 (2011 census¹⁰³). The regional economy has been historically dominated by mining activities, which began with the discovery of copper ore in Bor in 1903. In the post World War II period, the state-owned mining and processing complex of Rudarsko-Topioničarski Basen Bor (RTB Bor) has grown into one of Europe's largest producers of copper and was a flagship of the former Yugoslav industry. The dissolving of Yugoslavia and its accompanied collapse of the socialist economy and lack of investments, have led to a rapid decline of mining operations over the past fifteen years. This had a tragic impact on the regional economy and environmental conditions^{104–106}.

The author has been involved in a project of consulting engineering firm Witteveen+Bos (Deventer, The Netherlands), which comprises of the design of the closure and remediation of Tailings Disposal Facilities (TDFs) and overburden waste dumps in the Bor area. To give an example of the structure and weathering characteristics of an overburden waste dump, observations from fieldwork on Southeast (Ostrelj) overburden waste dump are given in appendix A. This section briefly describes the (weathering) characteristics of the tailings dams in the Bor area.

3.3.1 Project components

The remediation site in Bor consists of two overburden waste dump and three Tailings Disposal Facilities (TDFs) (figure 3.8):

- “Old Bor” TDF,
- Krivelj TDF 1,
- Krivelj TDF 2,
- (East) Saraka overburden waste dump, and
- Southeast (Ostrelj) overburden waste dump.



FIGURE 3.7: Map of Serbia indicating the city Bor in the east by the red circle. Coordinate system and North arrow were not indicated. It is assumed that WGS84 is used, and that the North arrow is pointing straight up. [United Nations Cartographic Section (2007)¹⁰⁷]

3.3.2 Tailings Disposal Facilities (TDFs)

The Krivelj TDFs in Bor are typical valley impoundments, i.e., natural occurring depressions are used to store the tailings. This can be seen from the original, i.e., pre-mining, topology shown in figure 3.12.

In this particular case, the tailings are deposited in a depression formed by a small river (Krivelj river). With this construction two dams were needed down- and upstream of the river, since the tailings level exceeds the natural topography height difference. The river is diverted from the complex through a tunnel called the “kolektor”, which is indicated by a red line that runs north of TDF 1 and through TDF 2 in the maps of figures 3.8 and 3.14. As a guide to the eyes, figure 3.13 gives 3D representation of Krivelj TDF 2 and its dams.

3.3.3 Tailings dams

The tailings dams in Bor are of the upstream-type, which is the oldest and most economic way²⁰. As stated before, the upstream-type dam is also comes with increased risk when it comes to high amounts of rainfall and liquefaction. Therefore an extensive study was done on the stability of Bor’s tailings dams comprising amongst others of boreholes, Cone



FIGURE 3.8: Satellite view of Bor indicating Old Bor TDF (brown), Ostrelj overburden (green), Krivelj TDFs 1&2 (blue) incl. three tailings dams (yellow), Saraka overburden (purple), RTB factory (orange), Kollektor (red), project area border (white). The North arrow is pointing straight up (poorly visible in the top right corner of the image). [Satellite imagery: Google™Earth 2005]

Penetration Tests (CPTU) and laboratory tests by Pachen (2011)¹⁰⁸. To support finding in the field, part of this data is used below.

Particle size

As the easiest available material, the coarser part of the tailings in Bor is separated by cycloning (figure 3.4) to be used as construction material for the tailings dam that retains the impoundment. Hence, the dam consists of the coarsest material, followed by the beach, leaving the remaining (finest) fraction deposited in the impoundment (figure 3.9¹⁰⁸).

The dam itself consists mainly (> 80 %) of fine sand-sized particles between 100 – 300 μm . The beach in front of the dam consists of approximately 45 % sand-, 45 % silt-, and 10 % clay-sized tailings. The fraction of sand-sized grains in the beach is just above the limit (40 %) that it is considered safe as foundation for a subsequent construction phase^{10;20}.

The remaining tailings that are deposited in the impoundment consist of almost only silt and clay fractions, i.e., less than 63 μm .

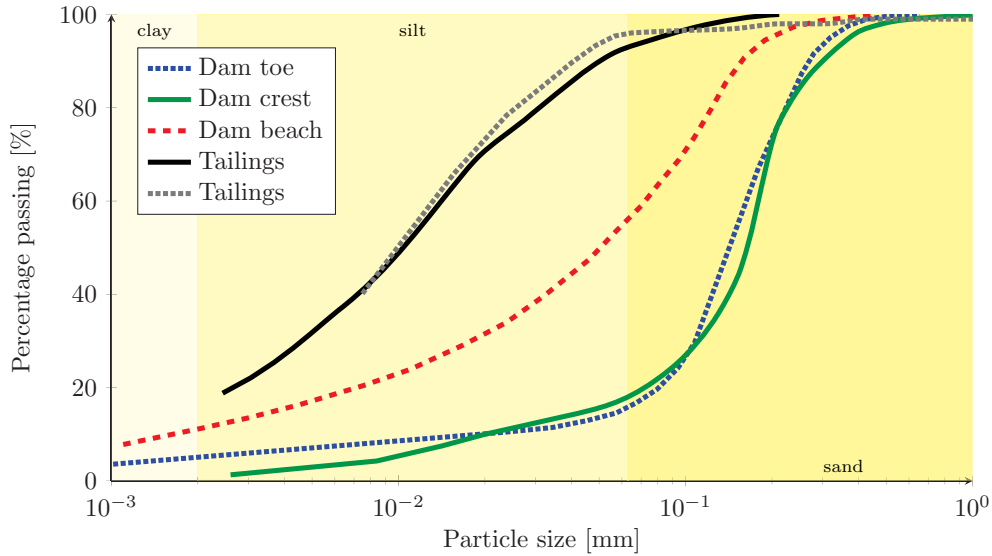


FIGURE 3.9: Particle size distribution of tailings material in Krivelj Tailings Disposal Facility 2 (Bor, Serbia). The tailings material of which the dam is constructed at the surface by the blue line \cdots (D3-B2, depth 1.5-1.9 m) and bulk indicated by the green line — (D3-B5, depth 15.6-20.0 m) is the courser part. The particle size distribution of the finer tailings in the Tailings Disposal Facility are indicated by the black line — (F2-B9, depth 6.0-7.5 m) and grey line \cdots (F2-B15, depth 35.3-35.7 m). The beach in front of the dam consist of a mixture of both the course and fine tailings (--- D3-B6, depth 2.3 m). The location of the boreholes are shown in figure 3.14. [Data by courtesy of Witteveen+Bos (Pachen (2011)¹⁰⁸)].

Decay

Tailings consist of all ore minerals that are left over after extraction, i.e., those that have no economic value and some residual extraction-minerals, as a 100 % yield is never achieved. Hence, many minerals that used to be deep below the surface are suddenly exposed to the environment. Depending on the stability of the exposed minerals, the environmental and geotechnical factors, this may result in high weathering rates (section 2.3.2). The tailings in Bor mainly consist of quartzite and pyrite minerals¹⁰⁸. The latter are very prone to oxidation, which generates Acid Mine Drainage (figure 3.10).

Next to the seepage, weathering is very obvious by the discolouration of the tailings material itself. Figure 3.11(a) shows a dug hole on top of the tailings dam exhibiting the three prevalent colours of the tailings material: Grey, light yellow, and brownish orange. Grey corresponds to the unweathered tailings, as it is similar to that of the newly deposited tailings (e.g., figure 3.4). Light yellow seems to be the (completely) weathered part of the tailings where the iron-oxides have flushed in to parts that have stained brownish orange as a result.

This is in line with figure 3.5, where a hardpan layer is created in between an oxidation (yellow) and anoxic (grey) layer. Cone Penetration Tests conducted in scope of the remediation study, confirming the existence of hardpan layers as increased cone resistance and permeability up to typical depths of 2 m were measured¹⁰⁸.

For the tailings in Krivelj TDF 2 this oxidation layer is typically 20 to 80 cm deep, while for dam 3 four borehole logs suggest that this weathered layer is approximately 1.3 to 1.9 m deep¹⁰⁸. The difference is due to both the accessibility of both water and oxygen to the pyrite grains to start the reaction given in equation 2.2. The tailings in the impoundment are



FIGURE 3.10: Seepage of Acid Mine Drainage (AMD) at the base of tailings dam 1 (Krivelj TDF1). The AMD is the result from pyrite oxidation as given in equation 2.2. This gives rise to the formation of Goethite/Hematite that inhibits the typical brown/red staining of the seepage water. [1st November 2011, Bor, Serbia (44°5'58.3" N; 22°7'48.8" E)]

often submerged, blocking access to oxygen. Secondly, the finer tailings in the impoundment are less permeable than the coarser material of the dam, readily allowing access of water.

Although the dam itself is constructed from the coarser part, much of the finer tailings from the impoundments are blown over the dam and deposited on the leeward side. During the journey over the dam these airborne particles may hit the dam dislodging other particles; effectively sand blasting the dam. On the crest of tailings dam 3, weathered tailings (orange/yellow) were found to be less susceptible to erosion due to cementation or compaction over time (section 3.1.3). As a consequence, drop-shaped humps are formed with weathered (cemented) material facing windward and blown over tailings (finer material from the tailings impoundment) deposited on the leeward side [figure 3.11(b)].



(A) Discolouration of tailings material. [3rd November 2011 (44°5'12.2" N; 22°9'34.7" E)]



(B) Wind erosion on the crest of the tailings dam. [5th March 2011 (44°5'12.3" N; 22°9'35.8" E)]

FIGURE 3.11: Decay on top of tailings dam 3 (TDF2), Bor, Serbia.

Topography of the project area (Bor, Serbia)

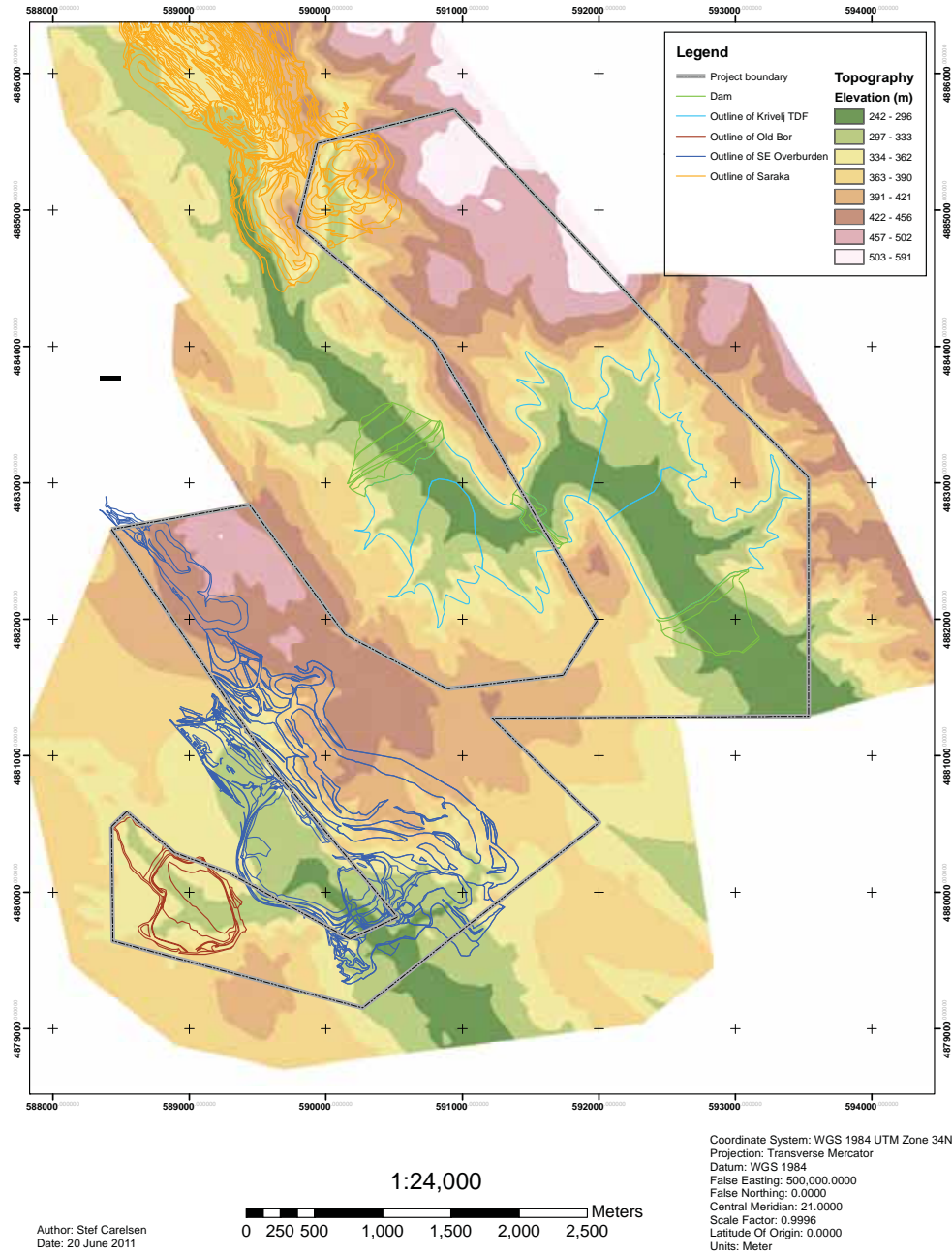


FIGURE 3.12: Topography of the project area (Bor, Serbia). The original topography prior to excavation and the formation of mine waste structures was obtained from maps from 1965 and is shown by the colourmap. The outlines of the various structures in 2011 are shown by several coloured lines, given in the legend. It can be seen that natural depressions, i.e., rivers were used to store the mine waste.

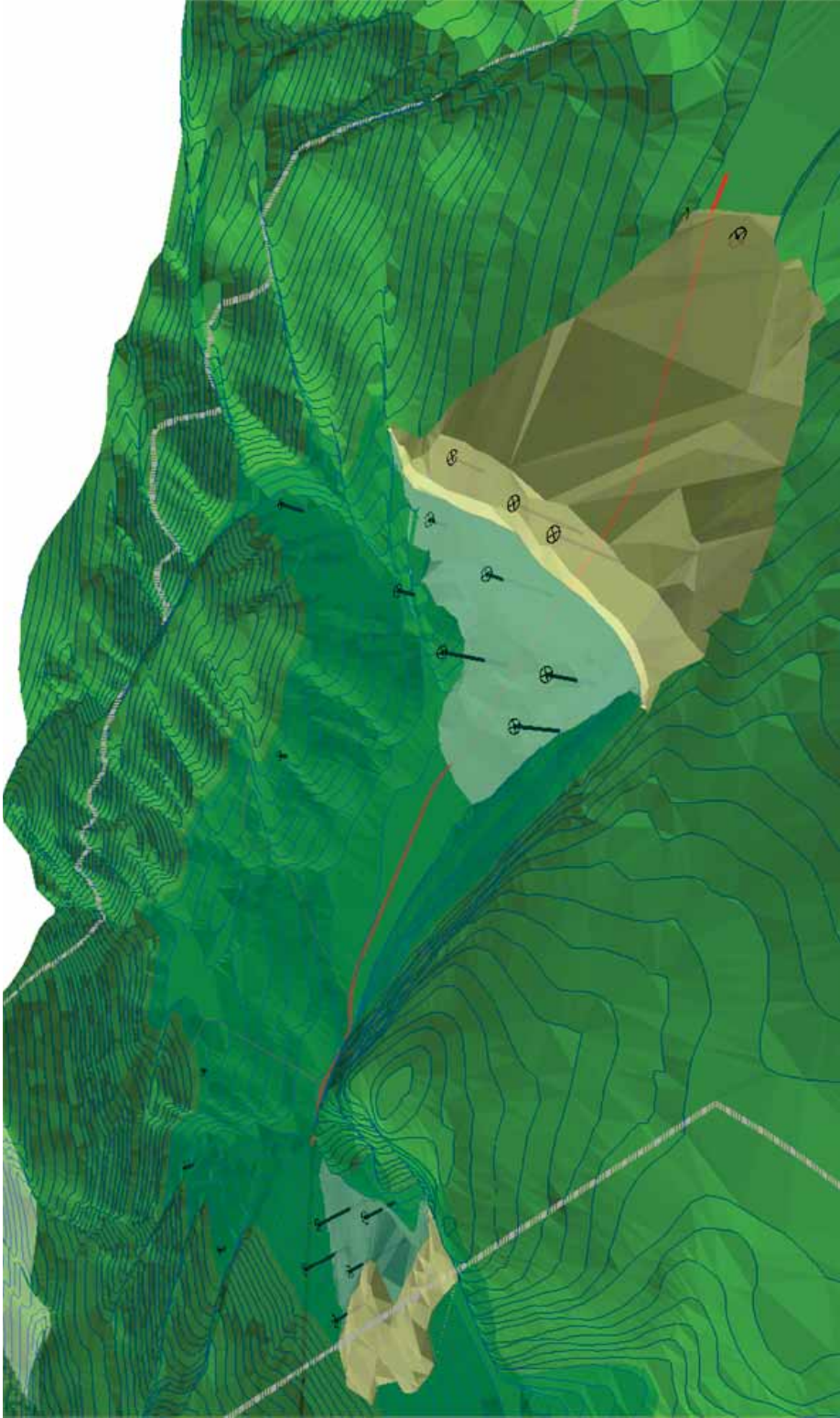


FIGURE 3.13: 3D GIS representation of Krivelej TDF 2 facing North. This was done by triangulating the contours obtained from maps from 1965 (prior to construction) by ArcGIS. Also, the boreholes on Dam 3 and TDF 2, the tunnel diverting the water from the Krivelej river (red), and the project boundary (grey) are visualised.

Krivelj Tailings Disposal Facility 2 (TDF2) - Drillingholes

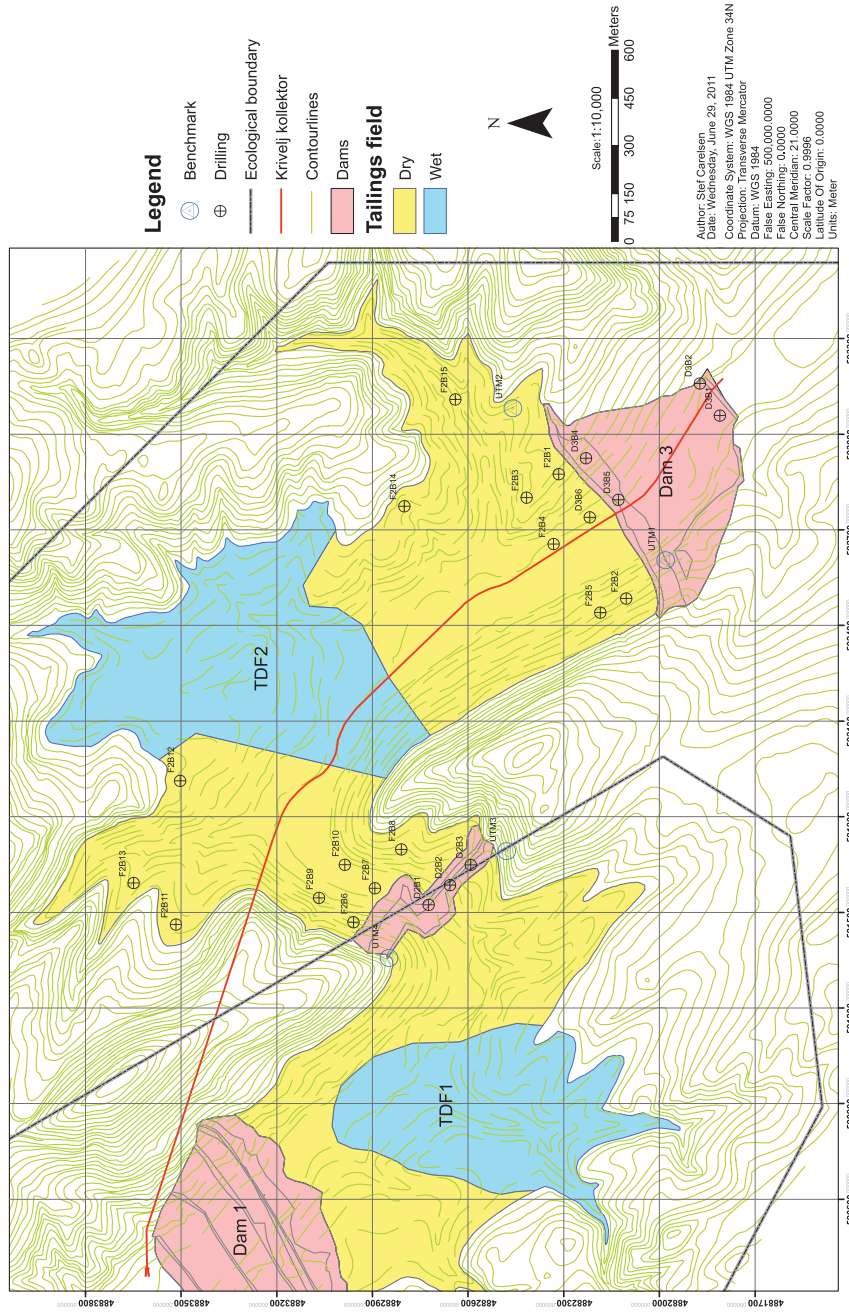


FIGURE 3.14: Overview of the Krivelj Tailings Disposal Facilities (TDFs), consisting of two TDFs and three tailings dams. The tailings are contained in the valley formed by the Krivelj river. The river is diverted through a mountain north from TDF 1 and constructed on the bottom of TDF 2 (red line). The grey line indicates the project boundary. The location of the drillingholes, i.e., boreholes, and their label are indicated.

Liquid content and the shear strength of wet granular matter

Previous chapter explained how the effects of weathering can change the hydrological condition of a slope in weathering granular material, such as tailings dams.

This chapter briefly introduces the general terms used for unsaturated soils or *wet granular matter* in section 4.1. Secondly, it is explained how the shear strength of wet granular matter is governed by negative pore pressures induced by capillary bridges (section 4.2). Finally, section 4.3 introduces the shear strength fundamentals (e.g., coefficient of friction and Mohr-Coulomb failure criterion), with a focus on the dynamical or *residual* shear strength.

4.1 Wet granular matter

This section treats the basics of unsaturated (granular) soils or *wet granular matter* by introducing the different characteristics of the solid phase (section 4.1.1) and that of the liquid phase (section 4.1.2). A wet granular matter comprises three phases as schematically drawn in figure 4.1.

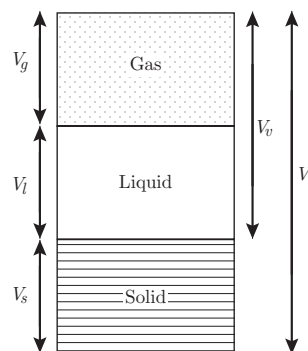


FIGURE 4.1: Volumes of the gas (V_g), liquid (V_l), and solid (V_s) phases in a granular matter sample of volume V . The void volume V_v , which is the sum of V_g and V_l , is also indicated.

4.1.1 Solid phase

The part of the total volume that is occupied by the granular material, is called the *packing fraction*, ϕ , of the material, i.e., $V_s = \phi V_t$. This packing fraction is dependent on material characteristics, such as particle shape, grain-grain friction, and particle size distribution⁴.

Assuming that the grains are monodisperse and perfectly spherical, the packing fraction, ϕ , can be mathematically determined assuming a crystalline arrangement. Also, ϕ has been determined for various unordered (random) arrangements, i.e., amorphous configuration⁴. Table 4.1 give the packing fractions for various crystalline and amorphous configurations.

The theoretical maximum possible packing fraction, which is referred to “Apollonian packings”, is 0.951⁴. This can only be achieved by sequentially adding particles in the interstitial spaces of its larger predecessor, i.e., by making an infinitely broad particle size distribution.

TABLE 4.1: Maximum packing fraction, ϕ , for several crystalline and amorphous configuration of spheres^{109;110}. The coordination number is the number of nearest neighbouring spheres per sphere.

| Arrangement | ϕ | Description |
|---|---------------|------------------------|
| <u>Crystalline</u> | | |
| Simple cubic | 0.52 | Coordination number 6 |
| Body-centered cubic packing | 0.68 | Coordination number 8 |
| Face-centered cubic and hexagonal packing | 0.74 | Coordination number 12 |
| <u>Amorphous</u> | | |
| Random very loose packing | $\simeq 0.56$ | Settled bed |
| Random loose packing | 0.59 – 0.60 | Packed by hand |
| Random poured packing | 0.609 – 0.625 | Poured into container |
| Random close packing | 0.625 – 0.641 | Vibrated bed |

4.1.2 Liquid phase

The volume of voids, $V_v = (1 - \phi)V_t$ (porosity = $1 - \phi$), can be filled by the liquid and gaseous phase, i.e., $V_v = V_l + V_g$.

The packing fraction of the liquid phase or *liquid content* W , can be calculated by^{4;111;112}:

$$W = \frac{V_l}{V_t} = \frac{m_l \rho_s \phi}{m_s \rho_l}, \quad (4.1)$$

where V_l is the volume taken by the liquid phase ($V_l = m_l / \rho_l$, where m_l and ρ_l are the mass and density of the liquid, respectively), and V_t the total volume occupied by the sample ($V_t = m_s / \rho_s \phi$ where m_s and ρ_s are the mass and density of the solids, respectively)⁴. In the field of unsaturated soil mechanics, W is also called the *volumetric water content*⁴⁵.

Another measure is the *degree of saturation*, S , which is the ratio of volume of the liquid phase, V_l , and that of the voids, V_v ⁴⁵. The volume of the voids is given by $V_v = V_t(1 - \phi)$, i.e.:

$$S = \frac{V_l}{V_t(1 - \phi)} = \frac{W}{1 - \phi} = \frac{m_l \rho_s \phi}{m_s \rho_l (1 - \phi)}. \quad (4.2)$$

S expresses what percentage of the voids is occupied by the liquid, i.e., a fully saturated soil has $S = 1$ and no gaseous phase. If the amount of water is even further increased ($S > 1$) the solid phase is in suspension.

4.2 Capillary bridges

As is shown in figure 4.2, the addition of a liquid phase has a large influence on the angle of repose of a granular material. A well-known childhood example is that a sandcastle cannot be made from dry sand^{62;113;114}. Yet, fully saturated sand (mud) will even sustain smaller angles than dry material. This increased shear strength of unsaturated (damp) material is due to the formation of capillary bridges which is explained in next section.

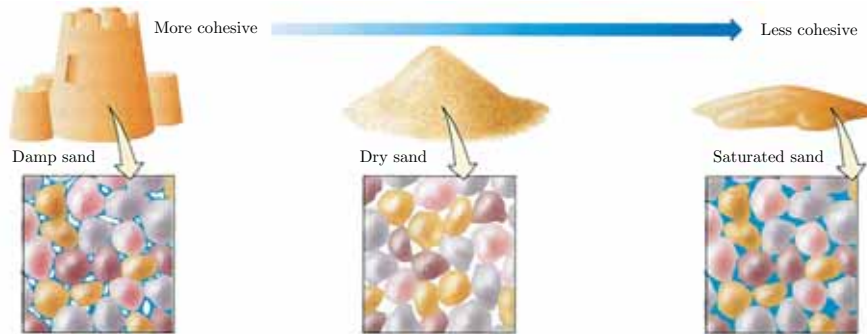


FIGURE 4.2: Effects of liquid content on the cohesion of granular material. Cohesion is generated by liquid bridges in unsaturated (damp) sand. Saturating the soil causes the water to lubricate the grains, which reduces the coefficient of friction. [Modified after J. Grotzinger & T.H. Jordan (2010)⁵⁹]

In an unsaturated soil, water or *capillary bridges* create an attractive force in between particles due to the surface tension (γ) of the liquid^{113;115}. This surface tension induces a pressure difference ΔP over the water-air interface, i.e., the Laplace pressure $P_L = 2/H$, where H is the mean curvature of the capillary bridge. In the field of unsaturated soil mechanics the water-air interface is called the *contractile skin* and the Laplace pressure is often referred to as the *matric suction*⁴⁵.

Figure 4.3 sketches the formation and subsequent separation of a capillary bridge between two equally sized spheres of radius R .

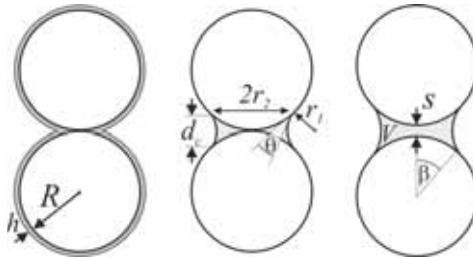


FIGURE 4.3: Geometrical constants of a capillary bridge between two particles of radius R . Left: Two wetted spherical particles with a wetting layer of thickness h . Center: A capillary bridge is formed, which in equilibrium has a constant mean curvature ($H = r_1^{-1} + r_2^{-1}$). θ is the contact angle, which at equilibrium is called Young's angle θ_Y . Right: The particles are separated by a distance s . The bridge volume V and angle β and their dependence on s are explained in Herminghaus (2013)⁴ [S. Herminghaus (2013)⁴]

The force exerted on the two spheres by a single capillary bridge of a liquid with surface tension γ between two equally sized spheres of radius R is approximated by⁴:

$$F_{cb} \approx 2\pi R\gamma \cos \theta , \quad (4.3)$$

where θ is the contact angle of the solid and the liquid that depends on their respective surface energies¹¹⁵. The contact angle for completely wetting surface is equal to zero, while a surface is called hydrophobic when $\theta \leq 90^\circ$, and superhydrophobic when $\theta \leq 150^\circ$.

Hence, assuming a completely wetting surface (i.e., $\theta = 0$), the force of a single capillary bridge F_{cb} is approximately $2\pi R\gamma$.

4.2.1 Energies

From a more physical perspective, the influence of capillarity can be explained by the several energies that play a role in a (wet) granular material. Figure 4.4 shows these energies with as a function of their particle radius r . The formulae used to calculate these energies are given in table 4.2.

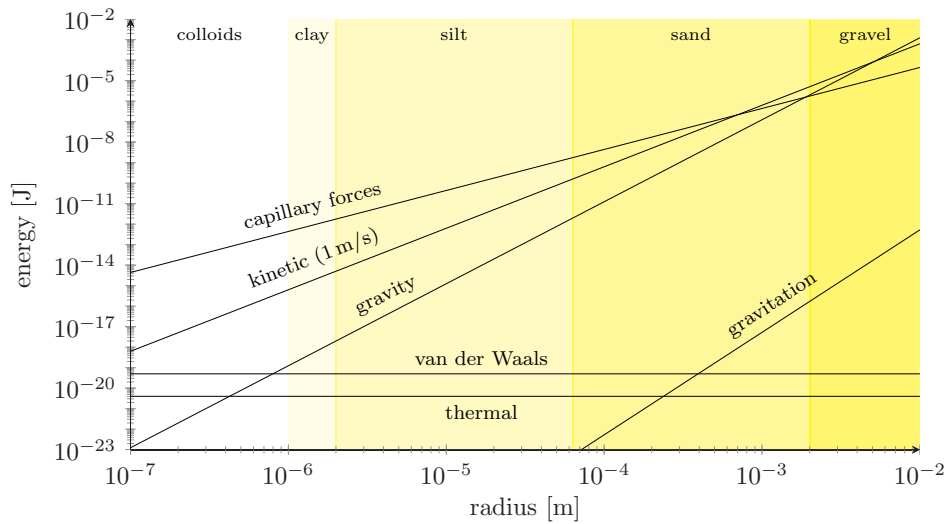


FIGURE 4.4: Energies in granular materials as a function of the particles radii after Herminghaus (2013)⁴. The background color indicate different soil types, from colloidal ($<1\ \mu\text{m}$) to gravel size (2–63 mm) as defined by BS EN ISO 14688-1⁷⁷.

TABLE 4.2: Types of energy in (wet) granular matter and their relation to the particles radius, r . [Herminghaus (2013)⁴]

| Type of energy | Formula | Evaluation in J |
|-----------------------------------|-------------------------------|-------------------------------|
| Van der Waals ($\delta = 0.1r$) | $Ar/12\delta$ | $5 \cdot 10^{-20}$ |
| Gravitation (grain–grain) | $Gm^2/2r$ | $5.3 \cdot 10^{-3} \cdot r^5$ |
| Capillary force | $2\pi r\gamma$ (equation 4.3) | $0.44 \cdot r^2$ |
| Gravity (earth) | mgr | $1.24 \cdot 10^5 \cdot r^4$ |
| Kinetic ($v = 1\ \text{m/s}$) | $1/2mv^2$ | $630 \cdot r^3$ |
| Thermal energy | $k_B T$ | $4 \cdot 10^{-21}$ |

A Hamaker constant¹¹⁶ [$\propto 10^{20}\ \text{J}$]
 G Gravitational constant [$\approx 6.67 \cdot 10^{-11}\ \text{m}^3\text{kg}^{-1}\text{s}^{-2}$]
 g Standard gravity [$9.81\ \text{ms}^{-2}$]
 k_B Boltzmann constant [$\approx 1.38 \cdot 10^{-23}\ \text{JK}^{-1}$]
 m Mass [kg]
 T Temperature [K]
 v Velocity [m/s]
 γ Surface tension [water: $\gamma \approx 72 \cdot 10^{-3}\ \text{Nm}^{-1}$]
 δ Depth of surface roughness [m]

As can be expected, the energies that correlate to van der Waals and thermal (Brownian motion) forces are only significant from colloidal particles¹¹¹. Also, the velocity (i.e., inertia) of the shearing motion can be easily dominant. Yet, in this thesis experiments are done at velocities of 5 mm/s, which are much lower than 1 m/s indicated in figure 4.4.

Hence, from colloidal- to sand-sized particles the dominant energy is that from capillary forces, i.e., the existence of liquid (e.g., water) bridges in between the particles. At larger particle sizes of in the order of millimeters and onward, gravity becomes dominant over capillary forces. The typical lengthscale at which this transition occurs is called the capillary length, κ^{-1} , which is the ratio between the Laplace pressure (γ/κ^{-1}) and the hydrostatic pressure ($\rho g \kappa^{-1}$):

$$\kappa^{-1} = \sqrt{\gamma/\rho g}, \quad (4.4)$$

where γ is the surface tension, ρ the density of the liquid, and g the standard gravity¹¹⁵. The capillary length for water is 2.7 mm*, i.e. for larger particles it can be expected that water will drain by gravity rather than form capillary bridges⁴.

4.2.2 Regimes of wetness

Figure 4.5 show the different regimes that are distinguished in literature^{4;111;117;118}. In the *humidity regime*, an apparent “dry” material will actually have a small liquid film bind to the grains by the van der Waals force. The thickness of this film will be dependent on the humidity of the surrounding air. For low humidity, the film thickness will be in the order of magnitude of the microscopic asperities, where for a large humidity it will be in the order of the (larger) surface roughnesses.

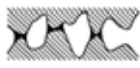




| wetness regime | morphology | liquid content |
|----------------|--|-------------------------------|
| humidity | asperities  | $W = 0.0$ to 0.026 |
| | roughness  | |
| pendular |  | W_{cb} |
| funicular |  | W^* |
| | | clusters 0.026 to 0.08 |
| bubbles |  | bicontinuous 0.08 to 0.28 |
| | | 0.28 to saturation |

FIGURE 4.5: Wetting regimes encountered while increasing the liquid content of granular matter. W_{cb} and W^* indicate the liquid contents at which capillary bridges start to develop and when multiple capillary bridges start to merge into clusters, respectively. [S. Herminghaus (2013)⁴]

When W is increased further, the *pendular* regimes is entered where liquid bridges will form ($W > W_{cb}$), but the surface of the grains is not covered by a liquid film.

*For water: $\gamma \approx 72 \text{ mN/m}$ (25° C), $\rho = 1000 \text{ kg/m}^3$, $g = 9.81 \text{ m/s}^2$

The *funicular* regime is typically entered for $W = W_* > 0.026$ and is characterised by the coalescence of multiple bridges into clusters. Herminghaus⁴ has split the funicular regime up in a cluster and a bicontinuous regime. The first corresponds to the original description of the funicular regime, while in the latter the clusters can become so large that the liquid phase is completely connected throughout the sample (typically from $W > 0.08$).

As the name suggests, in the *bubbles* regimes, the liquid traps the interstitial air ($W > 0.28$). This is different from the bicontinuous regime, where the gaseous phase is still allowed to flow freely through the sample.

It is likely that the shear strength of wet granular matter is dependent on the average number of liquid bridges formed per sphere. This dependence as function of the water content was studied experimentally by Kohonen *et al.* (2004)¹¹² and Scheel *et al.* (2008)¹¹⁹. Figure 4.6 shows the number of capillary bridges (left axis), number of cluster (left side of right axis), and the normalised volume of the largest cluster (right side of right axis) as a function of the water content W .

Figure 4.6 shows the transition from the pendular regime (approximately six liquid bridges per sphere), to the cluster regime, and finally to the bicontinuous regime (where the liquid throughout the sample becomes connected). It is likely that the shear strength will be a function of the number of capillary bridges, and hence, follow a similar trend. Figure 4.6 gives the result for a random loose packing fraction (i.e., for a pile). For higher packing fraction such as ϕ_{rdp} , the number of capillary bridge per sphere will be slightly larger, but a similar trend was observed (figure 6.9 in Herminghaus (2013)⁴).

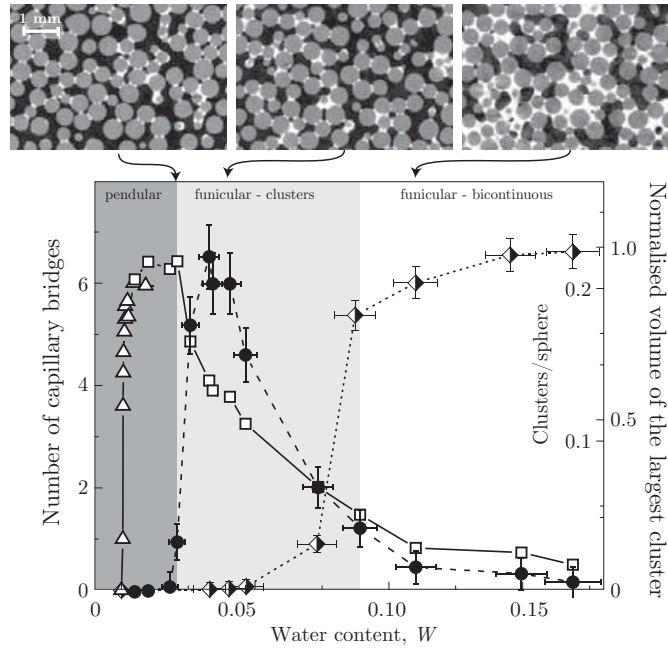


FIGURE 4.6: The number of capillary bridges (left axis), number of cluster [i.e., a connected region of liquid touching more than two glass beads (left side of right axis)], and the normalised volume of the largest cluster (right side of right axis) as a function of the water content W in a wet granular pile ($\phi \approx 0.57$). These numbers were determined by fluorescence microscopy (triangles) and X-ray tomography (squares and circles). The images are slices of 3D tomograms of glass beads (diameter: $280 \mu\text{m}$) at $W = 0.02$, 0.04 , and 0.11 . [Modified after M. Scheel *et al.* (2008)¹¹⁹, wetting regimes are added by the author (figure 4.5)]

4.3 Shear strength

The shear strength of a granular material is the maximum shear stress σ_s which it can sustain under a certain normal pressure σ_n ². The ratio of these stresses is called the *coefficient of static friction* μ ¹⁰². I.e.,

$$\mu = \frac{\sigma_s}{\sigma_n} . \quad (4.5)$$

This coefficient of static friction can be illustrated by placing a (solid) sample on a supporting platform that is slowly tilted (dividing the gravity force into components of the normal pressure and shear stress). The angle at which the sample start to slide is called the *angle of internal friction* ϕ , at which a shear stress $\sigma_s = \sigma_n \cdot \tan(\phi)$. Hence,

$$\mu = \tan(\phi) . \quad (4.6)$$

These shear stresses for which failure occurs can be measured for several normal pressures, resulting in a linear envelope that can be approximated by the *Mohr-Coulomb failure criterion*, i.e.:

$$\sigma_s = \sigma_n \tan(\phi) + c , \quad (4.7)$$

where σ_s is the shear stress, σ_n the (effective) normal stress¹²⁰, ϕ the angle of internal friction, and c the cohesion⁶².

4.3.1 Shear strength of an unsaturated soil

For an unsaturated soil the Mohr-Coulomb failure criterion is extended by Fredlund & Rihardo⁴⁵ comprising the effects of the Laplace pressure (or matric suction) P_L , i.e.:

$$\sigma_s = (\sigma_n - u_a) \tan(\phi) + (u_w - u_a) \tan(\phi^b) + c , \quad (4.8)$$

where u_a and u_w are the pressures of the gaseous and liquid phase in the pores, respectively. ϕ^b indicates the rate of increase of the angle of internal friction with respect to the matric suction. Hence, to apply this model the matric suction needs to be measured.

4.3.2 Static friction

Most research focusses on the shear strength of granular soils, i.e., the static friction. For example, an extensive study on the shear strength as a function of the matric suction for unsaturated and saturated gold tailings has been done by Rassam & Williams (1999)⁵⁰⁻⁵².

Figure 4.7 shows the results of an experiment was performed by Fournier *et al.* (2005)¹²¹, who sheared granular matter in between deformable membranes by increasing the pressure on one side of the shear cell (inset). The pressure difference over the cell at which a deformation occurred was measured and calculated into a certain yield shear strength as a function of the water content of the sample.

4.3.3 Dynamic friction

The dynamic coefficient of friction μ_d may have behave differently with respect to the water content and displacement. Contrary to cohesion by cementation, in wet granular matter liquid bridges are formed and pinched off continuously during a shearing motion^{4;122}.

This can be especially interesting when short shocks (e.g., a seismic event) triggers the slow failure of a dam that is governed by the residual (dynamic) shear strength. The Aznalcóllar

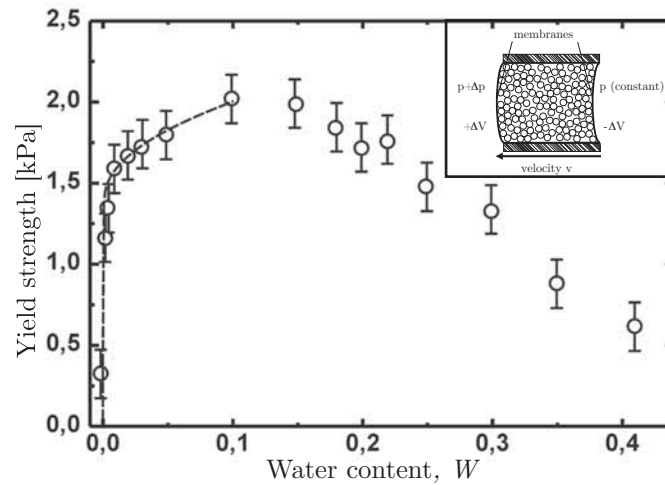


FIGURE 4.7: Yield strength versus water content of a sample of grains measured in a pressure driven shear apparatus (inset). [Modified after S. Herminghaus (2013)⁴, data and inset after Fournier *et al.* (2005)¹²¹]

tailings dam failure is an example of where such a slow failure mechanism may have occurred after the residual shear strength of the foundation was decreased^{91;92} (chapter 3).

Other phenomena that can influence the dynamic shearing of (wet) granular matter are:

- Water migration from the shear band¹²³,
- Dilatation of the shear band^{102;124;125},
- Particle size segregation during a granular flow^{102;111}, and
- Anisotropy in the distribution of the liquid bonds, which depends on the normal force applied^{46–49}.

Mani *et al.* (2012)¹²³ observed experimentally and numerically that a *migration of water* from the band occurs when an unsaturated material is sheared. This migration is associated with microscopic redistribution of liquid to neighboring contacts after a capillary bridges is ruptured due to the shearing motion.

Reynolds' dilatancy is the principle that a sheared volume of densely packed spheres expands, i.e. dilates, perpendicular to the shearing direction¹⁰². The principle is based on the concept that spheres, which are interlocked by their neighbours, are forced to move around each other. This forced displacement causes the grains to hop over one another, generating a net expansion and thus a reduced packing fraction.

During a granular flow, *particle size segregation* may occur. This is referred to as the Brazil nuts effect that occurs when shaking a granular material that consists of larger and smaller particles. This effect, which can be demonstrated with muesli, causes the larger grains to 'float' (i.e., move upwards) and thus results in a segregation. A more elaborate explanation of this phenomenon can be found in Herminghaus (2005)¹¹¹.

An anisotropy in the distribution of liquid bonds was found by Richefeu *et al.* (2006, 2008 & 2009)^{46–49}. This anisotropy was found to be dependent on the level and sign of the applied normal pressure.

Experiment

This chapter presents the experimental aspects of the research done, i.e., the created experimental setup in which granular material can be sheared dynamically.

While shearing a sample in this setup, the resulting friction consists of two components: *Grain-to-grain* and *grain-to-plate* friction. In order to measure these components two type of experiments were conducted:

Plate+grain The sample is sheared above the lower container and (partially) the plate.

Plate-only The sample is sheared above the supporting plate (no grain-to-grain friction).

By comparing the results of both experiments the shear stress between the grains can be obtained. This will be explained in the analysis of these experiments in chapter 6: Analysis & results.

This chapter is split into four part, each of which discusses one aspect of the experiments:

5.1: Shear box which consist of an upper container and a lower container recessed in a supporting plate.

5.2: Actuation of the upper container done by a linear induction motor via a rod.

5.3: Measurement of the force exerted on the upper container with a load cell.

5.4: Sample of glass beads with varying water contents that were sheared.

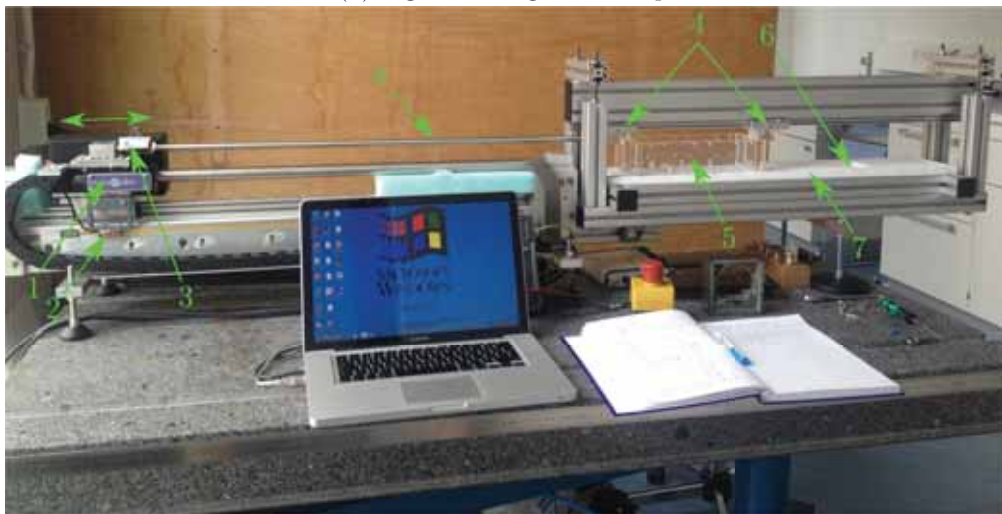
5.1 Shear box

Figure 5.1 shows both a digital drawing (A) and a photograph of the actual experimental setup (B). The upper container is fixed to a linear motor by a steel rod with a load cell mounted in between. The load cell measures the force exerted on the upper container while the linear motor shears a sample with a preprogrammed distance, velocity, acceleration and deceleration. The output of the load cell is recorded by a digital data acquisition module and saved on a computer for further analysis. Appendix B briefly describes the creation of this setup, which was build from scratch during this research.

A close up of shear box is shown in figure 5.2. Here the upper container is loaded for a plate-only measurement. The normal stress σ_n is generated by stainless steel plates on top of a PVC holder that tightly fits the upper container.



(A) Digital drawing of the setup.



(B) Photograph of the actual setup.

FIGURE 5.1: (A) Digital drawing and (B) photograph of the setup. 1. Linear motor, 2. Digital encoder, 3. Load cell, 4. Guiding rails, 5. Upper container, 6. Lower container, 7. Supporting plate, 8. Rod.



FIGURE 5.2: Close-up of the upper-container while it is loaded with a sample. The normal stress is applied by stainless steel plates that are on top of a holder (black PVC) that tightly fits the upper container.

The geometrical constants of the experiment, i.e., the dimensions of the setup, are given in table B.1 (Appendix B). From these dimensions the values of the areas of the upper, A_u , and lower container, A_l , were determined:

$$A_u = l_u \cdot w_u \approx 204 \text{ cm}^2 \quad (5.1a)$$

$$A_l = l_l \cdot w_l - 4 \cdot r_l^2 (1 - 1/4\pi) \approx 35.9 \text{ cm}^2 \quad (5.1b)$$

Hence, the ratio $A_u : A_l$ is $5^2/3 : 1$, i.e., during a plate+grain experiment only 17.7% of the total sheared surface is actually grain-to-grain.

Details on the shear box part of the setup, i.e., the supporting plate and the gap width (upper-container–plate) are described below.

5.1.1 Supporting plate

Although the friction of the supporting plates with the sheared granular material can be measured and accounted for during analysis, it is preferably kept minimal. There are two parameters controlling this friction:

1. the initial “dry” friction from the plate, i.e. surface roughness.
2. cohesion due to the formation of liquid bridges with the plate.

The “dry” friction of the plate can somewhat reduce over time as the plate wears out due to the experiment. It is expected that this effect will be marginal as long as the hardness of the material is adequately high and the normal forces used are small.

The cohesion or *suction* from liquid bridges in between the plate and the particles is larger than those formed in between the particles¹²⁶. The reason is that a liquid bridge with a plate has a smaller curvature, which reflects in a larger adhesion (see section 4.2). Hence, it is important that liquid bridges with the supporting plate do not, or scarcely, form. To inhibit this formation of liquid bridges, a hydrophobic supporting plate can be used. This hydrophobicity can be attained by either hydrophobic coatings or materials, e.g., silanised surfaces [octadecyltrichlorosilane (OTS)]^{115;127}.

In the experiments a Teflon [polytetrafluoroethylene (PTFE)] plate is used. Teflon has both a low coefficient of friction, $\mu = 0.04$ ^{70*}, and high hydrophobicity (contact angle smooth Teflon: 110–118°)¹²⁸.

5.1.2 Gap width

The minimum sample grain diameter that can be sheared in this setup is twice the achievable minimum distance between the upper-container and the supporting plate. Otherwise, the shear force on the particles at the edge can be deflected downward, which may mechanically jam part of the setup. This gap width is dependent on the flatness of the plate, parallelism of the plate and upper container, and tolerance in between the rail and the slider.

The tolerance in between the rail and the slider is adjustable: It can be completely tightened (zero tolerance), but this will result in high rail frictions (section 5.2.2). Therefore, a compromise was chosen with an estimated maximum tolerance of about 50 μm . An estimated maximum gap width of 300 μm was measured with thin metal strips. Summing both the gap width and rail tolerance (350 μm), particles of twice this size in diameter or larger are expected to be of adequate size for this setup, i.e., $\leq 700 \mu\text{m}$.

*The coefficient of friction is from the Handbook of Physics and Chemistry⁷⁰ and was determined by moving two plates over one another. The value presented is valid for Teflon on Teflon and Teflon on steel in dry conditions, under both the static and dynamic shearing condition, i.e., μ_s and μ_d , respectively.

5.2 Actuation

The linear motor used in the setup consists of a servo amplifier, a $5\ \mu\text{m}$ resolution digital ruler/encoder (Renishaw[®] RGH24D) and a magnetic rod with a block that can move over it (ThrustTube[®] TBX 2506). The rod (or stator) consist of permanent magnets that alternate in orientation. The block has coils which, by a driving current, can alternate their magnetic orientation, resulting in a monorail-like motion over the rod. Some key properties of this linear motor are the peak velocity of $9.7\ \text{m/s}$ and peak, intermittent and continuous stall forces of 929, 258 and $72.8\ \text{N}$, respectively¹²⁹.

5.2.1 Precision

The precision of both the position and velocity of the linear motor are limited by the response of the load it is moving. With an inelastic load it will be able to attain high precision, while an elastic load requires on-the-fly compensation by the controller. Unfortunately, the setup as shown in figure 5.1 induces an elastic response to the linear motor. This response originates from the rod, the difference in static and kinematic friction of the rails (i.e. stick-slip motion), and the load cell, which is essentially a spring.

When the motor compensates too much it can stall in a resonant type motion, in which it compensates the elasticity of the setup while recompensing any prior attempts. This vibration can be clearly detected by the load cell and potentially disturbs the measurement. To avoid this behaviour, the feedback frequency was adjusted downward which retards the motors compensation efforts. As a consequence, the motor may exhibit small oscillations in its velocity when completely unloaded. Higher loads inhibit the elastic response from the setup and result in a more constant velocity throughout the shearing motion.

5.2.2 Rail friction

Although the setup is designed to have a minimum friction, part of the measured shear force is introduced by the friction of the rails. Figure 5.3 shows this rail friction for various velocities, which was measured by simply pushing and pulling the upper container while it is empty.

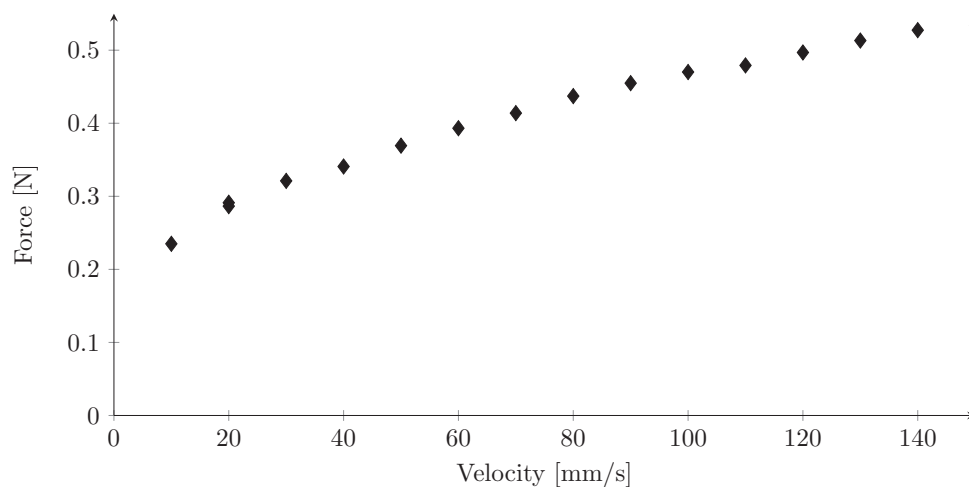


FIGURE 5.3: Measurement of the shear force of the (empty) setup for several velocities.

All measurements were done over an interval of 19 cm (plate-only) and 13 cm (plate+grain) at a velocity of 50 mm/s. At this velocity, the rail friction is approximately 0.37 N. As will be presented in chapter 6, this force measured with a non-empty setup is approximately 10 times higher than that introduced by the rail. Nonetheless, it is taken into account during the determination of the Coulomb cohesion.

5.3 Measurement

The load cell used is a so-called parallelogram load cell (FUTEK model LSM300, item FSH00006, figure 5.4). It has a measuring range of 222 N in both compression and tension in the z-direction, as defined in the figure 5.4¹³⁰. The rod can be attached to a thread in the middle beam, which will deform a strain gauge when pressed or pulled upon. It was calibrated in combination with a signal-conditioning amplifier module (FUTEK model CSG110, item QSH00602).

As the load cell is sensitive to noise generated by the linear motor and moments in the xy-plane induced by the object moving through the suspension, a detailed description of the calibration and measures taken to reduce and quantify these unwanted effects are given below.



FIGURE 5.4: Load cell used in the experiments.

5.3.1 Noise reduction

Little noise on the output signal of the load with a frequency of 50 Hz is visible when no additional equipment is switched on. This causes a small modulation on the signal, which can be attributed to the 50 Hz AC mains power supply.

A larger and significant amount of noise is imposed on the output of the load cell when the linear motor is switched on. This noise was attributed to two different artefacts:

1. High frequent noise ($\sim 10^3$ Hz) originating from the servo amplifier that was picked up by the signal conditioner, coaxial cables, and metal parts of the setup.
2. A ground loop between the linear motor and the power source.

The high frequent noise was largely resolved by shielding the signal conditioner with a metal box acting as a Faraday cage, grounding the wires and setup, and placing a low-pass filter into the circuit (figure 5.5). The ground loop was eliminated by connecting the motor control and measuring devices to separate groups.

Another noise was identified to be the laboratory DC power source used for the experiments on dry glass beads. Significant deviations in the source's voltage, were also visible in the

output of the load cell. Hence, a 12 V (motorcycle) battery was placed in the setup to give a more reliable DC source. Finally, the setup was placed on an heavy granite table to reduce any mechanical vibrations and thus noise on the signal.

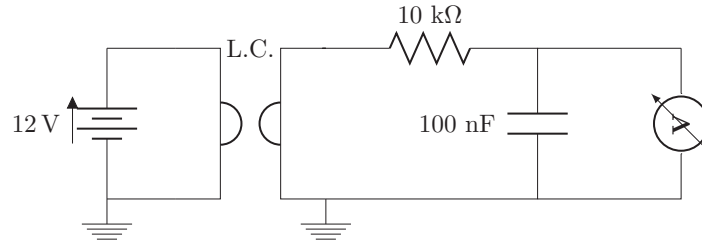


FIGURE 5.5: Electronic circuit with the low-pass filter connected to the load cell (L.C.). The cut-off frequency is 159 Hz ($f_c = \frac{1}{2\pi RC}$)

5.3.2 Calibration

Since the load cell is mounted within a small distance of the linear motor possible errors on the outcome of the calibration, i.e. the force–voltage ratio, can arise. For example:

1. The noise of the linear motor as previously described, and
2. Rigidity introduced by the permanent magnets of the linear motor.

The noise is found to lower the measured output voltage of the load cell, which will not introduce a problem when the force–voltage ratio remains linear and (preferably) equal. The force generated by the permanent magnets may inhibit deflection of the load cells middle beam, making the sensor less sensitive. In order to verify the (in)significance of these effects, the load cell was calibrated twice; outside the setup with the motor switched off, and mounted in the setup with the motor switched on. This was done by hanging calibrated weights to the middle beam of the load cell by a string.

Both calibrations are plotted and fitted in figure 5.6. A small deviation of about 0.274 N/V in the output of the load cell was observed, which is a relative error of only 0.6%. Considering that the calibration outside the setup consists of more data points over a wider range, it is used to calculate the forces reported in this Thesis, i.e.:

$$F = (45.646 \pm 0.274) \cdot (V - V_0) . \quad (5.2)$$

Strain response

Besides the force in the z-direction, the load cell may also experience forces in the xy-plane when the rod slightly bends. To get an order of magnitude of these fluctuations, the end of the rod was subjected to forces in the horizontal plane, by the use of a pulley, string and calibrated weights. A digital tension gauge was placed in between the rope and the rod, to verify the tension on the string. As a results, a maximum force discrepancy of ± 0.05 N was measured. Since both ends of the rod are attached to the setup, it is unlikely that the load cell will experience strain during the experiments.

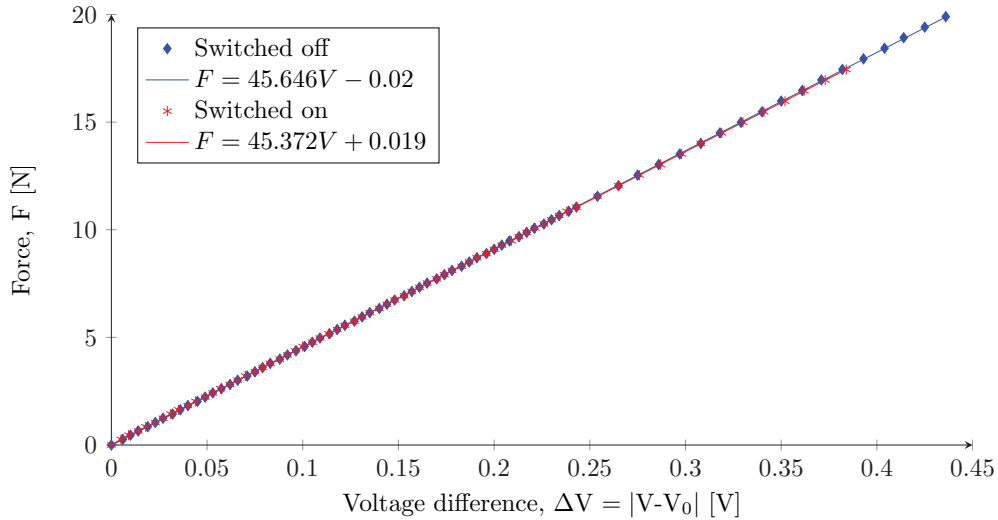


FIGURE 5.6: Calibration of the load cell with the linear motor switched on (*) and switched off (♦). The coloured lines are the corresponding linear fits.

5.3.3 Data acquisition

The output voltage is measured by both a voltmeter and digital data acquisition module (National Instruments USB-4432) that is connected to a computer with National Instruments' LabVIEW SignalExpress installed on it. The voltmeter acts as a guide to the eye during the experiment, while the data acquisition module records the signal with 5 kHz.

5.4 Sample

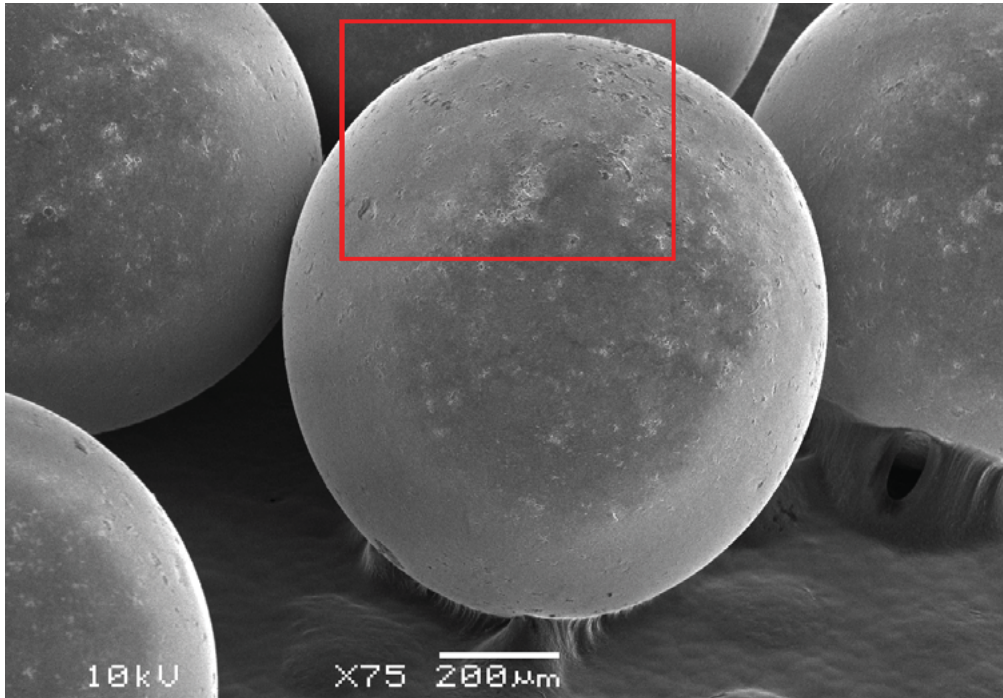
For the granular phase, spherical beads from soda lime glass were used in all experiments (density $\rho_s = 2490 \text{ kg m}^{-3}$). Glass beads are often used as a controllable and reproducible sample that can be regarded as an ideal sand.

Contrary to natural soils, the effects from the particle shape and polydispersity are absent in this type of granular material. In nature, soils are often found to have angular shaped grains and large particle size distribution. These characteristics will give rise to higher grain-to-grain friction and packing fraction as compared to the spherical glass beads⁴.

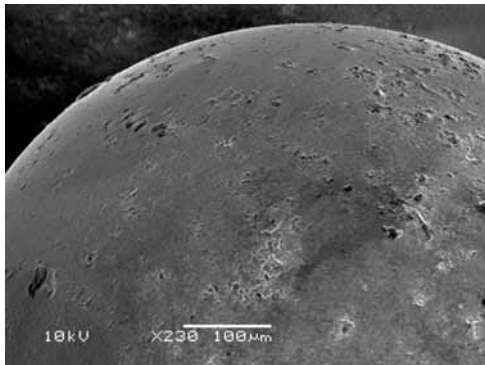
Beads of 1 mm in diameter, with a variation of approximately 10 %, were used. These beads are larger than the grain size of tailings material used for the dams [100–300 μm (figure 3.9)], which is the scope of this research. This deviation lies in the achievable minimum distance between the upper-container and the supporting plate (section 5.1.2)

Roughly similar characteristics are expected for particles of 100–300 μm diameter. The relevant energies that play a role at both scales are roughly the same (figure 4.4), i.e., in both cases capillary forces are dominant. Yet, gravity becomes more significant as it approaches the capillary length $\kappa^{-1} = 2.7 \text{ mm}$ of the system (equation 4.4). Gravity, may break or inhibit the formation liquid bridges, and is the driving force behind drainage. The inertial (kinetic) forces are not expected to play a significant role as experiments were done at velocities in the order of 1 cm/s (figure 5.3).

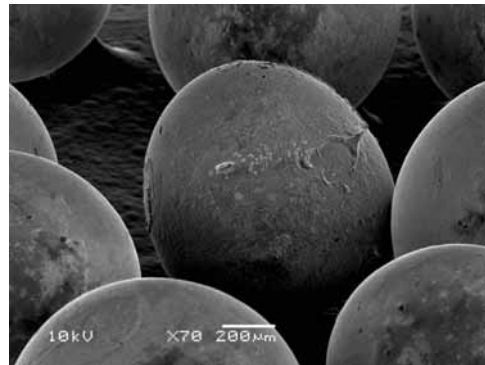
Scanning Electron Microscope images of both used (sheared in experiments) and unused (newly bought) beads are presented in figure 5.7. Both used and unused samples show many asperities and cavities, i.e., surface roughness. Surface roughness will affect both the angle of internal friction^{66;131} and the water content beyond which capillary bridges are formed, i.e., W_{cb} (figure 4.5)⁴. Some of the used grains show larger damages that may be the result of the experiment [right hand side of the grain in figure 5.7(c)]. Yet, due to the rare occurrence of these damages and relatively weak alteration it invokes, it is not expected that results will be affected when a sample is used for multiple experiments.



(A) SEM image of unused glass beads attached to carbon tape. The red square indicates the close up area of figure 5.7(b).



(B) Close up SEM image of the surface of an unused glass bead, showing asperities and cavities.



(C) SEM image of used, i.e., sheared, glass beads.

FIGURE 5.7: Scanning Electron Microscope imagery of (A) & (B) unused and (C) used 1 mm glass beads. [In collaboration with R. Groenen]

5.4.1 Packing fraction

In the setup used during these experiments a random close packing can be achieved by shaking the sand after it is poured in the setup (section 4.1). In an ideal situation, where grain-to-grain friction and elasticity are both negligible, a packing fraction of approximately 0.64 could be achieved. In practice, the glass beads do experience a mutual coefficient of friction in the order of 10^{-1} [†]. Herminghaus (2013)⁴ determined $\phi \approx 0.62$ to be more applicable when considering similar values for the aforementioned coefficients of friction. In this state the average number of neighbouring spheres or *coordination number*, is approximately 6. This packing is referred to as a *random dense packing* (ϕ_{rdp}) and is assumed to be the packing fraction prior to shearing in this thesis.

5.4.2 Liquid content

The liquid content W and degree of saturation S are described in section 4.1.2. Assuming $\phi = \phi_{\text{rdp}} = 0.62$, we find for W and S from equations 4.1 and 4.2, respectively:

$$W = \frac{m_l \rho_s \phi_{\text{rdp}}}{m_s \rho_l}, \quad (5.3)$$

$$S = \frac{m_l \rho_s \phi_{\text{rdp}}}{m_s \rho_l (1 - \phi_{\text{rdp}})}, \quad (5.4)$$

where in this case $\rho_s = 2493 \text{ kg/m}^3$ and $\rho_l = 1000 \text{ kg/m}^3$ (water).

Table 5.1 gives the water contents and degrees of saturation of the samples used. The mass of the glass beads m_s for plate-only experiments was 1000 g, but to remain comparability 1138.6 g of grains were used during plate+grain experiments. This 138.6 g extra grains is calculated to fill the lower container[‡]. Hence, the same sample weight is above the sheared surface during both type of experiments.

Prior to adding water, the samples were dried in an oven (105 °C) for at least 12 hours to evaporate any water added by humidity or previous experiments and allowed to cool down to room temperature.

TABLE 5.1: Liquid content of the samples used. The liquid content W and saturation S are given in equations 4.1 and 4.2, respectively. The different wetting regimes to which W theoretically relates is shown in figure 4.5.

| Liquid content W | Saturation S [%] | Wetting regime ⁴ | Liquid volume V_l [ml] | |
|--------------------|--------------------|-----------------------------|--------------------------|-------------|
| | | | Plate-only | Plate+grain |
| 0 | 0 | dry | 0 | 0 |
| 0.026 | 6.8 | pendular | 16.8 | 19.1 |
| 0.053 | 13.95 | funicular (clusters) | 34.3 | 39.1 |
| 0.1 | 26.3 | funicular (bicont.) | 64.8 | 73.8 |
| 0.15 | 39.5 | funicular (bicont.) | 97.2 | 110.6 |
| 0.2 | 52.6 | funicular (bicont.) | 129.6 | 147.5 |
| 0.3 | 79.0 | bubbles | 194.3 | 221.23 |

[†]Glass to glass plates are found to have coefficients of friction of $\mu_s = 0.94$, and $\mu_k = 0.4$ (equation 4.5) (after the Handbook of Chemistry and Physics⁷⁰).

[‡]Mass in lower container $m_l = V_l \cdot \rho_s \phi_{\text{rdp}} = A_l \cdot h_l \cdot 2.49 \cdot 0.62 \approx 138.6 \text{ g}$, where V_l, A_l , and h_l are the volume, area, and height of the lower container (table B.1 and equation 5.1b).

Analysis & Results

This chapter presents the results from the experiments of which the setup was described in the previous chapter. Section 6.1 gives the analysis of the raw signal into meaningful quantities like forces and stresses/pressures. Section 6.2.1 presents the results from the two types experiments done for dry glass beads and at six different water contents. During the first type, the sample is sheared with the teflon plate only (referred to as plate-only or σ_p -experiments). Resulting in a measurement of the grain-to-plate friction force F_p or shear stress σ_p .

During the second type of experiment, the sample was sheared above the lower container containing grains with an equal water content, i.e. from the same sample (referred to as plate+grain or σ_{p+g} -experiments). This results in the measurement of the force F_{p+g} (shear stress σ_{p+g}), which comprises both the grain-to-plate friction (F_p) and grain-to-grain friction force (F_g).

Finally, section 6.2.2 gives the grain-to-grain shear stress σ_g deduced from both type of experiments and fits these to a Mohr-Coulomb model.

6.1 Analysis

6.1.1 Noise filtering

A typical output signal of the strain gauge sensor, while shearing the sample above the lower container, is shown in figure 6.1. The analysis of the output signal was done by the use of a Matlab script, which is presented in appendix C.

The light grey (noisy) curve is the original measured signal, i.e., the output of the load cell. As the original signal contains a significant amount of high-frequency noise, the signal is digitally filtered (zero-phase) with a Butterworth low-pass filter with a cut-off frequency of 5 Hz. This 5 Hz filtered signal is indicated as the black line in figure 6.1 and was used for further analysis.

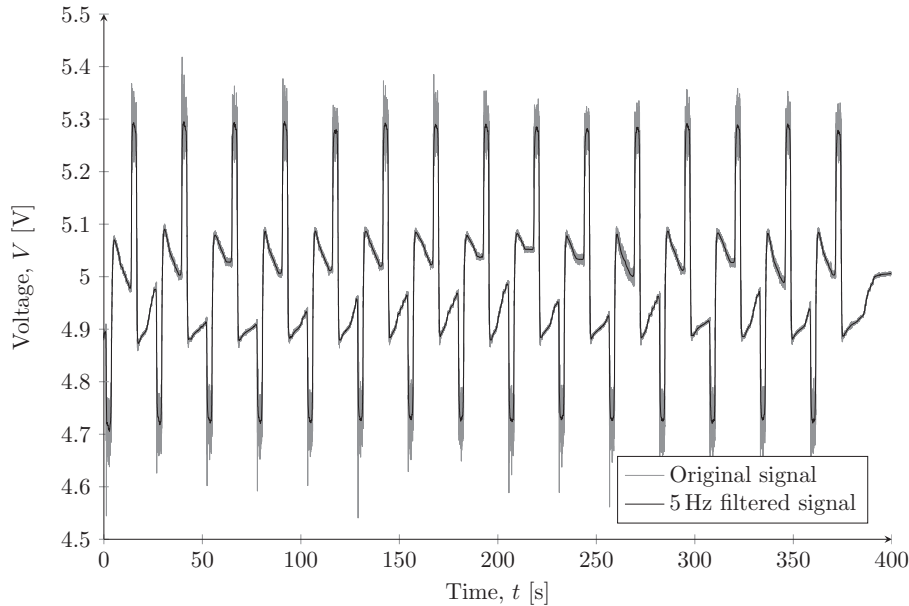


FIGURE 6.1: Example of the measured (grey) and its filtered signal (black) while shearing a sample ($W = 0.3$) 15 times back and forth while applying a normal pressure of $\sigma_n \approx 1559$ Pa. $V < 5$ V indicates a force in the negative direction (pushing) and $V > 5$ V in the positive direction (pulling).

6.1.2 Timing

Next to the output of the load cell, a trigger signal from the linear motor was measured. This trigger signal gave $V_{trig} = 5$ V when the linear motor was moving, while indicating $V_{trig} = 0$ V when it is idle. To get rid of measuring artifacts of V_{trig} , the original trigger signal was converted to a binary signal which is 1 when $V_{trig} \geq 3$ V and 0 otherwise. This binary trigger signal (with an offset of 4.5 V) is shown in the detailed view figure 6.2 and was used to determine the intervals of motion.

6.1.3 Baseline

The signal condition module from the load cell (section 5.3) ought to give a 5 V signal when the linear motor idles and, hence, no force is applied. Yet, it can be observed in figure 6.2 that the values in between the shearing motion are not constant. Even prior to the measurements the signal indicates a small force in the negative direction (push).

This behaviour was observed for both type of measurements and for all samples (with or without adding liquid), but not when the shear box was empty (figure 5.3). Hence, it is an artifact originating from the sample in the shear box.

A possible explanation of this behaviour can be found in the formation of an ensemble of force networks during shear motion¹³². These force networks oppose the shear force and cause an overshoot when shearing is halted. After this overshoot, these force networks start to relax with a certain (logarithmic) rate. Hartley & Behringer (2003)⁵⁷ found a first fast relaxation occurring within a timescale in the order of 20–300 s after which a slower relaxation continues for several hours (over 20 hrs). As a consequence of this slow process, it is hard to determine a proper baseline for a signal like that in figure 6.1, i.e., where the measured voltage corresponds to force $F(t) = 0$.

This baseline can be measured prior to the measurements, but a large disadvantage is that the source's voltage may drop slightly over time (battery). Another way to determine this baseline is by assuming that there is no difference between shearing the sample in negative (pulling) or positive direction (pushing), i.e., both should comprise the same result. Under this assumption, the average values of all averages per motion (red lines in figure 6.2) should be equal to the baseline. This baseline is indicated by the blue line in figure 6.2. This value (here 5.0033 V) was subtracted from the filtered signal to obtain absolute voltage differences, which after conversion with the calibration constants (equation 5.2), correspond to a absolute forces deviation from zero.

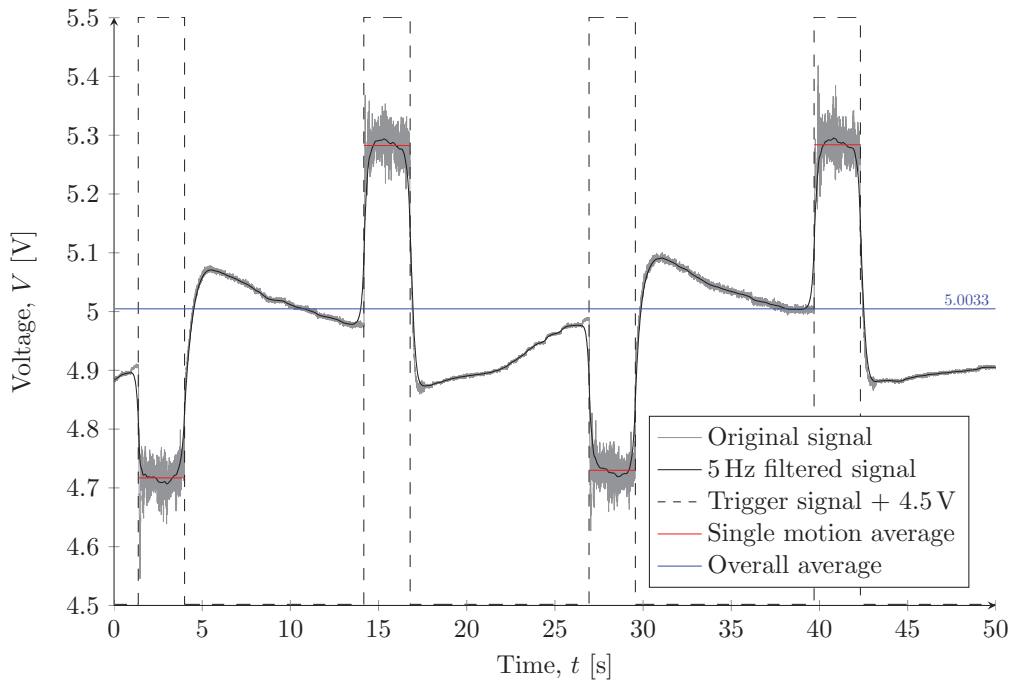


FIGURE 6.2: Detailed view of the first four shear measurements as shown in figure 6.1. Besides the original (grey) and filtered signal (black), the trigger signal (with an offset of 4.5 V) (dashed) is given. Also, the averages per motion (red) and overall average (blue) are indicated.

6.1.4 Average determination

Now the baseline has been determined, the (filtered) signal can be converted into units of force by the use of the calibration constants determined (equation 5.2). From these values the average forces measured during a shearing motion (pushing or pulling) can be determined*.

Figure 6.3 shows an even view at a single (pulling) motion. The average force exerted on the load cell during such a motion were determined by taking the mean value over the interval, disregarding the first and last one fourth of a second. Within this disregarded time, the linear motor is still accelerating or decelerating, respectively. Also, Gan *et al.* (1988)⁵⁴ and Nam *et al.* (2011)⁵⁵ typically found a start-up phase in the first millimeters of displacement during a multi-stage direct shear test.

*Note that on average the forces for pushing and pulling motions will be equal, as these were used to determine the baseline.

The mean value was calculated for each push and pull motion (red line), from which (again) the average was taken to determine a single value for the shear force F_s at a specific normal force, F_n .

This mean value does not yet indicate dynamic behaviour during the motion. Hence, in order to get a better view of the development of the signal, each motion was split in four equal time intervals as shown in figure 6.3. Again, the mean value of the averages per interval was determined to get a global view of the dynamical behaviour during the motion.

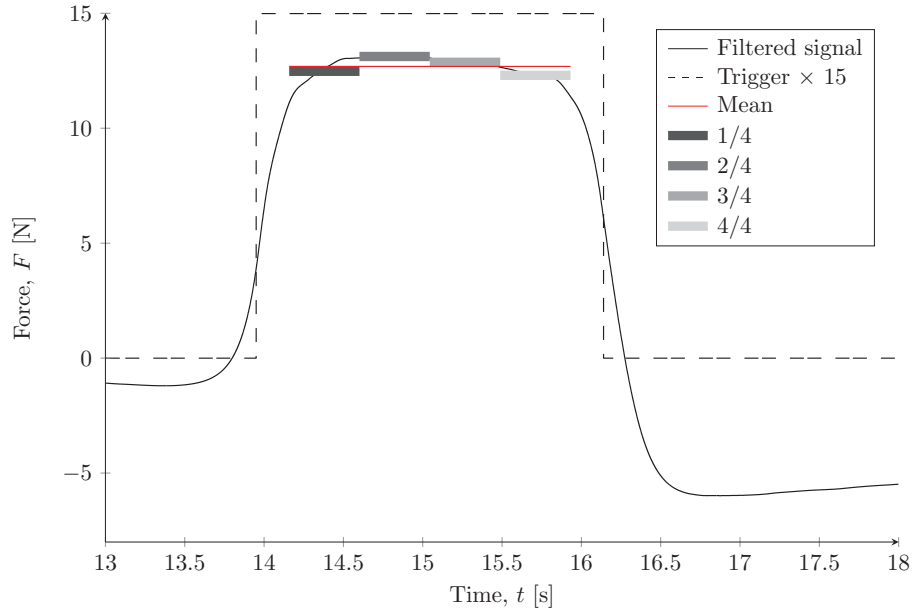


FIGURE 6.3: Detailed view of the first pulling motion as shown in figures 6.1 and 6.2. The four average intervals that were measured to visualise deviations in time are indicated alongside the total average for that motion (red). The filtered signal is given by the solid line and the trigger signal multiplied by 15 by the dashed line.

In order to create order in the chaos of averages, this list below describes the various averages that are taken from each measurement, consisting of 30 motions (15 pushes, 15 pulls):

- Average per motion
 - **Baseline:** Average of all 30 averages per motion (e.g., figure 6.2)
 - **Mean value:** Average of all 15 averages per push/pull. Presented in section 6.2.
- Average per interval per motion, i.e., first 1/4, second 2/4, third 3/4, and fourth 4/4 interval (e.g., figure 6.3).
 - Average of the 15 averages per interval per push/pull. Presented in section 6.2.

6.1.5 Calculation of shear stresses

With the previous steps, the shear force F_s exerted on the sample (with water content W) under a certain normal force F_n is known. These forces can be converted to stresses, which allows the measurement to be compared to models (e.g., Mohr-Coulomb) and values found in literature.

Figure 6.4 shows a schematic topview of the shearbox, indicating the area of the upper- and lower-container, i.e., A_u and A_l , respectively.

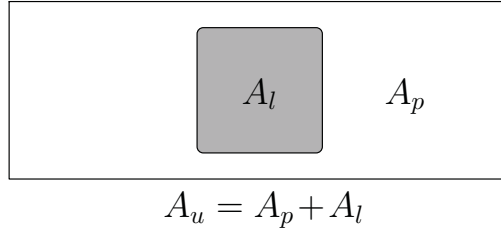


FIGURE 6.4: Schematic topview of the upper container with area A_u on top of the lower container with area A_l . A distinction is made between the area where grain-to-grain friction and grain-to-plate friction acts, i.e., A_l and A_p , resp.

Normal pressure σ_n

The normal force F_n acting on the shear band has two contributors:

1. The added weight m_{add} (including the PVC holder).
2. The weight of the sample, i.e., grains m_g and added liquid m_l (if applicable).

Hence, the normal force $F_n = (m_{add} + m_g + m_l) \cdot g$, where g is the standard gravity acceleration on Earth ($g \approx 9.81 \text{ ms}^{-2}$)^{133†}. As a consequence, measurements cannot be done at normal forces/stresses lower than those generated by the mass of the sample.

The normal pressure σ_n can be calculated by simply dividing the normal force by the area of the shearing interface, i.e., A_u :

$$\sigma_n = \frac{F_n}{A_u} = \frac{(m_{add} + m_g + m_l) \cdot g}{A_u} \quad (6.1)$$

Shear stresses σ_p , σ_{p+g} and σ_g

Similar to the normal force, the shear force F_s measured by the load cell, σ_p (above plate) and σ_{p+g} (above lower container) can be easily calculated by dividing the measured force by the area of the upper container A_u , i.e.:

$$\sigma_p = \frac{F_p}{A_u} \quad (6.2)$$

$$\sigma_{p+g} = \frac{F_{p+g}}{A_u} \quad (6.3)$$

To determine the shear stress resulting from the grain-grain interface, i.e., σ_g , both type of experiments need to be considered. σ_{p+g} comprises both the shear stress resulting from grain-to-plate (σ_p) and grain-to-grain (σ_g) friction shear stress. By subtracting σ_p from σ_{p+g} the contribution of the grains can be determined. This can be done by splitting F_{p+g} up in the contributions of the shear stress of the plate $F_p = A_p \sigma_p$ and the grains $F_g = A_l \sigma_{p+g}$ (figure 6.4), i.e.:

$$F_{p+g} = (A_u - A_l) \sigma_p + A_l \sigma_g \quad (6.4)$$

Now by substitution of equation 6.3 and rewriting in terms of σ_g , yields:

$$\sigma_g = \frac{A_u}{A_l} \sigma_{p+g} - \frac{A_u - A_l}{A_l} \sigma_p = \frac{A_u}{A_l} (\sigma_{p+g} - \sigma_p) + \sigma_p \quad (6.5)$$

Hence, from the measured force in both type of experiments the shear stress resulting from the grain-grain fraction can be calculated by equation 6.5.

[†]This value is assumed to be valid for Enschede, The Netherlands. Measurements done by the Netherlands Geodetic Commission from 1991 to 1999 show deviation in the order of 10^{-3} throughout the Netherlands

6.2 Results

6.2.1 σ_p - and σ_{p+g} -experiments

Figure 6.5 shows typical shear stress σ_s versus normal pressure σ_n plots of the plate-only [σ_p (*)] and plate+grain [σ_{p+g} (*)] experiments done for various water contents W (table 5.1). Each of these points represents the average of 15 shearing motions (pushes or pulls) by the linear motor at a certain normal pressure.

The minimal normal pressure achievable in the setup was when no mass was added on top of the sample, i.e., the sample was free to move. Hence, the only mass applying a force on the shearing interface is that of the sample itself, i.e., 1000 - 1194 g (table 5.1). During these (low σ_n) experiments, the whole shearing surface remained covered with grains, although the back and forth movements of the material caused a pile to form.

Figure 6.5(a) shows that σ_p and σ_{p+g} are quite similar for dry material, indicating a small contribution of the grain-to-grain friction to the total measured shear stress. This is not out of the ordinary as only 17.7% of the total sheared surface is actually grain-to-grain.

Adding a bit of water already shows a large change in-between σ_p and σ_{p+g} . This can be clearly seen for $W = 0.1$, where the both shear stresses are wider spread [figure 6.5(b)]. In this particular example, something changes for the σ_{p+g} -measurements at normal pressures larger than 1270 Pa. Increasing the water content even further, yields a decrease in the difference between the σ_{p+g} and σ_p [figure 6.5(c)].

Time development

The (average) time development during the shearing motions is also visualised in figure 6.5 by the lines with different shades of grey [from dark (start) to light (end)]. The plate-only measurements (*) show a reverse in behaviour from water contents of 0.15 onward. Below $W = 0.15$, the measured plate-only shear stress decreases with respect to time (and hence displacement), while above this value it increases. A possible explanation may be found in the imperfect hydrophobicity of the Teflon plate. Although Teflon is hydrophobic, a thin water film could be developed for higher water contents, i.e., water may (partially) drain in between experiments. Upon shearing, this water is taken back into the sample forming liquid bridges and removing the lubrication layer on the teflon plate, i.e., the shear stress increases.

For the plate+grain measurements (*), no specific trend in time with respect to water content is observed. In general, the shear stress increases at first with respect to time/displacement after which it stabilises (figure 6.3). Yet, it is remarkable that in figure 6.5(b), this increase with respect to time for the σ_{p+g} -measurements is more pronounced for higher normal pressures. A possible explanation behind the deviation of these experiments is given in the discussion of the next chapter.

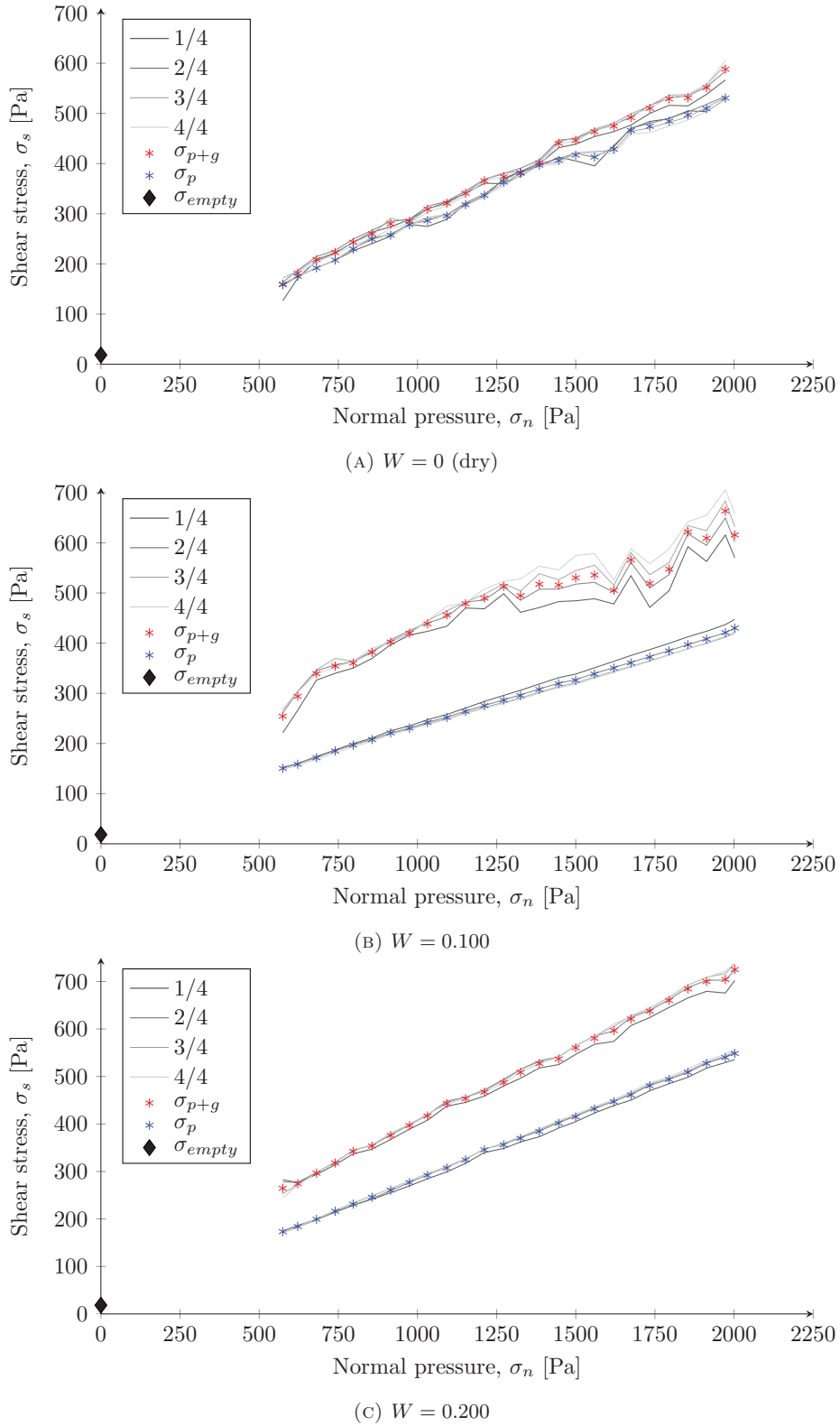


FIGURE 6.5: Shear stress σ_s versus normal pressure σ_n for $W = 0$ (dry), $W = 0.1$, and $W = 0.2$. The σ_p -experiments are indicated by blue asterisks (*) and the σ_{p+g} -experiments by red asterisks (*). The four intervals, as shown in figure 6.3, are also represented as shades of grey [from dark (start) to light gray (end)]. The measured shear stress equivalent from the rail friction of the apparatus is indicated by the black diamond (\blacklozenge) ($\sigma_{empty} \approx 18.4$ at 50 mm/s, see figure 5.3).

6.2.2 Grain-to-grain shear stress (σ_g)

Now that σ_p and σ_{p+g} are experimentally determined, σ_g can be calculated by equation 6.5. The resulting shear stress versus normal pressure plots for dry material, $W = 0.1$, and $W = 0.2$ are presented in figure 6.6 alongside their respective linear regression fits. These values are calculated point-by-point, i.e., for each normal pressure σ_n .

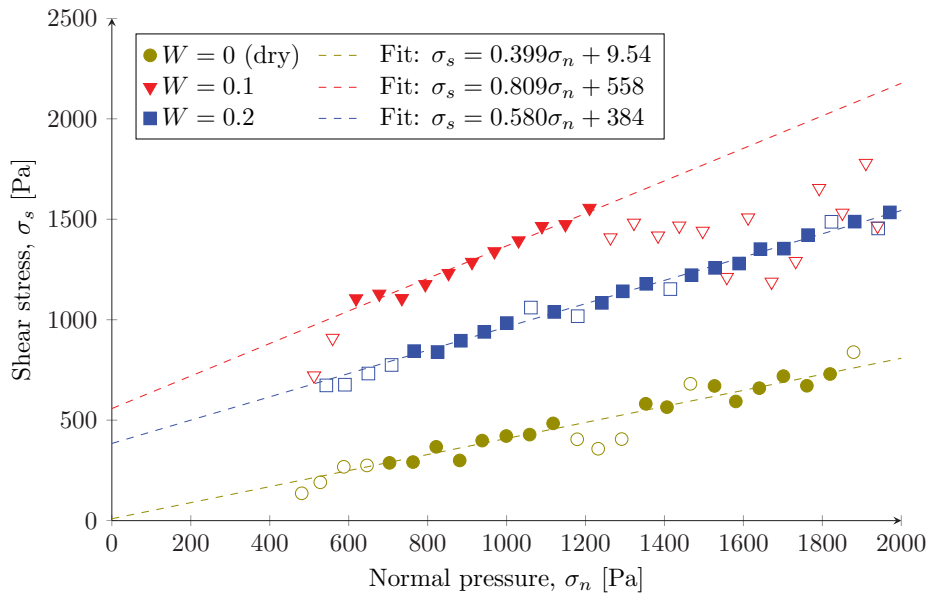


FIGURE 6.6: σ_g calculated for $W = 0$ (●), $W = 0.1$ (▼), and $W = 0.2$ (■). The determined outliers, that are excluded from the linear regression, are indicated by the open symbols. (See table 6.7 for correlation error, fit values, and the Mohr-Coulomb criteria for different water contents)

The data presented in figures 6.5 and 6.6 can be fitted to the Mohr-Coulomb theory[‡] (section 4.3), i.e., $\sigma_s = \sigma_n \tan(\phi) + c$. This was done by linear regression of the experimental data excluding outliers. Outliers that show clear deviation from linearity were either manually or automatically selected. Manually selected outlier consists of visually unreliable data. For example the σ_{p+g} -measurements for figure 6.5(b) clearly shows a clear deviation from linearity for normal pressures larger than 1270 Pa.

The automatically selected outliers consist of the first few (up to four) data points. These values show a (slightly) different slope that may be due to heap formation as the sample is moved hence and forth (section 6.2.1)]. After exclusion of these selected outliers, a preliminary linear fit is made and the residuals per point are calculated. Subsequently, any points that have residuals larger than the root-mean-square error (RMSE)[§] are also indicated as an outlier and excluded from the final fit.

[‡]For an unsaturated granular material, the pore pressure $u = 0$, i.e., $\sigma'_n = \sigma_n$.

[§]The RMSE is the standard deviation of the residuals.

6.2.3 Mohr-Coulomb

The data from the experiments and calculated values for σ_g were also fitted to the Mohr-Coulomb failure criterion (equation 4.8). Table 6.1 and figure 6.7 present the values of the angle of internal friction $\phi = \tan^{-1}(\mu)$ [figure 6.7(a)] and cohesion (c) [figure 6.7(b)]. It needs to be emphasised that ϕ and c from the experimental data (i.e., σ_p and σ_{p+g}) (partially) represent the friction between the glass beads and the Teflon plate. Hence, they do not represent an intrinsic value of the granular material.

Angle of internal friction ϕ

The angle of internal friction, does show a trend: In the lower wetting regime, the friction increases (up to $W = 0.053$) after which it either:

- Steadily decreases while the sample becomes saturated, or
- Stabilises around a value of approximately 35° .

Yet, taking into account the low angle of repose saturated granular materials can sustain (e.g., figure 4.2), it is unlikely that the angle of internal friction will continue to be significantly higher than that of the dry material.

In this perspective, the relation between the angle of internal friction and the water content seems to follow a similar trend as that for the yield strength as a function of the water content measured by Fournier *et al.* (2005)¹²¹ (figure 4.7).

Only the largest water content $W = 0.3$ shows a deviation from this trend. This outlier may be the result of drainage into the lower container as this may affect two aspects: The saturation of the lower container (reducing the water content of the upper container) and lubrication of the plate. As a consequence, the friction with the plate will be lowered as the plate is lubricated, while σ_g increases as the water content is actually lower than expected (due to drainage to the lower container).

Cohesion c

The cohesion values show large uncertainties. In fact, the value for σ_g at $W = 0.053$ gives an unphysical, negative cohesion, i.e., particles repel each other. Yet, within the 95% confidence bounds, the cohesion seems to be approximately zero for water contents $W \leq 0.053$. This is not in line with the cohesion in static shear strength experiments conducted on glass beads by Richefeu *et al.* (2006, 2008 & 2009)⁴⁶⁻⁴⁹, where a clear increase was observed for low water contents ($W \leq 0.05$). Also, Rassam & Williams (1999)⁵⁰⁻⁵², who did static shear strength experiments on tailings material with varying water content, find an increase in the cohesion and only a small deviation in the angle of internal friction.

Disregarding the negative value in the lower wetting regimes, the cohesion exhibits a peak value of approximately 550 Pa at $W = 0.1$, just after the peak value of ϕ at $W = 0.053$. After this maximum, the cohesion seems to decrease with respect to the water content. Yet, a distinct trend in the cohesion is hard to determine as the values show large uncertainties (see table 6.1).

It needs to be borne in mind that the values for cohesion are obtained from an extrapolation. As there are no measurable values for normal forces closer to zero, the slightest deviation in the friction angle will result in a large uncertainty in the cohesion. Also, errors in both experiments will sum up to that in σ_g . After equation 6.5:

$$\delta(\sigma_g) \approx \left| \frac{A_u}{A_l} \right| \delta(\sigma_{p+g}) + \left| \frac{A_u - A_l}{A_l} \right| \delta(\sigma_p) . \quad (6.6)$$

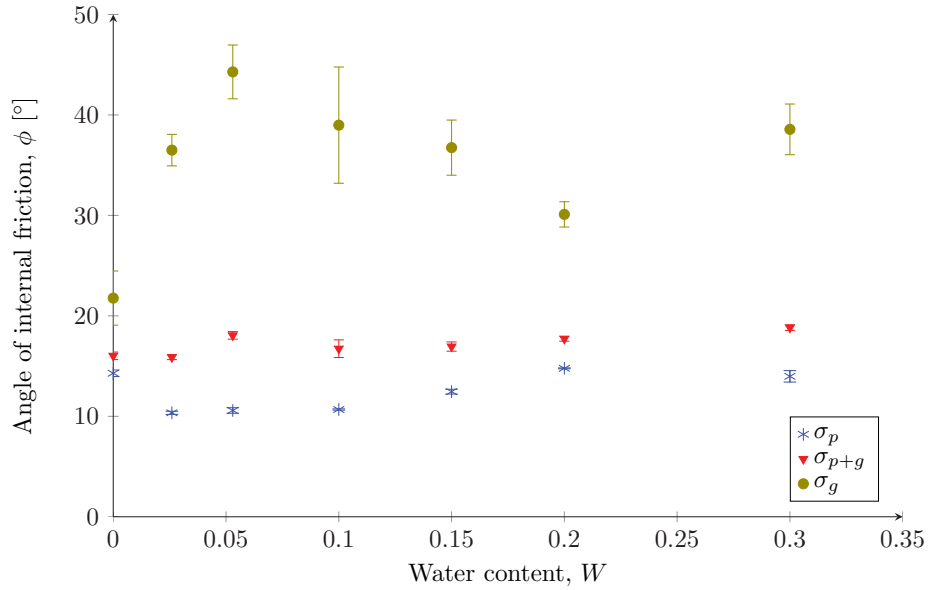
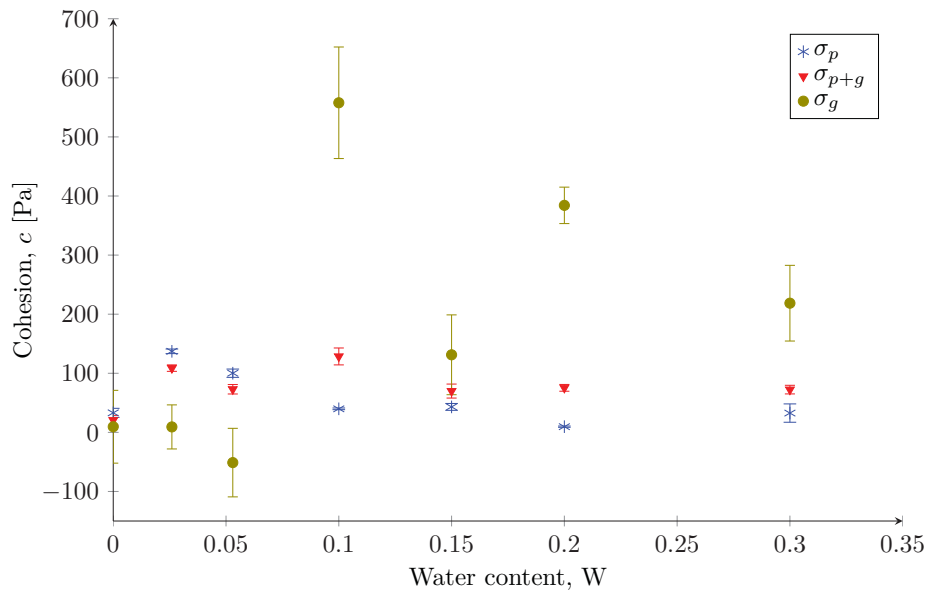
(A) Angle of internal friction, ϕ , as a function of the water content, W .(B) Cohesion, c , as a function of the water content, W .

FIGURE 6.7: Mohr-Coulomb criteria: (A) Angle of internal friction (ϕ) and (B) cohesion (c) as a function of the water content (W) for both experiments (Plate-grain: σ_p ; Plate+grain: σ_{p+g}) and calculated grain-to-grain shear stresses (σ_g). See table 6.1.

TABLE 6.1: The coefficient of friction (μ), angle of internal friction (ϕ) and cohesion (c) of the experimental data (σ_p & σ_{p+g}), and calculated σ_g for various water contents W . Also, their respective errors, $\delta(\mu)$, $\delta(\phi)$, and $\delta(c)$ (absolute, 95 % confidence interval) and the coefficient of determination, R^2 , of the fits used to obtain these parameters are given.

| Plate-only (σ_p) experiments | | | | | | | |
|---------------------------------------|--------|---------------|------------|--------------------|----------|------------------|-------|
| W | μ | $\delta(\mu)$ | ϕ [°] | $\delta(\phi)$ [°] | c [Pa] | $\delta(c)$ [Pa] | R^2 |
| 0.000 | 0.2546 | 0.006 | 14.3 | 0.3 | 33.1 | 7.6 | 0.999 |
| 0.026 | 0.1826 | 0.003 | 10.3 | 0.2 | 137.2 | 3.9 | 0.999 |
| 0.053 | 0.1868 | 0.005 | 10.6 | 0.3 | 100.1 | 7.0 | 0.998 |
| 0.100 | 0.1885 | 0.001 | 10.7 | 0.1 | 39.9 | 1.4 | 1.000 |
| 0.150 | 0.2209 | 0.004 | 12.5 | 0.2 | 43.1 | 5.8 | 0.999 |
| 0.200 | 0.2637 | 0.001 | 14.8 | 0.0 | 9.7 | 1.1 | 1.000 |
| 0.300 | 0.2489 | 0.010 | 14.0 | 0.6 | 32.7 | 15.5 | 0.996 |

| plate+grain (σ_{p+g}) experiments | | | | | | | |
|--|--------|---------------|------------|--------------------|----------|------------------|-------|
| W | μ | $\delta(\mu)$ | ϕ [°] | $\delta(\phi)$ [°] | c [Pa] | $\delta(c)$ [Pa] | R^2 |
| 0.000 | 0.2872 | 0.007 | 16.0 | 0.4 | 20.7 | 8.0 | 0.999 |
| 0.026 | 0.2846 | 0.004 | 15.9 | 0.2 | 108.7 | 5.5 | 0.999 |
| 0.053 | 0.3260 | 0.007 | 18.1 | 0.4 | 73.0 | 8.0 | 0.999 |
| 0.100 | 0.3006 | 0.015 | 16.7 | 0.9 | 128.5 | 14.3 | 0.995 |
| 0.150 | 0.3046 | 0.008 | 16.9 | 0.5 | 69.9 | 11.8 | 0.998 |
| 0.200 | 0.3195 | 0.004 | 17.7 | 0.2 | 75.4 | 5.7 | 0.999 |
| 0.300 | 0.3410 | 0.005 | 18.8 | 0.3 | 72.4 | 7.3 | 0.999 |

| Grain-to-grain shear stress (σ_g) calculations | | | | | | | |
|---|-------|---------------|------------|--------------------|----------|------------------|-------|
| W | μ | $\delta(\mu)$ | ϕ [°] | $\delta(\phi)$ [°] | c [Pa] | $\delta(c)$ [Pa] | R^2 |
| 0.000 | 0.399 | 0.047 | 21.8 | 2.7 | 9.5 | 61.6 | 0.959 |
| 0.026 | 0.740 | 0.027 | 36.5 | 1.6 | 9.2 | 37.3 | 0.996 |
| 0.053 | 0.975 | 0.047 | 44.3 | 2.7 | -51.1 | 58.0 | 0.994 |
| 0.100 | 0.809 | 0.101 | 39.0 | 5.8 | 557.8 | 94.4 | 0.973 |
| 0.150 | 0.747 | 0.048 | 36.7 | 2.7 | 131.3 | 67.5 | 0.989 |
| 0.200 | 0.580 | 0.022 | 30.1 | 1.3 | 384.2 | 30.8 | 0.995 |
| 0.300 | 0.797 | 0.044 | 38.6 | 2.5 | 218.6 | 64.0 | 0.992 |

Conclusion & Recommendations

This chapter reflects on the research presented in this thesis. Firstly, the results of are discussed in section 7.1. Recommendations for future work are given in section 7.2.

7.1 Discussion & Conclusion

The effects of capillary bridges in static shear strength experiments generally show an increase in (Coulomb) cohesion and only a small deviation in the angle of internal friction, e.g., Richefeu *et al.* (2006, 2008 & 2009)^{46–49} (glass beads) and Rassam & Williams (1999)^{50–52} (tailings) (section 6.2.3). A clear trend in the (Mohr Coulomb) angle of internal friction is observed for the residual shear strength.

The angle of internal friction [figure 6.7(a)] shows a fast increase up to a water content of $W = 0.053$, which theoretically corresponds to the funicular-cluster wetting regime (figure 4.5). Further increase of the water content results in a decrease of the angle of internal friction. Overall, the angle of internal friction shows a very similar trend with respect to the water content as that of the yield strength measured by Fournier *et al.* (2005)¹²¹ (figure 4.7).

Surprisingly, the cohesion remains zero up to the maximum angle of internal friction at $W \leq 0.053$, after which it rapidly increase to a value of about 550 Pa at $W = 0.1$. Further increase of the water content results in a decrease of the cohesion.

From these trends in the Mohr Coulomb criteria, a mechanisms on the influence of capillary bridges on the residual shear strength as a function of the water content can be proposed:

$W < 0.1$ The capillary bridges are ruptured in the shear band once the shear strength is exceeded. Subsequently, (nearly) no new capillary bridges are formed in the shear band, possibly due to an increased distance between the grains due to dilation¹⁰² and by water migration from the shear band¹²³. Capillary bridges in the bulk material generate adhesion and inhibit movement of the individual grains. As a consequence, the angle of internal friction increases due to the increased rigidity of the bulk material, while no or little cohesion is generated by capillary bridges in the shear band.

$W = 0.1$ The water content within the shear band is now high enough to continuously form and pinch off capillary bridges, increasing the cohesion of the material. This is in line with the literature, as the static friction was found to be highest around $W = 0.1$ (figure 4.7, section 4.2.2).

Yet, this maximum shear strength likely corresponds to a maximum energy state E_{\max} of the capillary forces (section 4.2.1). Figure 7.1 illustrates E_{\max} , if the energy added by the capillary bridges is directly proportional to that of the shear strength shown in figure 4.7. Dynamic shearing at this peak value for some distance may cause the capillary bridges to reorganise (e.g., by water migration¹²³) to minimise the energy. This results in the lower energy states E_{w1} and E_{w2} , which correspond to a lower and higher water content, W_1 and W_2 , respectively. This may explain the peculiar transition in σ_g that occurred for $W = 0.1$ at normal pressures $\sigma_n > 1270$ Pa (figure 6.6).

W > 0.1 Both the cohesion and angle of internal friction decrease as the granular material becomes saturated and less capillary bridges per sphere are formed (figure 4.6).

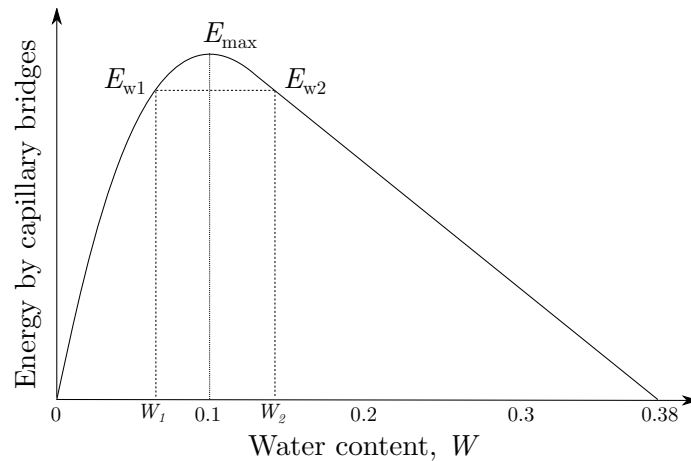


FIGURE 7.1: Schematic representation of energy from capillary forces in the system as a function of the water content. The shape is similar to that found in static shear experiments by Fournier *et al.* (2005)¹²¹ (figure 4.7) and that of the angle of internal friction from the experiments [figure 6.7(a)].

Conclusion

In chapter 3 it is shown how weathering can increase the packing fraction ϕ and reduce the permeability of (granular) tailings material. As a consequence, the water content of the material will likely increase (equation 4.1) and remain higher over a longer time.

If the water content increases to values higher than 0.1, a decrease of the residual shear strength will be the result. This can also be deduced from the literature as the angle of repose of a saturated granular material shows a similar pattern (figure 4.2).

The Mohr Coulomb failure envelopes suggest that around the maximum value of the residual shear strength $W = 0.1$ a transition occurs:

- For $W < 0.1$, the residual shear strength increases by an increasing amount of capillary bridges in the bulk material that provide rigidity.
- For $W = 0.1$, the residual shear strength is increased by an additional cohesion generated by the water bridges that are continuously form and pinched off in the shear band.
- For $W > 0.1$, the residual shear strength is decreased as the capillary bridges merge into increasingly larger clusters as the sample approaches saturation.

7.2 Recommendations

This section lists possible improvements the experiment (section 7.2.1) and gives recommendations for future work (section 7.2.2).

7.2.1 Improvements

Now, for both the grain+plate and plate-only experiments a new sample was prepared to rule out evaporation effects, as it took a day for a single σ_s vs. σ_n curve. It would be time-saving if the water content range was scanned for several normal forces, rather than *vice versa*. Strange behaviour as measured during the grain+plate experiment at $W = 0.1$ [figure 6.5(b)], could be better analysed in this way.

From the angle of internal friction of the grain+plate experiments [figure 6.7(a)], it becomes obvious that there is still interaction in between the grains and the plate as a function of the water content. An increase in the hydrophobicity of the supporting plate can be achieved by using a structured surface that generate superhydrophobic contact angles ($> 150^\circ$)¹¹⁵. This surface needs to be resistant towards wear inflicted by the grains. A possible solution could be the structured metal surfaces used to determine the effect of hydrophobicity on the Leidenfrost temperature at the Physics of Fluids chair (University of Twente-TNW, Enschede, The Netherlands).

In order to test more elaborate models such as that by Fredlund & Rihardo (1993)⁴⁵ (section 4.3.1), the matric suction or Laplace pressure needs to be measured throughout the measurement. This can be measured by piezometers in both the bottom of the lower container and the side of the upper container (near the shear band). This would also allow measurement of possible drainage into the lower container, which may have caused the high angle of internal friction for $W = 0.3$ [figure 6.7(a)].

With the shearing of a compacted material, dilation always occurs¹⁰². Dilation can result in a lower number of liquid bridges that are formed and, hence, a decrease in shear stress. If the packing fraction would decrease to a random loose packing ($\phi \approx 0.57$) the average number of liquid bridges per sphere would drop from 6.5 to approximately 5.7⁴. Measurement of the dilation would thus be advisable. By measuring the distance of the rail and the weight holder of the setup (figure 5.2), dilation could be determined *in-situ*. For example with a laser¹²⁴.

The variations in the calculated values for σ_g are quite large, resulting in a relatively high uncertainty in the angle of internal friction and cohesion (figure 6.7). Increasing the area of the lower container (A_l), will decrease this error (equation 6.6). Yet, increasing this area will also decrease the displacement that can be obtained during an experiment. The author suggests to try a ratio of A_u/A_l of 3/1, which was originally envisaged at the start of the research, but became larger due to removal of the teflon strip from the upper container (appendix B).

7.2.2 Future work

In completion of this work, ideally the static friction would have been determined too. It was expected that a clear peak would have been visible at the start of the motion, but this turned out to give irreproducible results (figure 6.1). Hence, a spring-tipped rod was developed that would be able to measure this static friction (appendix B). In scope of time, these experiments were unfortunately not done in this test series. However, the measuring of the static friction is expected to give a better understanding of the influence of capillary bridges in a granular material.

Parameter space is really huge and still lots of work needs to be done to make the results of these test universally valid. In scope of weathering the following material characteristics could be experimented with:

- Particle size,
- Particle size distribution,
- Surface roughness, and
- Particle shape/angularity.

A follow up study with real tailings material should be done to validate the results of the tests in this research to real tailings dams.

The bottleneck in the setup created during this research is the gap in between the upper container and the supporting plate. It turned out to be a practical challenge to get the gap as small as it is now (appendix B). In scope of weathering of material, i.e., its breaking into progressively smaller fragments, it would be good if this gap can be made smaller to be able to experiment with smaller particle sizes and different, for instance, flaky shapes. It should be noted that decreasing the gap size may result in capillary cohesion between the upper container and the supporting plate.

The apparatus used in these tests may also be used to determine influence of viscosity on the residual and static shear strength of the material. For example, the oil content of a sample could be varied, which would add an additional viscous force (F_v) that is exerted by a liquid bridge. The value for F_v on equally sized spheres (radius R) can be approximated by:

$$F_v = \frac{3\pi\mu R^2}{2s} \left(\frac{ds}{dt} \right), \quad (7.1)$$

where μ is the viscosity of the liquid and s the separation of the grains^{117;134}. It is likely that the F_v can be measured with the test setup used in this research.

List of References

- [1] Carelsen, S. (2013). “Pushing oobleck to the limit: Force response of an intruder in a dense cornstarch suspension”. MSc. thesis, Van der Meer, R.M. and Von Kann, S. (Advs), Physics of Fluids, University of Twente-TNW, Enschede, The Netherlands.
- [2] Hack, H.R.G.K. (2014). “Ground Mechanics: Lecture Notes”. University of Twente-ITC, Enschede, The Netherlands. (in preparation).
- [3] Price, D., de Freitas, M.H., Hack, H.R.G.K., Higginbottom, I., Knill, J. and Maurenbrecher, M. (2009). *Engineering Geology: Principles and Practice*. Berlin, Germany: Springer Berlin Heidelberg.
- [4] Herminghaus, S. (2013). *Wet granular matter: A truly complex fluid*. Series in Soft Condensed Matter: Volume 6. World Scientific Publishing, pre-print edn.
- [5] Halada, K., Shimada, M. and Ijima, K. (2008). “Forecasting of the Consumption of Metals up to 2050”. *Materials Transactions*, **49**(3): pp. 402–410.
- [6] International Copper Study Group (2012). “The World Copper Factbook 2012”. <http://www.icsg.org/> (Internet publication. Accessed: 17th May 2013.).
- [7] Rogich, D.G. and Matos, G.R. (2008). “The global flows of metals and minerals: U.S. Geological Survey Open-File Report 2008–1355”. <http://pubs.usgs.gov/of/2008/1355/> (Internet publication. Accessed: 28th May 2013).
- [8] U.S. Geological Survey (2012). “Copper Statistics 1900 - 2011”. <http://minerals.usgs.gov/ds/2005/140/ds140-coppe.pdf> (Internet publication. Last modification: 8th November 2012.).
- [9] Lottermoser, B.G. (2010). *Mine Wastes: Characterization, Treatment and Environmental Impacts*. Berlin, Germany: Springer, 3rd edn.
- [10] Blight, G. (2010). *Geotechnical Engineering for Mine Waste Storage Facilities*. London, U.K.: Taylor & Francis Group.
- [11] Molson, J.W., Fala, O., Aubertin, M. and Bussière, B. (2005). “Numerical simulations of pyrite oxidation and acid mine drainage in unsaturated waste rock piles”. *Journal of Contaminant Hydrology*, **78**(4): pp. 343–371.
- [12] Tating, F.T., Hack, H.R.G.K. and Jetten, V.G. (2013). “Engineering aspects and time effects of rapid deterioration of sandstone in the tropical environment of Sabah, Malaysia”. *Engineering Geology*, **159**: pp. 20–30.
- [13] Tating, F.T., Hack, H.R.G.K. and Jetten, V.G. (2013). “Weathering effects on discontinuity properties in sandstone in a tropical environment: Case Study at Kota Kinabalu, Sabah Malaysia”. *Bulletin of Engineering Geology and the Environment* (submitted).

- [14] Tating, F.T., Hack, H.R.G.K. and Jetten, V.G. (2013). "Influence of weathering induced iron precipitation on properties of sandstone in a tropical environment". *To be submitted*.
- [15] Bishop, A.W. and Hutchinson, J.N. (1969). *Geotechnical investigation into the causes and circumstances of the disaster of 21st October, 1966*. Tech. rep., The Aberfan Tribunal.
- [16] Johnes, M. and McLean, I. "Aberfan disaster". <http://www.nuffield.ox.ac.uk/politics/aberfan/desc.htm> (Internet publication. Last modification: October 2006.).
- [17] USGS (2013). "Mineral Commodity Summary of Copper". <http://minerals.usgs.gov/minerals/pubs/commodity/copper/mcs-2013-coppe.pdf> (Internet publication. Accessed: 12th October 2013.).
- [18] Martin, T.E., Davies, M.P., Rice, S., Higgs, T. and Lighthall, P.C. (2002). *Stewardship of Tailings Facilities*. Tech. rep., International Institute for Environment and Development.
- [19] Martin, T.E. and Davies, M.P. (2002). "Trends in the stewardship of tailings dams". In "Tailings and Mine Waste '00. Fort Collins, Colorado.", pp. 393–407. Rotterdam: A.A. Balkema.
- [20] U.S. EPA Office of Solid Waste (1994). *Design and evaluation of tailings dams*. Tech. rep., U.S. Environmental Protection Agency, 401 M Street, SW Washington, DC 20460.
- [21] WISE-Uranium. "Chronology of major tailings dam failures". <http://www.wise-uranium.org/mdaf.html> (Internet publication. Accessed: 12th October 2013.).
- [22] Alonso, E.E., Pinyol, N.M. and Puzrin, A.M. (2010). "Earth Dam Sliding Failure: Aznalcóllar Dam, Spain". In "Geomechanics of Failures. Advanced Topics", pp. 129–164. Springer Netherlands.
- [23] Burgos, P., Madejón, P., Madejón, E., Girón, I., Cabrera, F. and Murillo, J. (2013). "Natural remediation of an unremediated soil twelve years after a mine accident: Trace element mobility and plant composition". *Journal of Environmental Management*, **114**(0): pp. 36–45.
- [24] Szymanski, M.B. (1999). *Evaluation of Safety of Tailings Dams*. Bitech Pub Ltd.
- [25] Davies, M.P. and Martin, T.E. (2009). "Mining market cycles and tailings dam incidents". In "Tailings and Mine Waste 2009, Banff, Canada", pp. 3–14.
- [26] Rico, M., Benito, G., Salgueiro, A.R., Déz-Herrero, A. and Pereira, H.G. (2008). "Reported tailings dam failures: A review of the European incidents in the worldwide context". *Journal of Hazardous Materials*, **152**(2): pp. 846–852.
- [27] Hack, H.R.G.K., Price, D.G. and Rengers, N. (2003). "A new approach to rock slope stability – a probability classification (SSPC)". *Bulletin of Engineering Geology and the Environment*, **62**(2): pp. 167–184.
- [28] Acero, P., Ayora, C., Cama, J. and Carrera, J. (2007). "Weathering of pyritic tailings in unsaturated columns: experimental and reactive transport modeling". In R. Cidu and F. Frau (eds.), "IMWA Symposium 2007: Water in Mining Environments", Cagliari, Italy.
- [29] Mihai, S., Deak, S., Deak, G., Oancea, I. and Petrescu, A. (2008). "Tailings dams waste-rock dumps safety assessment using 3D numerical modelling of geotechnical and geophysical data". In "12th International Conference of International Association for Computer Methods and Advances in Geomechanics (IACMAG)", .

- [30] Mihai, S., Zlagnean, M., Oancea, I. and Petrescu, A. (2009). “Tailings dams stability analysis using numerical modelling of geotechnical and geophysical data”. In “EGU General Assembly 2009”, p. 3219.
- [31] Martínez-Pagán, P., Faz, A., Acosta, J.A., Carmona, D.M. and Martínez-Martínez, S. (2011). “A multidisciplinary study for mining landscape reclamation: A study case on two tailing ponds in the Region of Murcia (SE Spain)”. *Physics and Chemistry of the Earth, Parts A/B/C*, **36**(16): pp. 1331–1344.
- [32] Riaza, A. and Müller, A. (2010). “Hyperspectral remote sensing monitoring of pyrite mine wastes: a record of climate variability (Pyrite Belt, Spain)”. *Environmental Earth Sciences*, **61**: pp. 575–594.
- [33] Turner, A.K. and Schuster, L.R. (eds.) (1996). *Landslides: investigation and mitigation*. Washington D.C., U.S.A.: National Academy Press.
- [34] Fernandez-Merodo, J., Castellanza, R., Mabssout, M., Pastor, M., Nova, R. and Parma, M. (2007). “Coupling transport of chemical species and damage of bonded geomaterials”. *Computers and Geotechnics*, **34**(4): pp. 200–215.
- [35] Duncan, J.M. and Wright, S.G. (2005). *Soil Strength and Slope Stability*. New Jersey, U.S.A.: John Wiley & Sons, Inc.
- [36] Devasahayam, S. (2007). “Application of particle size distribution analysis in evaluating the weathering in coal mine rejects and tailings”. *Fuel Processing Technology*, **88**(3): pp. 295–301.
- [37] Utili, S. (2004). *Evolution of natural slopes subject to weathering: an analytical and numerical study*. Ph.D. thesis, Politecnico di Milano, Milan, Italy.
- [38] Utili, S. and Crosta, G.B. (2011). “Modeling the evolution of natural cliffs subject to weathering: 1. Limit analysis approach”. *Journal of Geophysical Research*, **116**(F1).
- [39] Utili, S. and Crosta, G.B. (2011). “Modeling the evolution of natural cliffs subject to weathering: 2. Discrete element approach”. *Journal of Geophysical Research*, **116**(F1).
- [40] Huisman, M. (2006). *Assessment of rock mass decay in artificial slopes*. Ph.D. thesis, Hack, H.R.G.K. and Nieuwenhuis, J.D. (Advs), Engineering Geology, University Delft; ITC Enschede, Delft/Enschede, The Netherlands.
- [41] Huisman, M., Hack, H.R.G.K. and Nieuwenhuis, J.D. (2006). “Predicting Rock Mass Decay in Engineering Lifetimes: The Influence of Slope Aspect and Climate”. *Environmental & Engineering Geoscience*, **12**(1): pp. 39–51.
- [42] Huisman, M., Nieuwenhuis, J.D. and Hack, H.R.G.K. (2011). “Numerical modelling of combined erosion and weathering of slopes in weak rock”. *Earth Surface Processes and Landforms*, **36**(13): pp. 1705–1714.
- [43] Zandarín, M.T., Oldecop, L.A., Rodríguez, R. and Zabala, F. (2009). “The role of capillary water in the stability of tailing dams”. *Engineering Geology*, **105**(1–2): pp. 108–118.
- [44] Bridge, J.S. and Demicco, R.V. (2008). *Earth Surface Processes, Landforms and Sediment Deposits*. Cambridge, U.K.: Cambridge University Press.
- [45] Fredlund, D.G. and Rahardjo, H. (1993). *Soil mechanics for unsaturated soils*. New York, U.S.A.: John Wiley & Sons, Inc.
- [46] Richefeu, V., El Youssoufi, M.S. and Radjai, F. (2006). “Shear strength properties of wet granular materials”. *Physical Review E*, **73**(5): p. 051304.

- [47] Richefeu, V., Radjaï, F. and El Youssoufi, M.S. (2006). “Stress transmission in wet granular materials”. *The European Physical Journal E: Soft Matter and Biological Physics*, **21**(4): pp. 359–369.
- [48] Richefeu, V., El Youssoufi, M.S., Peyroux, R. and Radjaï, F. (2008). “A model of capillary cohesion for numerical simulations of 3D polydisperse granular media”. *International Journal for Numerical and Analytical Methods in Geomechanics*, **32**(11): pp. 1365–1383.
- [49] Richefeu, V., Youssoufi, M.S.E., Azéma, E. and Radjaï, F. (2009). “Force transmission in dry and wet granular media”. *Powder Technology*, **190**(1–2): pp. 258–263.
- [50] Rassam, D.W. and Williams, D.J. (1999). “A relationship describing the shear strength of unsaturated soils”. *Canadian Geotechnical Journal*, **36**(2): pp. 363–368.
- [51] Rassam, D.W. and Williams, D.J. (1999). “A numerical study of steady state evaporative conditions applied to mine tailings”. *Canadian Geotechnical Journal*, **36**(4): pp. 640–650.
- [52] Rassam, D.W. and Williams, D.J. (1999). “Bearing Capacity of Desiccated Tailings”. *Journal of Geotechnical and Geoenvironmental Engineering*, **125**(7): pp. 600–609.
- [53] Rassam, D.W. (2002). “Variation of evaporative and shear strength parameters along a tailings delta”. *Canadian Geotechnical Journal*, **39**(1): pp. 32–45.
- [54] Gan, J.K.M., Fredlund, D.G. and Rahardjo, H. (1988). “Determination of the shear strength parameters of an unsaturated soil using the direct shear test”. *Canadian Geotechnical Journal*, **25**(3): pp. 500–510.
- [55] Nam, S., Gutierrez, M., Diplas, P. and Petrie, J. (2011). “Determination of the shear strength of unsaturated soils using the multistage direct shear test”. *Engineering Geology*, **122**(3–4): pp. 272–280.
- [56] Abramson, L.W., Lee, T.S., Sharma, S. and Boyce, G.M. (2002). *Slope stability and stabilization methods*. New York, U.S.A.: John Wiley & Sons, Inc., 2nd edn.
- [57] Hartley, R.R. and Behringer, R.P. (2003). “Logarithmic rate dependence of force networks in sheared granular materials”. *Nature*, **421**(6926): pp. 928–931.
- [58] Panien, M., Schreurs, G. and Pfiffner, A. (2006). “Mechanical behaviour of granular materials used in analogue modelling: insights from grain characterisation, ring-shear tests and analogue experiments”. *Journal of Structural Geology*, **28**(9): pp. 1710–1724.
- [59] Grotzinger, J. and Jordan, T.H. (2010). *Understanding Earth*. New York, U.S.A.: W. H. Freeman & Company, 6th edn.
- [60] U.S. Geological Survey (2012). “Landslide events”. <http://landslides.usgs.gov/recent/> (Internet publication. Last modification: 3rd December 2012.).
- [61] International Consortium on Landslides, UNESCO. “International Programme on Landslides”. <http://iplhq.org/category/home/> (Internet publication. Accessed: 12th October 2013.).
- [62] De Mulder, E.F.J., Hack, H.R.G.K. and Van Ree, C.C.D.F. (2012). *Sustainable Development and Management of the Shallow Subsurface*. London, U.K.: The Geological Society of London.
- [63] Bland, W. and Rolls, D. (1998). *Weathering: An introduction to the scientific principles*. New York, U.S.A.: Arnold.

-
- [64] Hencher, S.R. and McNicholl, D.P. (1995). “Engineering in weathered rock”. *Quarterly Journal of Engineering Geology and Hydrogeology*, **28**(3): pp. 253–266.
- [65] Brady, N.C. (1990). *The Nature and Properties of Soils*. London, U.K.: Macmillan Publishing Company, 10th edn.
- [66] Halsey, D.P., Mitchell, D.J. and Dews, S.J. (1998). “Influence of climatically induced cycles in physical weathering”. *Quarterly Journal of Engineering Geology and Hydrogeology*, **31**(4): pp. 359–367.
- [67] Fookes, P.G., Gourley, C.S. and Ohikere, C. (1988). “Rock weathering in engineering time”. *Quarterly Journal of Engineering Geology and Hydrogeology*, **21**(1): pp. 33–57.
- [68] Agus, S.S. and Schanz, T. (2005). “Swelling Pressures and Wetting-Drying Curves of a Highly Compacted Bentonite-Sand Mixture”. In T. Schanz (ed.), “Unsaturated Soils: Experimental Studies”, vol. 1 of *Springer Proceedings in Physics, Vol. 93*, pp. 241–256. Springer Berlin Heidelberg.
- [69] Enriquez, O.R., Marin, A.G., Winkels, K.G. and Snoeijer, J.H. (2012). “Freezing singularities in water drops”. *Physics of Fluids*, **24**(9): p. 091102.
- [70] Haynes, W. and Lide, D. (eds.) (2013–2014). *Handbook of Chemistry and Physics*. Internet Version 2013. CRC, 94nd edn.
- [71] Hall, K. (1999). “The role of thermal stress fatigue in the breakdown of rock in cold regions”. *Geomorphology*, **31**(1–4): pp. 47–63.
- [72] Willies, L. and Weisgerber, G. (2000). “The use of fire in prehistoric and ancient mining-firesetting”. *Paléorient*, **26**(2): pp. 131–149.
- [73] Mustoe, G.E. (1982). “The origin of honeycomb weathering”. *Geological Society of America Bulletin*, **93**(2): pp. 108–115.
- [74] Hencher, S.R., Lee, S.G., Carter, T.G. and Richards, L.R. (2011). “Sheeting Joints: Characterisation, Shear Strength and Engineering”. *Rock Mechanics and Rock Engineering*, **44**(1): pp. 1–22.
- [75] Holzhausen, G.R. (1989). “Origin of sheet structure, 1. Morphology and boundary conditions”. *Engineering Geology*, **27**(1–4): pp. 225–278.
- [76] Fookes, P.G. and Hawkins, A.B. (1988). “Limestone weathering: its engineering significance and a proposed classification scheme”. *Quarterly Journal of Engineering Geology and Hydrogeology*, **21**(1): pp. 7–31.
- [77] Price, D.G. (1995). “Weathering and weathering processes”. *Quarterly Journal of Engineering Geology and Hydrogeology*, **28**(3): pp. 243–252.
- [78] Fowler, T.A., Holmes, P.R. and Crundwell, F.K. (2001). “On the kinetics and mechanism of the dissolution of pyrite in the presence of *Thiobacillus ferrooxidans*”. *Hydrometallurgy*, **59**(2–3): pp. 257–270.
- [79] Wenner, D. and Wannemacher, H. (2009). “Alborz Service Tunnel in Iran: TBM Tunnelling in Difficult Ground Conditions and its Solutions”. In “1st Regional and 8th Iranian Tunneling Conference”, Iranian Tunnelling Association (IRTA) & Tarbiat Modares University, Tehran.
- [80] Saunders, M.K. and Fookes, P.G. (1970). “A review of the relationship of rock weathering and climate and its significance to foundation engineering”. *Engineering Geology*, **4**(4): pp. 289–325.

- [81] de Jong, R. (2012). “Droplet impact on rough surfaces”. MSc. thesis, Van der Meer, R.M. (Adv), Physics of Fluids, University of Twente-TNW, Enschede, The Netherlands.
- [82] Hack, H.R.G.K. (1996). *Slope Stability Probability Classification - SSPC*. Ph.D. thesis, Delft University of Technology.
- [83] Nicholson, D.T. (2004). “Hazard assessment for progressive, weathering-related breakdown of excavated rockslopes”. *Quarterly Journal of Engineering Geology and Hydrogeology*, **37**(4): pp. 327–346.
- [84] British Standards Institution (1981). *BS5930 (1981): Code of practice for site investigations*. British Standards Institution.
- [85] British Standards Institution (1999). *BS5930 (1999): Code of practice for site investigations*. British Standards Institution.
- [86] Hencher, S.R. (2008). “The ‘New’ British and European Standard Guidance on Rock Description”. *Ground Engineering*, **41**(7): pp. 17–21 (online). (New Civil Engineer) <http://www.nce.co.uk/eurocodes/1709994.article> (Accessed: 17th November 2013).
- [87] Colman, S.M. and Dethier, D.P. (eds.) (1986). *Rates of chemical weathering of rocks and minerals*. Orlando, U.S.A.: Academic Press.
- [88] Nordstrom, D.K., Alpers, C.N., Ptacek, C.J. and Blowes, D.W. (2000). “Negative pH and Extremely Acidic Mine Waters from Iron Mountain, California”. *Environmental Science & Technology*, **34**(2): pp. 254–258.
- [89] Fields, S. (2003). “The earth’s open wounds: abandoned and orphaned mines”. *Environmental Health Perspectives*, **111**(3): pp. A154–A161.
- [90] Kantongo, C. (2005). “Ground conditions and support systems at 1 shaft, Konkola mine, Chililabombwe, Zambia.” In “Third Southern African Base Metals Conference”, Symp. Series S39. South African Institute of Mining and Metallurgy.
- [91] Alonso, E.E. and Gens, A. (2006). “Aznalcóllar dam failure. Part 1: Field observations and material properties”. *Géotechnique*, **56**(3): pp. 165–183.
- [92] Alonso, E.E. and Gens, A. (2006). “Aznalcóllar dam failure. Part 2: Stability conditions and failure mechanism”. *Géotechnique*, **56**(3): pp. 185–201.
- [93] Davies, M.P. (2002). “Tailings impoundment failures: Are geotechnical engineers listening?” *Geotechnical News*, pp. 31–36.
- [94] Martin, T.E. (1999). “Characterization of pore pressure conditions in upstream tailings dams Characterization of pore pressure conditions in upstream tailings dams”. In “Tailings and Mine Waste ’99. Fort Collins, Colorado.”, 6, pp. 302–314. A.A. Balkema.
- [95] Martin, T.E. and McRoberts, E.C. (1999). “Some considerations in the stability analysis of upstream tailings dams”. In “Tailings and Mine Waste ’99. Fort Collins, Colorado.”, 6, pp. 287–302. A.A. Balkema.
- [96] Petronic, B.M., Al, T.A., Weaver, L. and Hall, D. (2009). “Identification and characterization of secondary minerals formed in tungsten mine tailings using transmission electron microscopy”. *Applied Geochemistry*, **24**(12): pp. 2222–2233.
- [97] Graupner, T., Kassahun, A., Rammlmair, D., Meima, J.A., Kock, D., Furche, M., Fiege, A., Schippers, A. and Melcher, F. (2007). “Formation of sequences of cemented layers and hardpans within sulfide-bearing mine tailings (mine district Freiberg, Germany)”. *Applied Geochemistry*, **22**(11): pp. 2486–2508.

-
- [98] Jambor, J.L., Blowes, D.W. and Ptacek, C. (2006). “Mineralogy of mine wastes and strategies for remediation”. In D. Vaughan and R.A. Wogelius (eds.), “Environmental mineralogy”, vol. 2, pp. 255–290. European Mineralogical Union.
- [99] Bagnold, R. (1954). *The Physics of Blown Sand and Desert Dunes*. London, U.K.: Methuen and Co., Ltd.
- [100] Nowak, S., Samadani, A. and Kudrolli, A. (2005). “Maximum angle of stability of a wet granular pile”. *Nature Physics*, **1**(1): pp. 50–52.
- [101] Hustrulid, W.A., McCarter, M.K. and Van Zyl, D.J.A. (2000). *Slope stability in surface mining*. Partially available via books.google.com, Accessed: 26th November 2013: SME.
- [102] Duran, J. (2000). *Sand, Powders, and Grains: An Introduction to the Physics of Granular Materials*. Partially Ordered Systems. New York, U.S.A.: Springer-Verlag New York, Inc.
- [103] Statistical Office of Republic Of Serbia (2012). “2011 Census of Population, Households and Dwellings in the Republic of Serbia”. <http://pod2.stat.gov.rs/Objavljenepublikacije/Popis2011/Starost%20i%20pol-Age%20and%20sex.pdf>.
- [104] Corsi, S. (2006). *Environmental Assessment of RTB Bor Operations*. Final report, ERM.
- [105] DMT GmbH, Faculty of Mining & Geology of the University of Belgrade and Projmetal ad (2007). *RTB Bor Tailings Ponds Remediation Study*. Tech. rep., Consortium.
- [106] Van der Wijk, M. (2011). *Bor Regional Development Project Serbia: Inception report*. Final version, Witteveen+Bos, Deventer, The Netherlands.
- [107] Section, U.N.C. (2007). “Road map of Serbia”. <http://www.un.org/Depts/Cartographic/map/profile/serbia.pdf> (Internet publication. Accessed: 11th October 2013).
- [108] Pachen, H. (2011). *Bor Regional Development Project Serbia*. Geotechnical Investigation, Geotron B.V.
- [109] Barnes, H., Hutton, J. and Walters, K. (1989). *An Introduction to Rheology*. Amsterdam, the Netherlands: Elsevier.
- [110] Dullien, F. (1992). *Porous Media: Fluid Transport and Pore Structure*. San Diego, U.S.A.: Academic Press. Inc., 2nd edn.
- [111] Herminghaus, S. (2005). “Dynamics of wet granular matter”. *Advances in Physics*, **54**(3): pp. 221–261.
- [112] Kohonen, M.M., Geromichalos, D., Scheel, M., Schier, C. and Herminghaus, S. (2004). “On capillary bridges in wet granular materials”. *Physica A: Statistical Mechanics and its Applications*, **339**(1–2): pp. 7–15.
- [113] Hornbaker, D.J., Albert, R., Albert, I., Barabási, A.L. and Schiffer, P. (1997). “What keeps sandcastles standing?” *Nature*, **387**(6635): p. 765.
- [114] Halsey, T.C. and Levine, A.J. (1998). “How Sandcastles Fall”. *Physical Review Letters*, **80**(14): pp. 3141–3144.
- [115] de Gennes, P.G., Brochart-Wyart, F. and Quéré, D. (2004). *Capillarity and Wetting Phenomena: Drop, Bubbles, Pearls, Waves*. New York, U.S.A.: Springer.

- [116] Hamaker, H.C. (1937). “The London–van der Waals attraction between spherical particles”. *Physica*, **4**(10): pp. 1058–1072.
- [117] Iveson, S.M., Beath, J.A. and Page, N.W. (2002). “The dynamic strength of partially saturated powder compacts: the effect of liquid properties”. *Powder Technology*, **127**(2): pp. 149–161.
- [118] Mitarai, N. and Nori, F. (2006). “Wet granular materials”. *Advances in Physics*, **55**(1–2): pp. 1–45.
- [119] Scheel, M., Seemann, R., Brinkmann, M., Di Michiel, M., Sheppard, A., Breidenbach, B. and Herminghaus, S. (2008). “Morphological clues to wet granular pile stability”. *Nature Materials*, **7**(3): pp. 189–193.
- [120] Terzaghi, K. (1943). *Theoretical soil mechanics*. New York, U.S.A.: John Wiley & Sons, Inc.
- [121] Fournier, Z., Geromichalos, D., Herminghaus, S., Kohonen, M.M., Mugele, F., Scheel, M., Schulz, M., Schulz, B., Schier, C., Seemann, R. and Skudelný, A. (2005). “Mechanical properties of wet granular materials”. *Journal of Physics: Condensed Matter*, **17**(9): pp. S477–S502.
- [122] Willett, C.D., Adams, M.J., Johnson, S.A. and Seville, J.P.K. (2003). “Effects of wetting hysteresis on pendular liquid bridges between rigid spheres”. *Powder Technology*, **130**(1–3): pp. 63–69.
- [123] Mani, R., Kadau, D. and Herrmann, H.J. (2012). “Liquid migration in sheared unsaturated granular media”. *Granular Matter*, pp. 1–8.
- [124] Losert, W., Géminard, J.C., Nasuno, S. and Gollub, J.P. (2000). “Mechanisms for slow strengthening in granular materials”. *Physical Review E*, **61**: pp. 4060–4068.
- [125] Bagnold, R.A. (1966). “The Shearing and Dilatation of Dry Sand and the ‘Singing’ Mechanism”. *Proceedings of the Royal Society of London. Series A, Mathematical and Physical Sciences*, **295**(1442): pp. 219–232.
- [126] Chen, Y., Zhao, Y., Gao, H. and Zheng, J. (2011). “Liquid bridge force between two unequal-sized spheres or a sphere and a plane”. *Particuology*, **9**(4): pp. 374–380.
- [127] Ashurst, W., Yau, C., Carraro, C., Maboudian, R. and Dugger, M. (2001). “Dichlorodimethylsilane as an anti-stiction monolayer for MEMS: a comparison to the octadecyltrichlorosilane self-assembled monolayer”. *Journal of Microelectromechanical Systems*, **10**(1): pp. 41–49.
- [128] van der Wal, P. and Steiner, U. (2007). “Super-hydrophobic surfaces made from Teflon”. *Soft Matter*, **3**(4): pp. 426–429.
- [129] Copley Control/ThrustTube Motors. “Datasheet of the linear motor: ThrustTube[®] TBX 2506”. <http://www.copleycontrols.com/motion/pdf/QM0006-AAE.pdf> (Internet publication. Accessed: 28th November 2013.).
- [130] FUTEK. “Datasheet of the load cell: FUTEK model LSM300, item FSH00006”. <http://www.futek.com/files/pdf/Product%20Drawings/lsm300.pdf> (Internet publication. Accessed: 28th November 2013.).
- [131] Utermann, S., Aurin, P., Benderoth, M., Fischer, C. and Schröter, M. (2011). “Tailoring the frictional properties of granular media”. *Physical Review E*, **84**(3): p. 031306.

- [132] Snoeijer, J.H., Ellenbroek, W.G., Vlugt, T.J.H. and van Hecke, M. (2006). “Sheared Force Networks: Anisotropies, Yielding, and Geometry”. *Physical Review Letters*, **96**: p. 098001.
- [133] Crombaghs, M., de Min, E. and van Hees, G.S. (2002). *The first absolute gravity measurements in The Netherlands. Period 1991 - 1999*. Tech. rep., Netherlands Geodetic Commission, Delft, The Netherlands.
- [134] Iveson, S.M. and Litster, J.D. (1998). “Growth regime map for liquid-bound granules”. *AIChE Journal*, **44**(7): pp. 1510–1518.
- [135] Lerouge, C., Bailly, L., Béchu, E., Fléhoc, C., Genna, A., Lescuyer, J.L., Stein, G., Gillot, P.Y. and Kozelj, D. (2005). “Age and origin of advanced argillic alteration at the Bor Cu-Au deposit, Serbia”. In J. Mao and F.P. Bierlein (eds.), “Mineral Deposit Research: Meeting the Global Challenge”, pp. 541–544. Springer Berlin Heidelberg.
- [136] Jankovic, S. (1990). “Types of copper deposits related to volcanic environment in the Bor district, Yugoslavia”. *Geologische Rundschau*, **79**(2): pp. 467–478.
- [137] Clark, A.H. and Ullrich, T.D. (2004). “ ^{40}Ar - ^{39}Ar age data for andesitic magmatism and hydrothermal activity in the Timok Massif, eastern Serbia: implications for metallogenetic relationships in the Bor copper-gold subprovince”. *Mineralium Deposita*, **39**(2): pp. 256–262.
- [138] Petrović, D., Svrkota, I., Stojadinović, S., Milić, V., Pantović, R. and Milićević, Ž. (2012). ““Borska Reka” orebody, the future of the exploitation in Bor mine”. *Underground Mining Engineering*, **21**: pp. 83–88.
- [139] Karamata, S., Djordjevic, V., Djordjevic, P., Milojković, R. and Milovanović, D. (1981). “Study of horizontal and vertical distribution of hydrothermal alteration in the Bor area (Proučavanje horizontalne i vertikalne distribucije okolorudnih alteracija stena i njihove zakonomernosti u istražnom prostoru Bor) (in Serbian)”. *Rudarsko-geološki fakultet, Beograd*.
- [140] Karamata, S., Knežević, V., Djordjevic, P. and Milovanović, D. (1983). “Alterations in the Bor copper deposit and their significance for explanation of the ore genesis. (in Serbian)”. *Geologicky Zbornik*, **34**(1): pp. 45–52.

Southeast “Ostrelj” overburden waste dump

The ‘Southeast’ or “Ostrelj” overburden waste dump is the largest of its kind in the Bor area with a total area of approximately 1.8 km² and hosting more than 170 million m³ of overburden material. It is located adjacent to the eastern part Bor town (figure 3.8). This overburden waste dump is a nexus of the old Bor deposit, of which exploitation started in 1924^{104;105}. The overburden waste dump was closed alongside the Bor open-pit in 1993, but part of it is still used to dump and burn waste of the town.

A.1 General description

The material which lays in Ostrelj overburden waste dump originally was the host rock of the Bor deposits and, to some extent, (low grade) ore. This makes the original setting prior to excavation of interest for this investigation.

The Bor deposit is a cupriferous pyrite deposit, with three major orebodies: “Tilva Rosh”, “Choka Dulkan” and “Tilva Mika”¹³⁵.

The minerals that are present in the orebodies are vertically zoned as:

Upper orebody Massive type mineralisation: abundance of pyrite (60 – 70 %) and cupriferous minerals like: chalcocite, covellite and enargite.

Lower orebody Stockwork with or without dissemination type mineralisation: dominance of bornite, chalcopyrite and pyrite (less then upper part).

Hence, it can be expected that these minerals are also present in the waste dump, but in a reverse order: The minerals of the upper orebody in the oldest, deepest parts, and the minerals of the lower orebody in the newest, surfacing parts of the overburden waste dump.

The orebodies are hosted by porphyritic* hornblende-biotite andesites with some dacites and their equivalent pyroclastics^{†136}. These andesites are also called **timocites** after the nearby Timok river¹³⁷ and are expected to be the major constituent of Ostrelj overburden waste dump.

*Porphyry are igneous rocks that have large crystals, i.e., phenocrysts.

†In this case, pyroclastics are rocks that consist of only the andesite material, without large phenocrysts.

During a preliminary remediation study¹⁰⁵, some of the physical and mechanical properties of the rocks in the Bor district have been determined and are here presented in table A.1.

| Type of rock | Physical and mechanical properties | | | | | |
|----------------------------------|------------------------------------|----------------------------------|------------------------------|--------------------------------|-------------------|---|
| | Density (t/m ³) | Compressive strength (MPa) | Bending strength (MPa) | Extension strength (MPa) | Cohesion (MPa) | Angle of internal friction (°) |
| Quartz-diorite- porphyrite | 2,52 - 2,55 | 40,73 – 68,16 | | 4,69 – 7,97 | 7,65 – 13,30 | 51° - 52° |
| Hornblende-biotite andesite | 2,56 - 2,67 | 73,23 – 89,00 | | 6,88 – 10,35 | 13,60 – 16,63 | 50° 30' - 54° |
| Kaoline andesite | 2,64 – 3,05 | 24,7 – 68,6 | 8,54 – 16,64 | 4,6 – 9,7 | 5,5 – 14,0 | 17° 30' - 41° |
| Chlorite andesite | 2,70 - 2,77 | 69,20 – 127,60 | | 8,2 – 10,2 | 11,0 - 18,0 | 36° 10' - 37° |
| Hydro-thermally altered rocks | 2,50 - 2,64 | 31,19 – 67,52 | | 3,47 – 9,04 | 5,58 – 12,97 | 46° - 53° |
| Volcano – clastic rocks | 2,70 – 2,77 | 58,1 – 89,6 | 6,6 – 9,8 | 7,2 – 9,3 | 14,0 – 18,0 | 36° - 48° |
| Bor's conglomerates | 2,77-2,78 | 56,7 – 76,6 | 6,8 – 7,7 | 7,6 – 8,4 | 13,0 – 18,0 | 39° - 43° 30' |

TABLE A.1: Physical and mechanical properties of rocks at Bor's mining field. It needs to be emphasised that the type of tests done nor the mathematical model to which the cohesion and angle of internal friction were fitted, are mentioned by the source. [DMT GmbH, University of Belgrade, and Projmetal ad (2007)¹⁰⁵]

A.2 Expected weathering

Jankovic (1990)¹³⁶ describes the most common alteration type of the hosting andesites as “pervasive silicification coupled with advanced argillic alteration”, which is particularly the case in the upper part of the orebodies (± 155 m depth¹³⁸). Argillic alteration essentially is the weathering of certain minerals under the influence of environmental conditions into clay minerals like kaolin. Kaolinisation is widespread and abundant in Bor, but other available argillic minerals in the deposit are pyrophyllite, diaspore, and alunite were also observed. In particular, alunite was observed abundantly in pyroclastic rocks in the upper parts of the orebodies [Refs. Karamata *et al.* (1981¹³⁹ & 1983¹⁴⁰) in Jankovic (1990)¹³⁶].

Table A.1 shows that this kaoline andesite has a reduced cohesion, strength characteristics and angle of internal friction as compared to its original hornblende-biotite andesite¹⁰⁵. Depending on the amount of this hornblende-biotite andesite in the waste dump, it can be expected that weathering (i.e. kaolinisation) does have a impact on the stability of the waste heaps. These kaolin andesites ultimately form a quasi-plastic mass under physical weathering processes, like wetting/drying, freeze/thaw, and thermal changes¹⁰⁵ (see section 2.1.1).

A.3 Observations

Three colours that were previously observed at both the tailings [figure 3.11(a)] and Bor's old open-pit (orange, yellow, and grey), are also present at Ostrelj overburden waste dump.

- Orange and yellow often correlates to moderately to completely weathered porphyry biotite-hornblende andesites^{104;136}.
- Grey can be two different materials:
 1. hornblende-biotite andesites (timocites) in non-weathered condition, or
 2. the pyroclastic equivalent of the timocites, as they do not seem to be porphyric and have less phenocrysts.

Although information on the build-up stages have not been provided, it is expected that the northwestern part of Ostrelj Overburden is the oldest part. This assumption has two motives:

1. The northwest is closest to the mine. It is highly probable that the mining company (RTB Bor) will have started dumping close to the open-pit first.
2. The northwestern part shows more signs of vegetation, indicating that the remaining soil is not acidic anymore and pyrite oxidation has (nearly) stopped.

Different weathering profiles at different locations around Ostrelj overburden waste dump confirm this assumption. For example, figures A.1 and A.2 show profiles in northwestern Ostrelj overburden, while figure A.3 presents a profile in the southeast.

The material in the northwestern part is almost complete degraded to yellow clay, often encapsulating grey cobbles that crumble in hand, implying that the Intact Rock Strength (IRS) is less than 1.25 MPa³. This clay is also found in the slopes in the southeastern part, but to a much lesser extent. Also, on all slopes a duricrust of about 5 – 10 mm thick was found, that consisted of cemented gravel- to sand-sized particles.

An orange/red layer is present in all profiles and is likely a layer that is stained by ferric oxide, a secondary product of pyrite oxidation. This ferric oxide is probably precipitated into this layer from the material above, which has a yellow colour. This is best illustrated by the SE-profile of figure A.1: This part of the dump was probably not used for a while, giving the material a chance to weather and kaolinise. Later on, the dump was probably reused by dumping a layer of fresh material on top of the clay that again started to weather. During the weathering of the second deposition, the ferric oxide could not percolate through the kaolinised layer of the first deposition. Hence, the reoccurrence of the yellow-red layers. The ferric oxide production in the lower layers also may have been enhanced by acid which percolated from the layers above¹²⁻¹⁴.



FIGURE A.1: Weathering profile at the northwestern part of Ostrelj overburden waste dump. A: Grey crust; B: ± 15 cm thick yellow layer of completely weathered residual clay; C: ± 15 –20 cm thick red sandy clay layer; D: 8 cm thick grey residual clay with some red spots; E: Orange sandy clay. [7th November 2011, Bor, Serbia (44°5'16.2" N; 22°6'37" E)]



FIGURE A.2: Weathering profile at the northwestern part of Ostrelj overburden waste dump. A: Orange crust; B: 22 cm thick orange layer of sandy clay; C: Grey *in-situ* residual soil in a matrix of yellow clay. [10th November 2011, Bor, Serbia (44°5'6.43" N; 22°6'0.6317" E)]



FIGURE A.3: Weathering profile at the southeastern part of Ostrelj overburden waste dump. A: Yellow crust; B: Orange clayey sand; C: grey sandy gravel. The red circle indicates a cobbler of weathered (kaolinised) andesite. [2nd November 2011, Bor, Serbia (44°4'7.77" N; 22°8'8.95" E)]

Experimental setup phases

The experimental setup that was used in this research (chapter 5) was completely build from scratch by the author and the technicians of the Physics of Fluids (PoF) chair of the University of Twente. The purpose of this chapter is to show the test setup as used (figure 5.1). This may be useful for future research.

B.1 Phase 1: Sketch

Figure B.1 presents a sketch of the principle of the setup. The shear box consist of three parts (from bottom to top):

Lower container which is recessed in a plate.

Upper container which is larger than the lower container and at a fixed height above the plate.

Holder that generates a normal force by inserting weight, e.g., by filling it by sand.

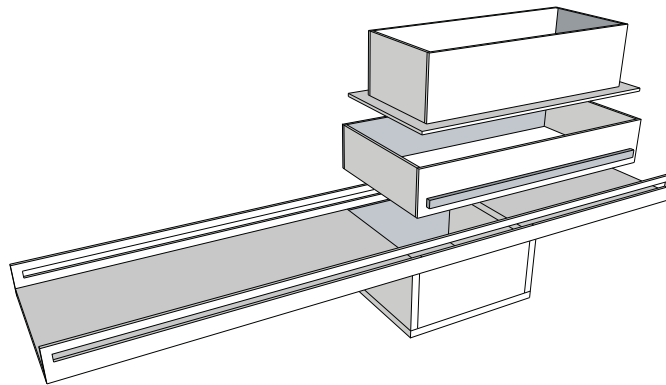


FIGURE B.1: Preliminary sketch of setup made in Google Sketch-Up showing the principle. From bottom to top: Smaller, lower container recessed in a plate with guiding rails; Larger, upper container with guiders, which is to be attached to a linear motor; Lid fitting the upper container, which is equipped with a reservoir that can be filled with sand or other material to produce a normal force.

B.2 Phase 2: Technical drawing

After the first ideas a technical drawing was made as shown in figure B.2.

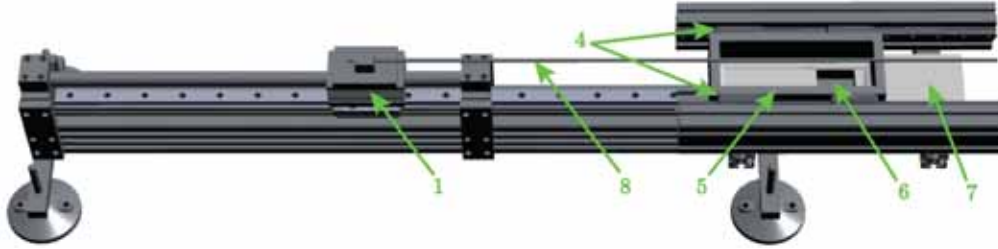


FIGURE B.2: Conceptual first digital drawing of the setup. Here the in first instance implemented two guiding rails (4) and Teflon strip [inside of the upper container (5)] are visible. 1. Linear motor, 4. Guiding rails, 5. Upper container, 6. Lower container, 7. Supporting plate, 8. Rod.

B.3 Phase 3: Inventory

From the (simple) concept sketched in figure B.1 and the elaborated digital drawing in figure B.2, the setup has evolved as shown in figure 5.1. Below the four aspects of the setup (i.e., shear box, actuation, measurement, and sample) are listed alongside the chosen options.

Shear box

- Ratio upper/lower container area: $5^2/3:1$ (section 5.1),
- Supporting plate material: Teflon (section 5.1.1),
- Normal force distribution: PVC plate,
- Normal force generation: Stainless steel weights (3x 61.7-61.8 g, 2x 246–251 g, 6x 361–373 g),
- Gap size (upper container-plate): Approximately $350\ \mu\text{m}$ (section 5.1.2)

The dimension of the setup are given in table B.1 below.

TABLE B.1: Geometrical parameters of the setup.

| Geometrical parameter | Value [mm] | Description |
|-----------------------|------------|--|
| l_u | 240 | Inner length upper container |
| w_u | 85 | Inner width upper container |
| h_u | 64 | Height upper container |
| t_u | 15 | Upper container wall thickness |
| l_l | 60 | Inner length lower container |
| w_l | 60 | Inner width lower container |
| h_l | 25 | Height lower container |
| r_l | 3 | Radius corners lower container |
| l_{pl} | 740 | Length teflon plate |
| w_{pl} | 135 | Width teflon plate |
| t_{pl} | 15 | Thickness teflon plate |
| x_l | 200 | Distance center of lower container to the closest end face of the teflon plate |
| l_{rod} | 860 | Length rod |
| r_{rod} | 6 | Radius rod |

Actuation

- Actuator: TrustTube TBX 2506 (section 5.2),
- Controller: Copley controls XTL-230-36S,
- Controller software: Copley controls CME2,
- Guidance of upper container: Rails with ball bearings,
- Rod: 6 mm radius hollow stainless steel tube.

Measurement

- Load cell: FUTEK LSM300 (section 5.3),
- Load cell placement: At point of application of the rod at the upper container,
- Power source: 12 V (motorcycle) battery,
- Data acquisition: National Instruments USB-4432 (section 5.3.3).
 - Sample rate: 5 kHz,
 - Recording software: Labview Signalexpress,
 - Implementation in analysis Matlab script: TDMS-reader (third party plug-in).

Sample (section 5.4)

- Material: Soda lime glass beads (density 2490 kg m^{-3})
- Particle shape: Spherical
- Particle size: 1 mm ($\pm 10\%$, indicated by manufacturer)

B.4 Phase 4: Adjustments

Many issues came up after the first setup was build based upon the first technical drawing. Below the adjustments that are made are summarised:

Rails

Using two rails on both sides of the container causes misalignment of the upper container with the plate, while maintaining a constant rail friction. To achieve adequate alignment, both rails need to be parallel to the plate and each other, while maintaining a certain height suitable for the envisaged particle size. Secondly, the relative distance of the rails needs to be constant. This turned out to be nearly impossible to achieve.

Alternatively, a mono-rail above the plate was constructed. This resolved the issue arising from the adjustability of relative distances and parallelism of the both rails. Now only the rails had to be parallel with the plate, while resting the container on a small metal strip of a predefined thickness (section 5.1.2).

Gap

A small teflon strip was fixed at the bottom of the upper container to prevent grains from getting stuck between the upper container and the supporting plate. Also, the idea was that any deficiencies in the distance between the container and plate would be corrected by this thin teflon strip as it is deformable. This did not work and was removed from the setup. Instead, the bottom of the upper container was precisely leveled off to maintain a constant gap width.

Load cell placement

It was planned to attach the load cell to the upper container by the use of a stainless steel holder. This was never implemented as it was clear that this would add weight to the container and, hence, increase the rail friction. The load cell was attached to the linear motor instead, at the expense of increased noise on the measured signal.

Rod rigidity

The rod in between the upper container and linear motor used to have a radius of 3 mm. At this radius, the rod is slightly bendable and, hence, started acting as a spring. The linear

motor is trying to adjust for this springlike behaviour, which led to a decreased accuracy of the linear motor's velocity and thus of the measurements. This was resolved by replacing the rod by a 6 mm radius hollow stainless steel tube.

Holder fins

The holder was firstly designed with fins, which break the movement of the grains underneath the holder. This would stop the holder from skewing during the shear motion. It turned out that this disturbed the measurement because the end compartments, formed by these fins, are not equally fillable. As a result, the first part of the motion resulting in net displacement of the grains, until the end compartment is filled. Up till that point the particles in the shear band are not fully under pressure by the normal weights added, which results in a lower shear stress than is actually the case. Removal of the fins resulted in more reliable measurements at average normal stresses ($\sigma_n \sim 1000$ Pa).

All these adjustments added up to the final setup as presented in figure 5.1.

B.5 Phase 5: Additions

It was envisaged that both the static and dynamic friction would be measurable with the test setup. Reproducible measurements of the dynamic friction coefficient were obtained. For instance, figure 6.1 shows that the average value during a motion (dynamic friction) is nearly equal for each successive movement. The static friction, which manifests itself as a peak value on the original (non-filtered) signal at the beginning of the motion, does show a much wider distribution. In fact, in many instances no significant peak was even observed.

This issue likely arises from the feedback mechanism of the linear motor: Once the static friction is overcome, the motor will overshoot slightly causing it to apply less force for a short instance. This behaviour will smooth out the first part of the measured signal until a steady state is achieved.

Hence, to delay the overshoot of the upper container, a spring-tipped rod was designed. This spring-tipped rod is shown in figure B.3. Although no measurements have been done with this spring-tipped rod, it possibly induces a stick-slip motion due to the hysteresis in static and dynamic friction¹⁰². As a consequence, the dynamic shear strength may be hard to be determine alongside its development in time.



(A) Digitally drawn cross section of the spring-tipped rod.



(B) Photograph of the spring-tipped rod.

FIGURE B.3: (A) Digitally drawn cross section and (B) photograph of the spring-tipped rod used to measure the static friction coefficient.

Matlab script

Below the Matlab script used to analyse the measured signal (see chapter 6) is given.

```
1 %% Set parameters
2 clear all
3
4 % PARAMETERS
5 scale = 5e-6; %m/cnt
6 %sample_freq = 1000; %Hz
7 M_pl = 97.85*1e-3; %Mass plate in kg
8 M = [61.73 61.78 61.82 245.84 250.54 364.52 364.2 373.62 360.91 362.18 ...
9      362.71 0 -M_pl*1e3]*1e-3; %Masses in kg
10 %M12 = only cover
11 %M13 = no mass at all
12
13 % USER INPUT
14 globalname = '1309_w0300_grain';
15 velo = 50;
16
17 Mno = {13 12 [2 3] 4 6 [2 3 6] [4 6] [6 2:4] [2 3 6 7] 5:7 6:8,...
18        [2 3 6:8] 5:8 6:9 [2 3 6:9] 5:9 6:10 [2 3 6:10] 5:10 6:11,...
19        [2 3 6:11] 5:11 [2 3 5:11] 4:11 2:11 1:11 [2 3 6:8] 13}; %SAME ORDER!
20
21 repetition = ones(1,length(Mno)).*30;
22 ME = zeros(1,length(Mno));
23 for ii = 1:length(Mno)
24     ME(ii) = sum(M([Mno{ii}]));
25 end
26 ME = ones(1,length(ME)).*M_pl+ME;
27
28 %DETERMINE FOLDERS
29 GlobalFolder = ...
30     '/Users/Stef/Documents/Study/AES/thesis/Experiments/Measurements';
31 TopFolder = sprintf('%s/%s',GlobalFolder,globalname);
32 DataFolder = sprintf('%s/TDMS',TopFolder);
33
34
35
36 %% Read all tdms (LabView) files
37 addpath(genpath(...
38     '/Users/Stef/Documents/Study/AES/thesis/Experiments/TDMSreader'));
39
40 cd(DataFolder)
41
42 % Generate list of all subfolders.
43 allSubFolders = genpath(DataFolder);
```

```

44
45 % Scan through them, separating them.
46 remain = allSubFolders;
47 listOfFolderNames = {};
48 while true
49     [singleSubFolder, remain] = strtok(remain, ':'); %#ok<STTOK>
50     if isempty(singleSubFolder), break; end
51     disp(sprintf('%s', singleSubFolder)); %#ok<DSPS>
52     listOfFolderNames = [listOfFolderNames singleSubFolder];
53 end
54 newListOfFolderNames = listOfFolderNames(2:end);
55 numfiles = length(newListOfFolderNames);
56
57 % Format cell data with entries: time of experiment, sample frequency ,
58 % mass, measurement, trigger signal
59
60 if numfiles ~= length(ME)
61     warning('Number of files mismatch')
62 else
63     rawdata = cell(numfiles+1,5);
64     rawdata(1,:) = {'Time (absolute)' 'Sample freq (Hz)' 'Mass (kg)'...
65                   'Voltage (V)' 'Trigger (V)'};
66
67     %Potentially str and str2 revised due to change in regional
68     %settings in windows
69
70     for ii = 1:numfiles
71         a = eval(sprintf('TDMS_getStruct(%s)',...
72                         sprintf('%s/Voltage.tdms',char(newListOfFolderNames(ii)))));
73         str = sprintf(...
74             'a.g.%s_%s_%s_%s_%s_%s...Voltage...All.Data.Dev1.ai2.data',...
75             newListOfFolderNames{ii}(end-14:end-13),...
76             newListOfFolderNames{ii}(end-12:end-11),...
77             newListOfFolderNames{ii}(end-10:end-7),...
78             newListOfFolderNames{ii}(end-5:end-4),...
79             newListOfFolderNames{ii}(end-3:end-2),...
80             newListOfFolderNames{ii}(end-1:end));
81         str2 = sprintf(...
82             'a.g.%s_%s_%s_%s_%s_%s...Voltage...All.Data.Dev1.ai0.data',...
83             newListOfFolderNames{ii}(end-14:end-13),...
84             newListOfFolderNames{ii}(end-12:end-11),...
85             newListOfFolderNames{ii}(end-10:end-7),...
86             newListOfFolderNames{ii}(end-5:end-4),...
87             newListOfFolderNames{ii}(end-3:end-2),...
88             newListOfFolderNames{ii}(end-1:end));
89         rawdata{ii+1,1} = newListOfFolderNames{ii}(end-5:end-2);
90         rawdata{ii+1,2} = 1/a.Props.log_dt;
91         rawdata{ii+1,3} = ME(ii);
92         rawdata{ii+1,4} = eval(str);
93         rawdata{ii+1,5} = eval(str2);
94     end
95     cd(TopFolder)
96     clear a str str2 allSubFolders ii listOfFolderNames...
97         newListOfFolderNames remain singleSubFolder TopFolder DataFolder...
98         GlobalFolder velo M ME M.pl Mno
99 end
100
101 %% Signals processing + calibration + save to Measurement_ ... .mat
102 data = cell(numfiles+1,4);
103 data(1,:) = {'Mass (kg)' 'Sample freq (Hz)' 'Voltage (V)' 'Trigger (V)'};
104 data(2:end,1) = rawdata(2:end,3);
105 data(2:end,2) = rawdata(2:end,2);
106
107 order = 1;
108 cut_off1 = 5; %Hz
109 for ii = 1:numfiles
110     %Trigger signal analysis. signal higher than 3V = 1, else 0

```

```

111     data{ii+1,4} = rawdata{ii+1,5}(1:length(rawdata{ii+1,5})) >= 3;
112
113     %Signal analysis (Filter 5Hz)
114     [butter_b1, butter_a1] = butter(order, cut_off1/(rawdata{ii+1,2})/2);
115     data{ii+1,3} = filtfilt(butter_b1,butter_a1,rawdata{ii+1,4});
116 end
117
118 % CALIBRATION
119 g = 9.81;
120
121 m1 = zeros(1,75);
122 m1(2:57) = (0:20:1100)+26.72;
123 m1(58:66) = (-50:50:350)+1201.27+26.75;
124 m1(67:75) = (0:50:400)+1602.06+26.75;
125
126 F1 = m1.*g./1000;
127 V1= [4.958 4.964 4.968 4.972 4.977 4.981 4.985 4.990 4.994 4.998 5.003,...
128      5.007 5.011 5.0155 5.020 5.024 5.029 5.033 5.037 5.041 5.046 5.050,...
129      5.0545 5.059 5.063 5.067 5.072 5.076 5.08 5.085 5.089 5.093 5.098,...
130      5.102 5.106 5.111 5.115 5.119 5.123 5.128 5.132 5.136 5.141 5.145,...
131      5.149 5.154 5.158 5.162 5.166 5.171 5.175 5.179 5.184 5.188 5.192,...
132      5.197 5.201 5.212 5.223 5.233 5.244 5.255 5.266 5.276 5.287 5.298,...
133      5.308 5.319 5.329 5.340 5.351 5.362 5.372 5.383 5.394];
134 V1=V1-V1(1);
135
136 FT = 'poly1';
137 calibration = fit(transpose(V1),transpose(F1),FT);
138
139 clear butter_b1 butter_a1 order cut_off1 rawdata ii g V1 F1 m1 FT
140
141 % Save to .mat in TopFolder
142     save(sprintf('Measurements_%s.mat',globalname),'data','numfiles',...
143           'calibration','scale','globalname','repetition','-v7.3')
144
145 %% Analysis
146 %clear all
147 cd(...)
148 '~/Documents/Study/AES/thesis/Experiments/Measurements/1309-w0300-grain')
149 load('Measurements_1309-w0300-grain.mat')
150
151 %Determine mean from signal after experiment
152 clear push pull
153 push=cell(numfiles+1,round(max(repetition)/2)+4);
154 pull=cell(numfiles+1,round(max(repetition)/2)+4);
155 push(1,1:4) = {'Mass (kg)' 'mean' 'std' 'V_mean'};
156 pull(1,1:4) = {'Mass (kg)' 'mean' 'std' 'V_mean'};
157 push(2:end,1) = data(2:end,1);
158 pull(2:end,1) = data(2:end,1);
159
160
161 %push/pull.int splits 4 different intervals per push/pull information per
162 %pull is discarded
163 push.int = cell(numfiles+1,round(max(repetition)/2)+9);
164 push.int(2:end,1) = data(2:end,1);
165 push.int(1,1:9) = {'Mass (kg)' 'mean1' 'std1' 'mean2' 'std2' 'mean3'...
166                  'std3' 'mean4' 'std4'};
167 pull.int = cell(numfiles+1,round(max(repetition)/2)+9);
168 pull.int(1,1:9) = {'Mass (kg)' 'mean1' 'std1' 'mean2' 'std2' 'mean3'...
169                  'std3' 'mean4' 'std4'};
170 pull.int(2:end,1) = data(2:end,1);
171
172 for ii = 18:numfiles
173     clear sig mean.V pnts
174
175     %pnts are the start and endpoints of each interval
176     pnts = find(abs(diff(data{ii+1,4})) == 1);
177     %Supposed to be exactly 2*repetition start+end points

```

```

178     if length(pnts) ~= round(2.*repetition(ii))
179         ii %#ok<NOPTS>
180         warning('Number of points not equal to 2x repetition')
181         for i = 2:2:length(pnts)
182             if pnts(i)-pnts(i-1) <= data{ii+1,2} %interval <1 second
183                 pnts(i) = NaN;
184                 pnts(i-1) = NaN;
185                 warning('Interval removed')
186                 interval_number = i-1 %#ok<NOPTS>
187                 clear interval_number
188             else
189                 end
190         end
191         pnts(isnan(pnts))=[];
192     else
193     end
194     %CHECK
195     if length(pnts) ~= round(2.*repetition(ii))
196         error('Too many faulty intervals')
197     else
198     end
199
200     sig = data{ii+1,3}.*data{ii+1,4};
201     sig(sig == 0) = NaN;
202
203     %determine mean signal, also for uneven pushes and pulls
204     if mod(repetition(ii),2) == 1 %more pushes than pull
205         %removes last interval to centralise the mean value
206         mean_V = nanmean(sig(1:pnts(end-1)));
207     else % equal pushes and pulls
208         mean_V = nanmean(sig);
209     end
210     sig = sig - mean_V; %Set signal to zero
211
212     n=4;
213     m=9;
214     %number of points after start and before end to discard. Half a second
215     offset = floor(0.5.*data{ii+1,2});
216
217     for i = 1:4:floor(repetition(ii)*2)
218         int_lengths = [(pnts(i+1)-offset-(pnts(i)+1+offset)),...
219             (pnts(i+3)-offset-(pnts(i+2)+1+offset))];
220         sub_int_length = floor(int_lengths./4);
221         interval =...
222             [(pnts(i)+1+offset):sub_int_length(1):(pnts(i+1)-offset),...
223             (pnts(i+2)+1+offset):sub_int_length(2):(pnts(i+3)-offset)];
224         if i == repetition(ii)*2-1
225             push{ii+1,n+1} =...
226                 mean(sig((pnts(i)+1+offset):pnts(i+1)-offset));
227             push_int{ii+1,m+1}(1) = mean(sig(interval(1):interval(2)));
228             push_int{ii+1,m+1}(2) = mean(sig(interval(2):interval(3)));
229             push_int{ii+1,m+1}(3) = mean(sig(interval(3):interval(4)));
230             push_int{ii+1,m+1}(4) = mean(sig(interval(4):interval(5)));
231         else
232             push{ii+1,n+1} =...
233                 mean(sig((pnts(i)+1 + offset):pnts(i+1)-offset));
234             push_int{ii+1,m+1}(1) = mean(sig(interval(1):interval(2)));
235             push_int{ii+1,m+1}(2) = mean(sig(interval(2):interval(3)));
236             push_int{ii+1,m+1}(3) = mean(sig(interval(3):interval(4)));
237             push_int{ii+1,m+1}(4) = mean(sig(interval(4):interval(5)));
238             pull{ii+1,n+1} =...
239                 mean(sig((pnts(i+2)+1 + offset):pnts(i+3)-offset));
240             pull_int{ii+1,m+1}(1) = mean(sig(interval(6):interval(7)));
241             pull_int{ii+1,m+1}(2) = mean(sig(interval(7):interval(8)));
242             pull_int{ii+1,m+1}(3) = mean(sig(interval(8):interval(9)));
243             pull_int{ii+1,m+1}(4) = mean(sig(interval(9):interval(10)));
244         end

```



```

245     n=n+1;
246     m=m+1;
247     end
248     push{ii+1,2} = mean([push{ii+1,5:end}]); %total mean
249     push{ii+1,3} = std([push{ii+1,5:end}]); %total standard deviation
250     push{ii+1,4} = mean.V; %offset absolute
251     pull{ii+1,2} = mean([pull{ii+1,5:end}]); %total mean
252     pull{ii+1,3} = std([pull{ii+1,5:end}]); %total standard deviation
253     pull{ii+1,4} = mean.V; %offset absolute
254
255     array1 = [];
256     array2 = [];
257     array3 = [];
258     array4 = [];
259     for k = 10:length(push_int(1,:))
260         array1 = [array1 push_int{ii+1,k}(1)]; %#ok<*AGROW>
261         array2 = [array2 push_int{ii+1,k}(2)];
262         array3 = [array3 push_int{ii+1,k}(3)];
263         array4 = [array4 push_int{ii+1,k}(4)];
264     end
265     push_int{ii+1,2} = mean(array1);
266     push_int{ii+1,3} = std(array1);
267     push_int{ii+1,4} = mean(array2);
268     push_int{ii+1,5} = std(array2);
269     push_int{ii+1,6} = mean(array3);
270     push_int{ii+1,7} = std(array3);
271     push_int{ii+1,8} = mean(array4);
272     push_int{ii+1,9} = std(array4);
273
274     array1 = [];
275     array2 = [];
276     array3 = [];
277     array4 = [];
278     for k = 10:length(pull_int(1,:))
279         array1 = [array1 pull_int{ii+1,k}(1)]; %#ok<*AGROW>
280         array2 = [array2 pull_int{ii+1,k}(2)];
281         array3 = [array3 pull_int{ii+1,k}(3)];
282         array4 = [array4 pull_int{ii+1,k}(4)];
283     end
284     pull_int{ii+1,2} = mean(array1);
285     pull_int{ii+1,3} = std(array1);
286     pull_int{ii+1,4} = mean(array2);
287     pull_int{ii+1,5} = std(array2);
288     pull_int{ii+1,6} = mean(array3);
289     pull_int{ii+1,7} = std(array3);
290     pull_int{ii+1,8} = mean(array4);
291     pull_int{ii+1,9} = std(array4);
292
293     end
294
295     %% Save global
296
297     close all
298     clear temp temp a b c
299     name = '_gr.w300.cl';
300     [a,~,b] = unique([push{2:end,1}]); %a = sorted, unique values, b = legacy
301
302
303     temp = zeros(length(a),6);
304     temp(:,1) = a;
305
306
307     c = 1:(length([push{2:end,1}]));
308     for ii = c
309         if temp(b(ii),2) == 0
310             temp(b(ii),2) = push{ii+1,2};
311             temp(b(ii),3) = push_int{ii+1,2};

```

```
312     temp(b(ii),4) = push_int{ii+1,4};
313     temp(b(ii),5) = push_int{ii+1,6};
314     temp(b(ii),6) = push_int{ii+1,8};
315     else
316         temp(b(ii),2) = (temp(b(ii),2) + push{ii+1,2})/2;
317         temp(b(ii),3) = (temp(b(ii),3) + push_int{ii+1,2})/2;
318         temp(b(ii),4) = (temp(b(ii),4) + push_int{ii+1,4})/2;
319         temp(b(ii),5) = (temp(b(ii),5) + push_int{ii+1,6})/2;
320         temp(b(ii),6) = (temp(b(ii),6) + push_int{ii+1,8})/2;
321     end
322 end
323
324 eval(sprintf('push%s = temp;',name));
325 clear a b c temp
326 [a,~,b] = unique([pull{2:end,1}]); %a = sorted, unique values, b = legacy
327 temp = zeros(length(a),2);
328 temp(:,1) = a;
329
330
331 c = 1:(length([pull{2:end,1}]));
332
333 for ii = c
334     if temp(b(ii),2) == 0
335         temp(b(ii),2) = pull{ii+1,2};
336         temp(b(ii),3) = pull_int{ii+1,2};
337         temp(b(ii),4) = pull_int{ii+1,4};
338         temp(b(ii),5) = pull_int{ii+1,6};
339         temp(b(ii),6) = pull_int{ii+1,8};
340     else
341         temp(b(ii),2) = (temp(b(ii),2) + pull{ii+1,2})/2;
342         temp(b(ii),3) = (temp(b(ii),3) + pull_int{ii+1,2})/2;
343         temp(b(ii),4) = (temp(b(ii),4) + pull_int{ii+1,4})/2;
344         temp(b(ii),5) = (temp(b(ii),5) + pull_int{ii+1,6})/2;
345         temp(b(ii),6) = (temp(b(ii),6) + pull_int{ii+1,8})/2;
346     end
347 end
348 eval(sprintf('pull%s = temp;',name));
349 clear temp
350
351
352 save(sprintf('Analysis-%s.mat',globalname),sprintf('pull%s',name),...
353     sprintf('push%s',name), 'calibration', 'scale','globalname',...
354     'repetition','-v7.3')
```